UFLA

UNIVERSIDADE FEDERAL DE LAVRAS

Eduardo Pereira da Rocha

Estudos computacionais de derivados de naftoquinona empregados como sondas espectroscópicas: cálculos relativísticos, parâmetros cinéticos e termodinâmicos

Lavras – MG
2016

Eduardo Pereira da Rocha

Estudos computacionais de derivados de naftoquinona empregados como sondas espectroscópicas: cálculos relativísticos, parâmetros cinéticos e termodinâmicos.

Tese apresentado à Universidade Federal de Lavras, como parte das exigências do Programa de Pós-Graduação em Agroquímica, área de Concentração Química/Bioquímica, para obtenção do título de Doutor.

Dr. Teodorico Castro Ramalho
Orientador

Lavras – MG
2016

Eduardo Pereira da Rocha

Estudos computacionais de derivados de naftoquinona empregados como sondas espectroscópicas: cálculos relativísticos, parâmetros cinéticos e termodinâmicos.
Computational studies derived naphthoquinone employed as spectroscopic probes: relativistic calculations, kinetic and thermodynamic parameters.

<div align="right">

Tese apresentado à Universidade Federal de Lavras, como parte das exigências do Programa de Pós-Graduação em Agroquímica, área de Concentração Química/Bioquímica, para obtenção do título de Doutor.

</div>

Aprovada em 08 de julho de 2016.

Prof. Dr. Felipe de Almeida La Porta (UFTPR)
Prof. Dr. Juan Manuel Andres Bort
Profª. Dra. Kátia Julia de Almeida (UFLA)
Prof. Dr. Matheus Puggina de Freitas (UFLA)
Prof. Dr. Nelson Henrique Morgon (UNICAMP)

Dr. Teodorico Castro Ramalho
Orientador

Lavras – MG
2016

"Dedico este trabalho a minha amada esposa
Jennyfer e meu amado filho Hugo."

AGRADECIMENTO

Agradeço a Deus pelos dons da sabedoria, paciência, perseverança e humildade para realizar este trabalho.

Agradeço a Universidade Federal de Lavras, ao Departamento de Química, ao programa de Pós-Graduação em Agroquímica, aos professores, técnicos e funcionários que conviveram comigo nesse tempo de doutorado.

Agradeço ao Instituto Federal de Educação, Ciência e Tecnologia do Sudeste de Minas Gerais e aos servidores do Campus Rio Pomba pela liberação e apoio para realização desta etapa.

Agradeço aos professores Matheus e Elaine, membros do Grupo de Química Computacional, pelo acolhimento durante este período e pelos momentos de partilha.

Agradeço aos colegas da "Era do Gelo": Lucas, Daniela, Silviana, Letícia Garcia, Letícia Assis, Tamiris, Lívia, Maíra, Telles, Alexandre, Matheus Aquino, Josué, Fátima, Daiana, Marcus Juliaci, William, Juliana, João Guilherme, Mariene, Stephen, Laize, e aos demais estudantes do programa que tive o privilégio de compartilhar experiências ao longo desse período de Doutorado.

Agradeço ao meu Orientador Teodorico, pela amizade, acolhimento, confiança e encorajamento durante esse breve tempo de trabalho, no qual aprendi muito e que modificou meu modo de agir como pesquisador.

Agradeço a minha família, Almerindo, Carmem, Luciano, Leonardo, Rafaela, Gisele, Pedro, Maria da Conceição, Daniele, Giuseppe, Arthur e Maria Eduarda pelo apoio e força.

Agradeço a minha esposa, Jennyfer, que me acompanhou nesse período, me dando força e me ajudando a superar os obstáculos no caminho. Ao meu filho Hugo, que cresceu junto com este trabalho, que foi a alegria nos momentos de dificuldade e desafio.

A todos o meu sincero agradecimento!

"As crianças devem ser autorizadas a quebrar coisas mais vezes. Isso é uma consequência da exploração. Exploração é o que você faz quando você não sabe o que está fazendo. É o que os cientistas fazem todo dia."

- Neil deGrasse Tyson -

"Qualquer um que não se choque com a Mecânica Quântica é porque não a entendeu. "

- Niels Bohr –

RESUMO GERAL

No mundo, muitas doenças, como o câncer, necessitam de um diagnóstico rápido. Atualmente, a espectroscopia de fluorescência é uma das metodologias mais promissoras para este fim, e derivados de naftoquinonas (ANQ) tem demonstrado aplicações como sondas fluorescentes. Estes compostos exibem o processo de transferência protônica intramolecular no estado excitado (ESIPT), que é um possível mecanismo responsável por seu uso como sondas fluorescentes. Neste trabalho, o processo ESIPT para derivados de ANQ foi realizado empregando o nível TD-DFT/CAM-B3LYP/DGTZVP e DFT/B3LYP/DGTZVP para os estudos eletrônicos e geométricos, respectivamente. Estes parâmetros foram selecionados com a ajuda da análise de componentes principais (PCA). O efeito do solvente foi avaliado durante o processo ESIPT foi favorável em solventes polares e não polares; além disso, as propriedades termodinâmicas mostram que o processo ESIPT é favorável com uma constante de equilíbrio de transferência do próton de ~10^5. ANQ e seus derivados halogenados tem propriedades fluorescentes e a presença de tais substituintes promove mudanças nas propriedades espectroscópicas dos compostos. Efeitos relativísticos como o acoplamento spin-órbita, o hamiltoniano relativístico e funções de base que incluem correções relativísticas são essenciais para a precisão dos cálculos de propriedades espectroscópicas. Para selecionar entre esses importantes fatores, foi empregado o planejamento fatorial do tipo 3^3, conhecido como planejamento Box-Benhken, nos derivados halogenados de naftoquinonas (F, Cl, Br e I). Dos resultados, observou-se que os compostos derivados contendo Cl, Br e I não apresentaram o processo ESIPT. O derivado contendo F apresentou o processo, apresentando 4,69 eV para energia de absorção, -1,58 eV para energia de transferência do próton e 1,87 eV para energia de emissão. Finalmente, a técnica de PCA foi empregada para análise de similaridade de 36 derivados de ANQ de acordo com as barreiras de energia envolvidas no processo ESIPT. Os resultados apontam que, substituintes com alta densidade eletrônica promovem deslocamento para comprimento de onda na região do vermelho. De fato, o efeito dos substituintes promoveu um entendimento a respeito do comportamento do processo ESIPT em derivados de ANQ, e como os parâmetros cinéticos e termodinâmicos influenciam o processo.

Palavras Chave: Estado excitado; sodas fluorescentes; Naftoquinonas; ESIPT; DFT; TD-DFT; Quimiometria

General Abstract

In the world, many diseases, such as cancer, require a rapid diagnosis. Currently, it is well known that the fluorescent spectroscopy is one of the most promising methodologies to this end. In this perspective, naphthoquinone derivatives (ANQ) have demonstrated applications as fluorescent probes. Those compounds exhibit excited-state intramolecular proton transfer (ESIPT), which is the main mechanism responsible in their use as fluorescent probes. In this work, the ESIPT process for ANQ was performed at the TD-DFT/CAM-B3LYP/DGTZVP and DFT/B3LYP/DGTZVP level for the electronic and geometric studies, respectively. These parameters were selected for the PCA analysis. The solvent effect was evaluated, and the ESIPT process of ANQ was favorable in nonpolar and polar solvents. Furthermore, the thermodynamics properties showed that the ESIPT is favorable with a proton transfer equilibrium constant of ~10^5. Naphthoquinone and their halogenated derivatives have fluorescent properties and the presence of such substituents promote changes in the spectroscopic properties of the compounds. Relativistic effects such as spin–orbit coupling, the Hamiltonian relativistic and the basis set including relativistic corrections are essential for the accurate calculation of spectroscopic properties. For the selection of which of these factors, it was employed the factorial design of the 3^3 type, known as a Box–Benhken design, in the halogenated derivatives naphthoquinone (F, Cl, Br and I). For the results, it was observed that the derivatives compounds containing Cl, Br and I do not have the ESIPT process. The compound containing F showed the process, it having 4.69 eV for absorption energy, −1.58 eV for the proton transfer energy and 1.87 eV for the emission energy. Finally, the PCA techniques have been employed for analysis the similarity between 36 naphthoquinone (ANQ) derivatives according to the energies involving in ESIPT process. Our findings point out that substituents with higher electron density promote wavelength red-shifting. In fact, the substituent effects provide an understanding about behavior of the ESIPT process in ANQ derivatives, and how kinetic and thermodynamic parameters can be influenced.

Keywords: Excited-State; Fluorescence Probe; Naphthoquinone; ESIPT; DFT; TD-DFT; Chemometric

LISTA DE ILUSTRAÇÕES

PRIMEIRA PARTE

SEGUNDA PARTE

ARTIGO 2

LISTA DE TABELAS

PRIMEIRA PARTE

SEGUNDA PARTE

Artigo 2

Artigo 3

Artigo 4

Lista de Abreviaturas e siglas

ESIPT	Transferência Protônica intramolecular no estado excitado
GSIPT	Transferência Protônica intramolecular no estado fundamental
GS	Estado fundamental
UV	Ultra-violeta
LED	Diodo emissor de luz
ESPT	Transferência do próton no estado excitado
S_0	estado eletrônico fundamental
S_1	primeiro estado eletrônico excitado
DHAQ	Diidroxiantraquinona
DNA	ácido desoxirribonucleico
4-DMAP	4-dimetilaminoftalimida
HIV	Vírus da imunodeficiência Humana
PDOHBA	p-N,N-dimetilamino-ortoidroxibenzaldeído
GFP	Proteína verde fluorescente
HBDI	(Z)-4-(4-hidroxibenzilideno)-1,2-dimetil-1H-imidazol-5(4H)-ona
EDTA	Etilenodiaminotetracético
ADP	Adenosina difosfato
ATP	Adenosina trifosfato
GDP	Guanina Difosfato
GTP	Guanina Trifosfato
RNA	ácido ribonucleico
PPi	Fosfato inorgânico
ALP	Alcalinefosfatases
AIDS	Síndrome da imunodeficiência adquirida
DOX	Doxorrubicina
BTD	2,1,3-benzothidiazole
dsDNA	dupla fita de DNA
BSA	Albumina de soro bovina
DFT	Teoria do Funcional de Densidade
HK	Hohenberg e Kohn
KS	Kohn e Sham
XC	Troca e correlação
LDA	Aproximação de densidade local
LSDA	Aproximação de densidade local de spin
GGA	Aproximação do Gradiente Generalizado
BP86	Funcional de gradiente corrigido proposto por Becke e Perdew em 1986.
HF	Hartree-Fock
LYP	Lee-Yang-Park
MP2	Teoria da perturbação de segunda ordem
LR-LSDA	Aproximação de densidade local de spin de longa distância
RSHF	Funcional híbrido de longo alcance
TD	Dependente do tempo
TDDFT	Teoria do Funcional de densidade dependente do tempo
DK	Douglas-Kroll
ZORA	Aproximação Regular de Ordem Zero
DKH	Douglas-Kroll-Hess
SOC	Acoplamento spin-órbita
ECP	Potencial efetivo de caroço
SR	Superfície de resposta

DOE	Planejamento de experimentos
EXP	Experimentos
Regr	Regressão
Resid	Resíduo
RSD	Resíduo padrão
PRESS	Resíduo predito
ANOVA	Análise de Variância
PCA	Análise de Componentes Principais
PC	Componente Principal
SVD	Decomposição em valores singulares
HCA	Análise Hierarquica de Cluster
DGTZVP	Função de base Triple-Zeta Valence Polarizável do tipo Gaussiana
ANQ	2-Amino-1,4-naftoquinona
NAT1	N-acetiltransferase 1
ICT	Transferência por troca de carga
PCM	Modelo de polarização contínua
IEF-PCM	Formalismo da equação Integral do modelo de polarização contínua
CASSCF	Sítio ativo completo e campo alto consistente
B3LYP	Funcional híbrido com 3 parâmetros de troca de Becke e parâmetros de correlação de Lee-Yang e Park.
B3PW91	Funcional híbrido com 3 parâmetros de troca de Becke e parâmetros de correlação de Perdew/Wang 1991
CAM-B3LYP	Funcional com Método de Atenuação de Coulomb usando B3LYP
mPW1PW91	Funcional empregando o potencial de troca de Perdew-Wang modificado por Adamo e Barone combinado com potencial de correlação de Perdew-Wang de 1991.
ωb97X-D	Funcional de Grimmes incluindo dispersão empírica
PBE	Função de base Perdew/Burke/Ernzerhof 1996
cc-pVTZ	Função de base de Dunning com triple zeta valencia
UV-VIS	Ultra-violeta e visível
PES	Superfície de Energia Potencial
ES	Estado excitado
CASPT2	Espaço ativo completo acoplado a teoria da perturbação de segunda ordem.
TZV	Função de base do tipo Triple Zeta Valencia
TZV_DKH	Função de base do tipo Triple Zeta Valencia com correção Douglas-Kroll-Hess
TZV_ZORA	Função de base do tipo Triple Zeta Valencia com correção ZORA
SOC-ENC	Acoplamento Spin órbita com carga nuclear efetiva
SOC-ENC-MFA	Acoplamento Spin órbita com carga nuclear efetiva e abordagem de campo médio.
TDA	Aproximação Tamm–Dancoff
COSMO	Condutor do tipo modelo de triagem (COnductor-like Screening MOdel)
AFNQ	2-amino-3-fluor-1,4-naftoquinona
ACNQ	2-amino-3-cloro-1,4-naftoquinona
AINQ	2-amino-3-iodo-1,4-naftoquinona
ABNQ	2-amino-3-bromo-1,4-naftoquinona
Std. Err	Erro padrão
ORCA	Programa de química quântica desenvolvido por Franck Nesee e colaboradores

HBO	hidroxifenilbenzoxazol
HBI	hidroxifenilbenzimidazol
HI	hidroxifenilindol

Lista de símbolos

I	símbolo do elemento químico Iodo
pKa	potencial da constante de acidez
Zn(II)	cátion zinco com carga 2+
Cu(II)	cátion cobre com carga 2+
Fe^{2+}	cátion ferro com carga 2+
F^-	ânion fluoreto com carga -1
B	símbolo do elemento químico Boro
Br	símbolo do elemento químico Bromo
F	símbolo do elemento químico Flúor
Si	símbolo do elemento químico Silício
O	símbolo do elemento químico Oxigênio
Cl	símbolo do elemento químico Cloro
N	símbolo do elemento químico Nitrogênio; conformação normal no estado fundamental
H	símbolo do elemento químico Hidrogênio
Zr	símbolo do elemento químico Zircônio
Zn	símbolo do elemento químico Zinco
Ca	símbolo do elemento química Cálcio
OH	símbolo do grupo hidroxila
NH	símbolo do grupo amino
OCH3	símbolo do grupo Metoxido
CN	símbolo do grupo Cianeto
NHCH3	símbolo do grupo metilamina
min	minutos
nm	nanômetro
eV	elétron Volt
exp	exponencial
kcal	quilocaloria
Å	medida de distância, angstrons
λ	comprimento de onda
cm^{-1}	número de onda (centrímetro a -1)
N*	Conformação normal no estado excitado
T*	Conformação tautomérica no estado excitado
pH	potencial hidrogeniônico
π	pi; elétrons pi
h	Constante de Plank
υ	Frequência de um feixe de radiação eletromagnética
E_0	Energia do estado fundamental
$\rho(\mathbf{r})$	Densidade eletrônica do estado fundamental
$\rho(\mathbf{x})$	Densidade eletrônica
α	spin-up; ângulo
β	spin-down; termo da equação de Dirac equivalente a matriz 4x4;
$\hat{n}(r)$	Operador densidade
H	Hamiltoniano
∇^2	Laplaciano

∇	Gradiente
v_{KS}	Potencial externo Khon-Shan
$n(r)$	Gradiente de densidade
Z_α	Carga nuclear
E_{XC}	Potencial de troca e correlação
δ	Densidade
NN	Núcleo-núcleo
v_{eN}	Potencial de repulsão elétron-núcleo
v_{NN}	Potencial de repulsão de Coulomb
J	Operador Energia Potencial
T	Operador energia cinética
V	Potencial externo dependente do tempo
W	Interação entre dois elétrons
τ_σ	Energia cinética orbital KS
$\varphi_{i\sigma}$	Função densidade de estado
t	Tempo
ψ	Função de onda
v	Velocidade do elétron
c	Velocidade da luz no vácuo
m_0	Massa reduzida
p	Momento angular
i	Número irracional
$\hbar$	Hamiltoniano relativístico
$\hat{a}_x$	Termo da equação de Dirac equivalente a matriz 4x4
I	Matriz identidade 4x4
L	"large"
S	"small"
ε_k	Matriz operador de ordem 4x4
V_{eff}	Potencial efetivo
B_{eff}	Campo magnético effetivo
μ_B	Magneton de Bohr
$\boldsymbol{\sigma}$	Vetor de matrizes de spin de Pauli
E	Energia do momento angular de Zeeman
Ω	Constante de estrutura fina
Z_α	Cargas nucleares
r	Coordenadas dos elétrons
$\vec{p}_i$	Operador momento eletrônico
$\vec{S}_i$	Operador spin eletrônico
L_{iA}	Momento angular orbital
S_i	Momento angular de spin
β_0	Coeficientes do modelo gerado pelo planejamento fatorial
X_1	Variáveis do modelo gerado pelo planejamento fatorial
Y	Resposta do modelo gerado pelo planejamento fatorial
2^K	Modelo de planejamento fatorial de segunda ordem
3^K	Planejamento fatorial de Terceira ordem
R^2	Variância Explicada
Q^2	Variância Predita
SS	Soma dos quadrados
P	Porcentagem
S_{kl}	Elemento da matriz S

d_{kl}	Distância euclidiana entre a amostra k e l
d_{max}	Distância euclidiana máxima
º	Graus
K	Temperatura Kelvin; Forma ceto no estado fundamental; Constante de equilíbrio
K*	Forma ceto no estado excitado; Constante de equilíbrio no estado excitado
E	Forma enol no estado fundamental; Energia
E*	Forma enol no estado excitado; Energia no estado excitado
k	Constante de equilíbrio; Constante de Velocidade
A	Parâmetro do planejamento fatorial
B	Parâmetro do planejamento fatorial
C	Parâmetro do planejamento fatorial
Q	Constante de equilíbrio no estado fundamental
Q*	Constante de equilíbrio no estado excitado
ΔE_1	Variação de energia de absorção
ΔE_3	Variação de energia de emissão
ΔG^0	Variação de Energia Livre de Gibbs padrão
$\Delta G^{\#}$	Variação de Energia livre de Gibbs do estado de transição
ΔG^*	Variação de Energia Livre de Gibbs do estado excitado
ΔH	Variação de Entalpia
ΔS	Variação de Entropia
ΔE	Variação de Energia
$\Delta H^{\#}$	Variação de Entalpia do estado de transição
$\Delta S^{\#}$	Variação de Entropia do estado de transição
$\Delta E^{\#}$	Variação de Energia do estado de transição
ΔG	Variação de Energia Livre de Gibbs
R	Constante Universal dos Gases; Radical
T	Temperatura
pK	potencial da constante de equilíbrio no estado fundamental
pK*	potencial de constante de equilíbrio no estado excitado
atm	atmosfera (unidade de medida de pressão)
k_B	Constante de Boltzmann
k*	Constante de Velocidade no estado excitado
R_n	Radical
d	distância

SUMÁRIO

PRIMEIRA PARTE

ARTIGO 1 - PROCESSO DE TRANSFERÊNCIA PROTÔNICA INTRAMOLECULAR NO ESTADO EXCITADO (ESIPT): APLICAÇÕES EM SONDAS FLUORESCENTES

Processo De Transferência Protônica Intramolecular no Estado Excitado (ESIPT): Aplicações em Sondas Fluorescentes

Abstract: Currently the opportune diagnosis of cancer has shown a great importance, mainly by decreasing the mortality rate. Among the techniques employed to achieve the diagnosis, spectroscopy has been highlighted for presenting safe and highly accurate diagnoses. The Fluorescence Spectroscopy has become very important in cancer diagnosis, being employed in breast, oral cavity and esophagus cancer testing. The technique employs fluorophore which in many cases have groups capable of carrying out the intramolecular proton transfer in the excited state (ESIPT). These compounds may be used for various molecular targets such as cations, anions and proteins detection, besides the diagnosis of diseases. Spectroscopic probes have an important role in the development of more accurate diagnosing diseases methods, which may influence the treatment and avoid the risks of further surgery and patient death.

1. INTRODUÇÃO

Na atualidade, o câncer é uma das doenças que mais vitimam no mundo.[1] Um dos motivos é a dificuldade de diagnóstico no pré e pós-operatório.[2] Quando o diagnóstico no pós-operatório é feito de forma acurada, diminui a necessidade de uma nova cirurgia, que hoje é de 50% dos casos de câncer de mama com margem positiva e 10% dos casos com margem negativa.[2] Atualmente, um dos grandes desafios do diagnóstico de imagem é desenvolver um sistema capaz de localizar espécies em diferentes ambientes para detectar focos de câncer nas margens cirúrgicas para uso clínico com alta resolução.[2]

Dentre as técnicas de diagnóstico empregadas no tratamento do câncer estão os exames de Tomografia, Ressonância Magnética por Imagem e Endoscopias Ultrassônicas. Porém, em muitos casos, o diagnóstico não traz a

acurácia pretendida para a doença, e muitos pacientes são vitimados pela falta de um diagnóstico preciso.[5] Muitos esforços têm sido empregados para detectar tumores utilizando a espectroscopia molecular, a exemplo disso, temos a espectroscopia molecular de infravermelho e Raman,[3] que medem as vibrações moleculares das amostras e são empregadas para diagnóstico de arteriosclerose no sangue, displasia e outros tipos de câncer,[4] como os tumores na tireoide, células cervicais, pele, mucosa oral, cólon, mama, células de linfomas e câncer de cérebro.[3] A Espectroscopia de Refletância Difusa tem sido usada no diagnóstico do progresso de doenças, como câncer de colón, esôfago, cervical e bexiga.[2,4] A Espectroscopia de Fluorescência, que mede a emissão de fluóforos endógenos encontrados em tecido, foi relatada para o diagnóstico de displasia no colo uterino, câncer no esôfago e cavidade oral, e por ser eficiente para estudos em tempo real de células vivas e outros tipos de doenças.[5,4,6] Além dos diagnósticos citados, esse tipo de espectroscopia molecular apresenta informações complementares sobre a composição do tecido, a organização, o movimento, e, superfície de membranas celulares e suas combinações, contribuindo com informações úteis sobre a doença e seu diagnóstico.[4]

Nesse contexto, vem crescendo o interesse por sondas fluorescentes. Essas sondas são altamente sensíveis, de fácil operação e permitem a análise por imagem em sistemas vivos.[7] Nos últimos anos, o interesse pelos compostos que apresentam o processo de transferência protônica intramolecular no estado excitado (ESIPT) vem aumentando, devido aos prospectos de aplicação no desenvolvimento de novas sondas fluorescentes, visando o desenvolvimento de métodos analíticos com aplicação nos campos da biofísica, medicina e no controle ambiental.[8]

2. O Processo de transferência protônica intramolecular no estado excitado

O processo ESIPT foi primeiramente observado por Weller em 1956, em estudos com o salicilato de metila (Figura 1).[9,10,8] O processo de transferência protônica intramolecular no estado excitado (ESIPT) pode ser iniciado por um pulso de luz, e posteriormente ser explorado como um sistema de transferência dinâmico.[11] As moléculas que apresentam o processo ESIPT apresentam no estado fundamental uma ligação de hidrogênio intramolecular entre um grupo hidroxila (OH) ou amino (NH) com uma carbonila ou ao nitrogênio do grupo piridil,[8,12] em uma distância menor que 2 Å.[13]
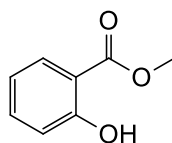
Figura 1 -Estrutura química do Salicilato de Metila.

No estado fundamental, a estrutura mais estável é a forma enol ou amino quando esse composto passa para o estado excitado por absorção de um fóton de luz, ele pode promover a troca para seu tautômero mais estável no estado excitado que é a forma ceto.[14,15] Esse processo adiabático acontece em pico-segundos e resulta na formação de produtos tautoméricos fotoativos que emitem radiação em comprimento de onda maior que no estado fundamental.[8,16] O estado ceto excitado produz o processo ESIPT pela diferença na geometria estrutural e configuração eletrônica em comparação com a espécie original (estado fundamental). Esse fato, gera um grande deslocamento de Stoke,[17] da ordem de 8 a 10 mil cm^{-1}.[12,15]

Depois, o produto ESIPT retorna ao seu estado fundamental pela emissão fluorescente ou perda da radiação (conversão interna),[12] que posteriormente é revertido ao tautômero, no estado fundamental, mais estável.[8] A forma enol é

observada no espectro de absorção e a forma ceto no espectro de fluorescência, o que caracteriza o processo ESIPT.[8]

Existem muitas dúvidas sobre o final do processo, e seu retorno ao estado fundamental (GS), na verdade, alguns pesquisadores na literatura relatam que o processo é irreversível. Porém, nos últimos anos, propostas reversíveis do processo vêm sendo estudadas.[8]
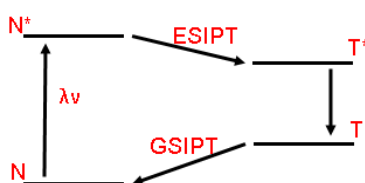
Esquema 1 - Diagrama de transição do estado fundamental (N) para o estado excitado (N*) e a conversão para a forma tautomérica (T*) via processo ESIPT, e o retorno ao estado fundamental pelo processo GSIPT.

Moléculas que apresentam o processo ESIPT tem muitas aplicações, como corantes laser,[18,14,19] foto estabilizadores UV,[18,20,19] sondas de proteínas e membranas,[18,20] LEDs orgânicos,[18] diodos emissores de luz,[20,16] sondas para diversos ambientes biológicos e solvatação dinâmica,[14] sensores de íons e metais,[14] materiais luminescentes,[12] entre outras aplicações.

A razão ultra-rápida do ESIPT, com um grande deslocamento de Stoke,[21] entre a banda de absorção e emissão do tautômero (pico a pico), fornece uma ampla janela de cor complementar para o processo de emissão e reabsorção.[22] Emissões brancas foram observados por Park e co-autores. Sun e co-autores observaram emissão branca dopando dois polímeros sólidos com moléculas que apresentam o processo ESIPT.[22] A alta intensidade da emissão fluorescente e o grande deslocamento de Stoke devido ao fenômeno ESIPT são muito sensíveis e dependem muito do ambiente local do composto. Porém, em alguns compostos, como os da família das 2-(2'-hidroxifenil)-benzimidazol, (Figura 2), é possível

regular estruturalmente essa propriedade fotofísica, excedendo a influência do ambiente.[21]
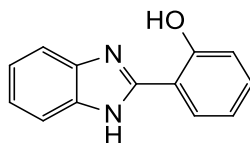
Figura 2 - Estrutura química da 2-(2'-hidroxifenil)benzimidazol.

Na literatura, diferentes etapas de reação para o processo ESIPT são apesentadas devido as características ácido-base das moléculas.[23] Quando ocorre a excitação eletrônica da molécula, características dos sítios ácido e básico aumenta, envolvendo assim, a troca rápida do próton na superfície do estado excitado.[21] Muitos compostos apresentam alteração no seu pKa quando excitados, podendo sofrer a desprotonação na presença de espécies básicas, como o solvente.[18,24] A influência do solvente é significativa no processo ESIPT, de modo que, solventes polares diminuem o solvatocromismo das moléculas, podendo até reduzir o efeito de emissão fluorescente. Solventes polares, podem concorrer diretamente pelo próton, promovendo o processo de transferência do próton no estado excitado (ESPT). Nesse processo, moléculas de solvente como a água, podem concorrer pelo próton, e nesse caso, impedir a transferência intramolecular.[24] Nesses solventes polares, a solvatação pode prejudicar o processo devido a inúmeras ligações de hidrogênio entre o soluto e o solvente.[25] Porém, solventes apolares favorecem a transferência, e alguns aumentam as características de fluorescência e a intensidade da emissão, que em alguns casos, se devem a estabilização dos produtos tautômeros.[24]

Alcoóis aromáticos apresentam acidez quando excitados para o primeiro estado excitado (S1). Como exemplo, o grupo hidroxila do 2-naftol, (Figura 3), aumenta sua acidez aproximadamente em 7 ordens de grandeza na forma excitada ($pKa \approx 2,8$) quando comparado ao estado fundamental ($pKa(S_0) \approx 0,5$).[24] O aumento

da acidez na excitação do 1-naftol é tão pronunciada que ele muda o pKa de 9,4 (estado fundamental) para 0,4 (no estado excitado). Fenóis excitados usam a desprotonação adiabática em piscosegundos em água via processo ESPT para emitir fluorescência na forma de fenolato no estado excitado.[24]
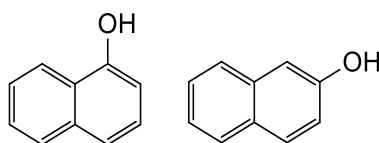
Figura 3 - Estrutura química do 1-naftol e do 2-naftol.

Recentemente, um conceito intrigante foi reportado por Dunietz e colaboradores na relação entre os graus de conjugação π e a ocorrência do processo ESIPT.[26,14] Nessa aproximação teórica, os autores reconstruíram virtualmente um conjunto de derivações com números diferentes e posições do anel aromático em análogos de dímeros da 7-azaindol, (Figura 4), e calcularam a relação entre a energia e a estrutura dessas espécies tautoméricas no estado excitado. Como um resultado, observou que os graus de conjugação π das espécies tautoméricas, no estado excitado, influenciam o processo.[26,14]
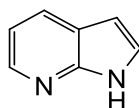
Figura 4 - Estrutura química do composto 7-azaindol.

Observaram que a conjugação π prolonga a deslocalização, melhorando a distribuição do excesso de carga no centro da reação e tende a baixar a energia relativa das espécies tautoméricas no estado excitado. Resultando, assim, numa grande força termodinâmica dirigida no sentido da transferência do próton.[26] Experimentalmente, Chung e coautores, procuraram provar esse conceito com o

estudo de vários 7-azaindol derivados da tereína; e mostraram que esses fenômenos são importantes para o processo ESIPT.[26]

A substituição em compostos que apresentam o processo ESIPT pode influenciar a emissão. Doadores de elétrons, em que os elétrons podem ser considerados ressonantes para o oxigênio da carbonila pela excitação, criam um grande momento de dipolo para o estado excitado na forma enol em relação ao tautômero no estado excitado e sua forma no estado fundamental. Essa substituição, então, causada por grupos doadores, pode promover um aumento da transferência do próton.[27]

Compostos que apresentam o processo ESIPT empregados como sondas fluorescentes apresentam características positivas como a não dependência da concentração, a variação da luz de excitação,[9] a ligação receptor-analito deve ser seletiva e muito sensível, além de gerar um sinal analítico grande.[28] Podendo ser empregados em diferentes ambiente e para diferentes alvos moleculares de interesse biológico, razão essa, que faz com que esses compostos sejam importantes dentro da espectroscopia de fluorescência para o diagnóstico de doenças.

3. Aplicações em Sondas
3.1. Sondas fluorescentes para cátions e metais

As Diidroxiantraquinonas (DHAQ), figura 5, são um grupo de compostos interessantes do ponto de vista fotoquímico e fotofísico.[29] Corantes DHAQ apresentam um grupo carbonila e uma hidroxila vizinho que podem ser empregados para ancorar na superfície de semi-condutores.[29]

A alizarina, a partir da segunda metade do século 19 revolucionou a indústria têxtil, apresentando afinidade por metais do bloco p e d, formando complexos com cores fortes, que são usados na quantificação dos mesmos. Sua interação com o cálcio foi importante para estudos de crescimento dos ossos e

osteoporose, expressão gênica e a engenharia de tecidos. Sendo empregada, também, na detecção de boro e fluoreto.[29] A Quinizarina forma complexos fluorescentes com lítio, boro, alumínio, e pode ser utilizado para a detecção desses elementos por espectroscopia de fluorescência. A Crisazina foi empregada na detecção de cálcio, cobre, platina, chumbo, cádmio, zinco, níquel, manganês, ferro e cobalto.[29]
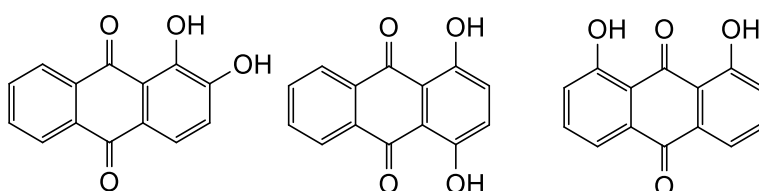
Figura 5 - Estrutura química da Alizarina, Quinizarina e Crizasina.

Quimiossensores fluorescentes artificiais para íons de metais de transição tem sido alvo de um grande número de pesquisas nos últimos anos, principalmente para o zinco, que é o segundo metal de transição mais abundante dentro do organismo humano.[30] Ele é significativo em vários processos biológicos, como metabolismo celular, expressão genética, reparação do DNA, apoptose celular, neuro-transmissão, regulação de proteínas, reorganização e regulação da desordem neurológica em doenças como às de Parkinson, Alzheimer, esclerose lateral amiotrófica e epilepsia.[30,28] Entre os diferentes caminhos para a produção de sondas fluorescentes para a detecção do zinco, o mais promissor é a utilização de compostos que apresentam o processo ESIPT.[28] Os derivados de 2-(benzotiazol-2-il)fenol estão envolvidos na formação de sondas fluorescentes de zinco. O hidroxinaftaleno baseado em sensores de benzotiazol, também tem recebido atenção para a determinação desse metal por espectroscopia de fluorescência.[13]
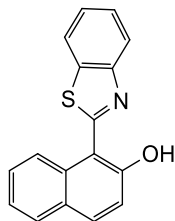
Figura 6 - Estrutura química da sonda derivado do 2-naftol com benzotiazol para análise de Zn(II).

3.2. Sondas fluorescentes formadas por proteínas.

Aminoácidos não naturais são importantes para investigar peptídeos e proteínas, podendo servir como sondas locais para monitoramento seletivo de propriedades e funções proteícas.[31] Os aminoácidos fluorescentes são atrativos por serem altamente sensíveis a métodos de fluorescência. Desde que os aminoácidos fluorescentes, como o triptofano, (Figura 7), apresentaram propriedades fluorescentes ruins, muitas pesquisas têm como objetivo desenvolver aminoácidos com melhores propriedades fluorescentes.[31]
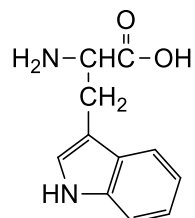
Figura 7 - Estrutura química do Triptofano.

Interações biomoleculares decrescem com a polaridade e com a presença de água em sítios lábeis, que podem ser monitorados por aminoácidos fluorescentes. Um exemplo: Foram os aminoácidos baseados no Prodan, Figura 8, que foram utilizados para monitorar interações do peptídeo S com a ribonuclease S e receptores de δ-opióides como antagonistas, bem como para estimar a constante dielétrica local do domínio B1 da proteína G do estafilococo.[31]
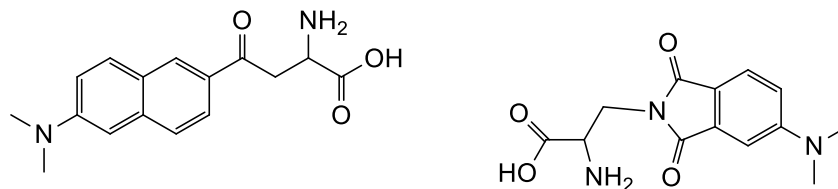
Figura 8 - Estrutura química da Prodan e da 4-dimetilamiononaftilimida (4-DMAP).

Os aminoácidos baseados no 4-dimetilaminoftalimida (4-DMAP) fluorescente foram aplicados para ligar a peptídeos na tentativa de investigar domínios de ligação de sulfeto (SH$_2$) fosfotirosiníco e interações peptídeo-calmodulina.[31]

Estudos de aminoácidos fluorescentes ainda são limitados a poucos exemplos e focados apenas em interações proteínaproteína, enquanto que, estudos de interações peptídeos-oligonucleotídeos são mais raros. Strizhake e colaboradores estudaram derivados da 3-hidroxicromona, que apresentam o processo ESIPT, para avaliar a detecção do núcleo capsídeo do vírus HIV. Estes dados mostram relativa interação da sonda com as proteínas e nucleosídeos presentes na estrutura.[31] As albuminas são importantes proteínas presentes no sistema circulatório, contribuindo para a manutenção da pressão osmótica.[32,33] As albuminas transportam muitos compostos, como ácidos graxos, sais biliares, hormônios, metais e fármacos.[33] Podem também, transportar proteínas geradas por tumores que entram na corrente sanguínea.[32]

A natureza da ligação entre sondas fluorescentes e a albumina tem sido investigada na tentativa de avaliar os problemas ocasionados nos estudos de estrutura molecular de proteínas pelo uso de surfactantes, que dobram/desdobram/redobram as estruturas das proteínas.[33] Alguns estudos mostram a aplicação da sonda p-N,N-dimetilamino-ortoidroxibenzaldeído (PDOHBA), Figura 9, que apresenta o processo ESIPT, nos estudos de estrutura

de proteínas pela interação com a albumina.[33] Nesse caso, a sonda foi empregada para avaliar mudanças conformacionais da proteína, carreando-a com o triptofano intrínseco da albumina.[33]
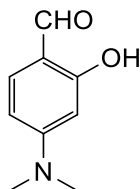
Figura 9 - Estrutura química da PDOHBA.

A molécula exibiu bandas de fluorescência tanto em ambiente polar como em ambiente apolar. Observaram, também, que a molécula se liga dentro da cavidade interna da albumina, diminuindo seu contato com a água, aumentando as emissões do estado excitado.[33] Caracterizaram a sonda como promissora para o estudo de propriedades estruturais de proteínas com o auxílio da albumina, como carreadora. Dentro dos estudos de proteínas geradas por células tumorais, a albumina pode ser empregada como alvo, uma vez que, carreia essas proteínas no meio sanguíneo para peptídeos biomarcadores que identificam essas proteínas dentro da cavidade da albumina.[32]

Sondas fluorescentes baseados em proteínas podem ser utilizadas para detecção de complexos bioativos (interação com metais Zn e Ca, por exemplo, na estrutura de proteínas) e para investigar estruturas subcelulares específicas.[34] Outro exemplo de sondas empregando proteínas são as Proteínas Verde Fluorescente (GFP), elas têm recebido intensa atenção devido a suas aplicações em biologia molecular e bioquímica.[35,11,16] Essas GFP apresentam reações do tipo ESPT no qual a ligação de hidrogênio envolve a molécula de água e certos aminoácidos. A solvatação por moléculas de água podem influenciar o processo de ESPT devido às inúmeras ligações de hidrogênio entre o soluto e o solvente.[25]

As GFP que apresentam o cromóforo (Z)-4-(4-hidroxibenzilideno)-1,2-dimetil-1H-imidazol-5(4H)-ona (HBDI) apresentam vantagens.[35] O HBDI é composto por um anel de 7 membros formado por uma ligação de hidrogênio, evidenciado pela presença de uma distância de 2,61 Å e um ângulo diedro de 175°, que apresenta o processo ESIPT.[35] A formação dessa ligação de hidrogênio favorece a deslocalização dos elétrons π e diminui o "gap" de energia entre os estados S0→S1. A transição entre os tautômeros provocado pelo processo ESIPT, então, gera a forma Zwitteriônica.[35]
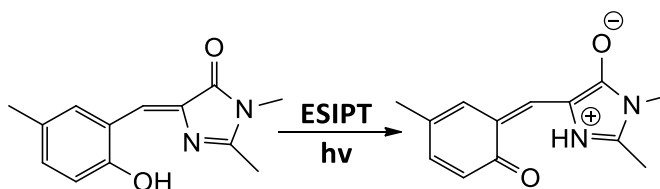
Figura 10 - Representação do processo de transferência protônica intramolecular para a HBDI representando os tautômeros enol(1) e ceto(2).

Duas estruturas têm sido sugeridas na literatura, uma utilizando o grupo meta-HBDI, que apresenta o processo ESIPT em solventes polares, e a orto-HBDI que apresenta o mesmo processo em solventes apolares, como o cicloexano, em torno de 605 nm. Podendo a estrutura orto ser empregada também em filmes sólidos originando o processo ESIPT e emitindo fluorescência na faixa de 595 nm.[35] Do ponto de vista químico, modificações na estrutura da HBDI tem apresentado emissão de cor que pode ser atribuído ao efeito do substituinte, uma vez que grupos retiradores de elétrons aumentaram a força da ligação OH diminuindo o processo ESIPT, e grupos doadores diminuíram a força da ligação OH aumentando as emissões do processo.[35]

3.3. Sondas para ânions

As sondas para fluoreto (F⁻) são as mais reportadas, apesar de possuírem algumas limitações na determinação e na formação de bioimagem.[7] Os sensores para fluoreto tem relativa importância, por ser um fator crucial na cárie e na osteoporose.[6,36] Uma variedade de sondas espectroscópicas para fluoreto têm sido desenvolvidas e três métodos analíticos são empregados para detectar o flúor: 1) a utilização de quimiossensores derivados de organoboro, que promovem a formação da ligação B – F, apropriados para o monitoramento de fluoreto em água potável ou de agentes químicos que contenham flúor, como o Sarin, (Figura 11). 2) A utilização de derivados desilil-éter, no qual ocorre a formação da ligação Si – F com a quebra da ligação Si - O, no qual o sensor necessita de uma quantidade 1400 vezes maior de fluoreto para apresentar sinal; 3) A utilização de moléculas que apresentam o processo ESIPT, no qual empregam grupos amida ou ligantes com OH.[5,37]
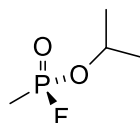
Figura 11 - Estrutura química do gás Sarin.

Dentre as sondas empregadas para fluoreto temos os derivados dos tetrazóis, que são compostos heterocíclicos de 5 membros que apresentam atividade biológica e farmacológica, e a Coumarina.[5,38] A sonda baseada em tetrazol (Figura 12) captura o íon fluoreto através de ligação com o anel imidazol (N-H), quebrando a ligação intramolecular promovendo assim a transferência de carga entre o 1H-tetrazol e o 2H-tetrazol auxiliado pelo processo ESIPT, estabilizando as estruturas ressonantes, e como consequência o ânion formado pelo anel tetrazol.[5] Na sonda, pode ocorrer a mudança de cor com a presença do

fluoreto de amarelo para incolor, o que pode auxiliar a detecção até a olho nu, permitindo uma determinação da presença de flúor.[5]

O design de sensores fluorescentes em solução aquosa tem obtido apenas limitado sucesso.[6,39] Um promissor corante fluorescente é derivado da 3-hidroxiflavona, que exibe o processo ESIPT em combinação com Zr-EDTA.[6]
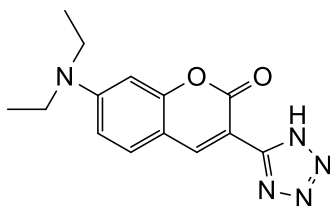
Figura 12 - Estrutura química do Tetrazol empregado como sonda fluorescente para Fluoreto.

Especial atenção é dada nos últimos anos aos ânions fosfatos, pois estes íons são essenciais para os processos biológicos.[28,40] Em particular, nucleotídeos di e trifosfato como ADP, ATP, GDP e GTP que são componentes estruturais do DNA e RNA.[28] Sensores capazes de reconhecer individualmente cada um desses compostos são importantes para o processo de comunicação químico e biológico.
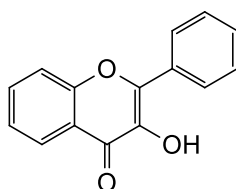
Figura 13 - Estrutura química da 3-hidroxiflavona.

O grupo de Kim e co-autores reportou, recentemente, um complexo composto por dois átomos de zinco, que foi empregado para sondas fluorescentes de pirofosfato (PPi). Esse grupo demonstrou que complexos de zinco tem a capacidade de se ligar a grupos fosfato na seguinte ordem: ADP<ATP<PPi.[28,41] O

complexo foi empregado para avaliar o comportamento de polimerização da Tubulina, que usa a energia do GTP para sofrer a polimerização.[28,42] O complexo de Zn mostrou interação com o PPi e íons de Cu(II) mostrando propriedades fluorescentes. A ligação com grupos como o ATP e GTP mostra que o complexo de Zn se forma por uma ligação forte com o grupo pirofosfato.[28,43] Na ligação com o ADP, observou-se que diferentes ânions não afetam a fluorescência e cátions Cu^{2+} e Fe^{2+} afetam negativamente a fluorescência, porém, o mercúrio parece não interferir no processo.[28,44] Como conclusão, o grupo apontou o complexo como uma sonda promissora no estudo de doenças degenerativas e para detecção de organofosfarados.[28,45]

3.4. Sondas empregadas no diagnóstico de doenças

As Alcalinefosfatases (ALP) são enzimas importantes que catalisam a hidrólise de trans-fosforilação de uma variedade de compostos fosfato. Essas enzimas são encontradas em diferentes tipos de tecidos (intestino, osso, placenta, fígado, e rim) de todos os organismos vivos.[46,47] Elas são empregadas como biomarcadores de diferentes doenças, como as relacionadas aos ossos (osteoporose, doença de Paget e osteomalacia) e ao fígado (câncer, hepatite e icterícia obstrutiva).[46,37] A avaliação da atividade da ALP é de fundamental importância para o diagnóstico preciso da doença ou para determinação dos alvos terapêuticos. Devido à sua rápida implementação, e sensibilidade, sondas fluorescentes como a fluoresceína e Coumarina, (Figura 14), são empregadas para avaliar a atividade da ALP em fluídos biológicos.[46,38]

Essas duas sondas são empregadas devido a sua alta sensibilidade, porém, elas são excretadas da célula reduzindo a aplicação endógena.[46,36] Compostos derivados da 2-(2-hidroxifenil)-4-feniltiazol, estão sendo investigados para tentar resolver os problemas de solubilidade enfrentados pelas sondas fluoresceína e coumarina, na tentativa de avaliar o diagnóstico endógeno das ALP's, com

resultados promissores.[46,48] A conversão do composto (1) em (2), (Figura 15), após a reação com a ALP promove uma forte emissão fluorescente, característica do processo ESIPT, em água e 2,0% de etanol. Quando ocorre a formação do composto (2), observa-se um forte batocromismo de 319 nm para 339 nm, resultando na formação desse composto ao longo de 10 min de reação, promovendo uma emissão azul intensa.[46,49]
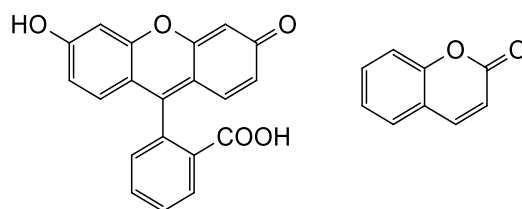
Figura 14 - Estrutura química da Fluoresceína e Coumarina.

A emissão de fluorescência em 525 nm é observada em diferentes concentrações de ALP em menos de 1 min. Possibilitando o monitoramento da atividade enzimática em tempo real pelas medidas fluorescentes.[28,50] A 3-hidroxiflavona (Figura 9), a mais abundante estrutura da classe dos flavonoides naturais, é outra classe de compostos que vem apresentando relativa importância no estudo de doenças humanas.[27,51] Essa classe de compostos, tem seu interesse por serem compostos bioativos no combate a diversos radicais livres mediados por doenças como a arteriosclerose, câncer, alergias, problemas cardíacos, inflamações e AIDS.[51,52] A 3-hidroxiflavona pode ser empregada como uma sonda fluorescente para explorar sítios ligantes em vários alvos biorrelevantes, como proteínas, membranas miméticas, como lipossomos e micelas.[28,53]

Pahari e co-autores empregaram a 3-hidroxiflavona no estudo de interações com a cavidade de ciclodextrinas para aplicações farmacológicas, mostrando grande sucesso na inserção da mesma. Porém, relataram que estudos

mais aprofundados de sua aplicação como fármaco, ainda, se fazem necessário.[51,54]
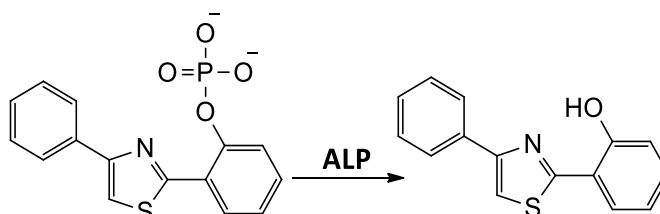
Figura 15 - Representação da ação da ALP sobre a sonda (1) que apresenta uma fluorescência azul sendo transformada em (2) que apresenta uma fluorescência verde forte.

A substituição na posição 4 da 3-hidroxiflavona por grupos dialquil amina, promove mudanças no processo ESIPT, uma vez que o grupo é um doador de elétrons por ressonância para o oxigênio da carbonila por excitação, aumentando o momento de dipolo para o estado excitado (N*) relativo ao tautômero excitado (T*), quando comparado ao seus estado normal (N) e tautômero (T) no estado fundamental.[27,54] Observou-se que N* é estabilizado por solventes polares e que o solvente aumenta a barreira energética de transferência.[27,55] Para tentar diminuir essa barreira é utilizado a substituição com os grupos amino na tentativa de aumentar a força de transferência do próton quando submetidos a solventes polares.[27]

A Doxorrubicina (DOX) apresenta aplicações biológicas como fármaco e características fotofísicas na transferência de prótons e elétrons.[23,56] A DOX é membro das antraciclinas dos grupos dos antibióticos, conhecida pela sua ação quimioterápica, sendo tetracíclica, contendo 3 anéis planares e um anel antraquinona aromático com uma hidroxila, e um anel não aromático composto por um grupo aminoglicosídico.[23,57]
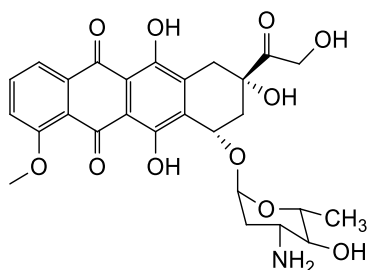
Figura 16 - Estrutura química da Doxorrubicina.

Devido a presença de diferentes grupos funcionais, ela pode se apresentar protonada dependendo do pH do meio. As propriedades fotofísicas da DOX apresentam variação com o pH do meio, exibindo fluorescência em 593 nm em solução aquosa e 577 nm em etanol. Essa diferença remete ao deslocamento atribuído a mudanças estruturais adotados em diferentes solventes, mais apolar (protonado) e polar (desprotonado), sugerindo que o solvatocromismo na DOX é determinado pelo ambiente local, mudando a polaridade do composto.[23,58] Seu interesse vem se reforçando, uma vez que pesquisas demonstram sua ação contra linhagens de células tumorais altamente resistentes "in vitro".[23,59] A DOX atua sobre a Topoisomerase II, além de impedir a geração de radicais livres dentro da célula. A DOX apresenta características fluorescentes intrínsecas podendo ser usada para sondas e empregado em várias técnicas de imagem. Alguns estudos têm focado na utilização da DOX no monitoramento da ligação com DNA, outros para o monitoramento de culturas de células por fluorescência.[23,60]
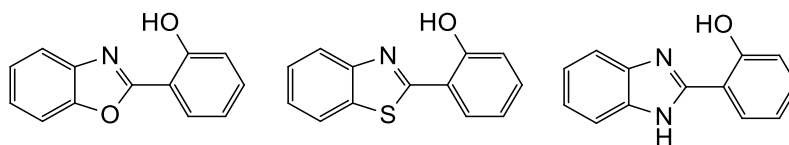
Figura 17 - Estrutura química da 2-(2'-hidroxifenil)benzoxazol, 2-(2'-hidroxifenil)benzotiazol e 2-(2'-hidroxifenil)benzimidazol, respectivamente.

A classe de compostos derivados dos 2-(2'-hidroxifenil)benzazol, como o 2-(2'-hidroxifenil)benzoxazol, 2-(2'-hidroxifenil)benztiazol e 2-(2'-hidroxifenil)benzimidazol (ver figura 2), apresentam fluorescência devido ao processo ESIPT, possuindo seus derivados uma ampla aplicação, como laser, materiais poliméricos e estabilizantes, sendo reportados por muitos grupos de pesquisa.[13,21,61,62,63,64,65] Um dos derivados, o composto 2,1,3-benzothidiazole (BTD) e seus derivados, apresentam detecção seletiva da dupla fita de DNA (dsDNA) em células vivas, sendo uma candidata a utilização em estudos de imagem, uma vez que, podem atravessar a membrana de células e se ligar seletivamente e eficientemente ao dsDNA. Outro exemplo, são os derivados aminobenzazoles sintetizados a partir dos 2-(2'-hidroxiphenil)benzozazoles e orto-anilinas. Esses compostos apresentam emissão fluorescente verde e potencial para aplicação biológica e médica, sendo aplicados para determinação de proteínas em meio aquoso, como a albumina (BSA).[63]

4. Considerações Finais

Os estudos de sondas fluorescentes aplicados a diferentes sistemas passam por estudos teóricos e experimentais, assim, como pelo entendimento dos seus mecanismos de ação e de aplicabilidade. Sendo necessários, ainda, estudos cada vez mais abrangentes para aplicação dessas sondas em organismos vivos. A utilização de sondas fluorescentes em diferentes ambientes surge como uma promissora técnica para a detecção de compostos de interesse ambiental, medicinal e bioquímico. O desenvolvimento de pesquisas para entender melhor o processo ESIPT pode auxiliar na criação de métodos para aplicação clínica, como o diagnóstico de tumores e problemas neurodegenerativos. Desta forma, novas pesquisas para aperfeiçoar a técnica de espectroscopia de fluorescência e a aplicação dessas sondas se fazem necessárias para que se produzam mecanismos de diagnóstico mais eficientes, que possam reduzir a mortalidade.

REFERÊNCIAS BIBLIOGRÁFICAS

[1] Chaudhuri, S.; Pahari, B.; Sengupta, P. K. Ground and excited state proton transfer and antioxidant activity of 7-hydroflavone in model membranes: Absorption and fluorescence spectroscopic studies. *Biophysical Chemistry* **2009**, *139*, 29.

[2] Lue , N.; Kang, J. W.; Yu, C. C.; Barman, I.; Dingari, N. C.; Feld, M. S.; Dasari, R. R.; Fitzmaurice, M. Portable optical fiber probebased spectroscopic scanner for rapid cancer diagnosis: A New tool for intraoperative margin assessment. *PLoS One* **2012**, *7*, e30887.

[3] Beleites, C.; Steiner, G.; Sowa, M. G.; Baumgartner, R.; Sobottka, S.; Schackert, G.; Salzer, R. Classification of Human gliomas by infrared imaging spectroscopy and chemometric image processing. *Vibrational Spectroscopy* **2005**, *38*, 143.

[4] Sepanovic, O. R.; Volynskaya, Z.; Kong, C. R.; Galindo, L. H.; Dasari, R. R.; Feld, M. S. A multimodal spectroscopy system for realtime disease diagnosis. *Review Scientific Instruments* **2009**, *80*, 1.

[5] Li , J. Y.; Zhou, X. Q.; Zhou, Y.; Fang, Y.; Yao C. A highly specific tetrazole-based chemosensor for fluoride ion: a new sensing functional group based on intramolecular proton transfer. *Spectrochimica Acta Part A:Molecular and Biomolecular Spectroscopy* **2013**, *102*, 66.

[6] Wang, F.; Wu, J.; Zhuang, X.; Zhang, W.; Liu, W.; Wang, P.; Wu, S. A highly selective fluorescent sensor for fluoride in aqueous solution based on the

inhibition of excited state intramolecular proton transfer. *Sensors and Actuators B: Chemical* **2010**, *146*, 260.

[7] Zhu , B.; Kan, H.; Liu, J.; Liu, H.; Wei, Q.; Du, B. A highly selective ratiometric visual and red-emitting fluorescent dual-channel probe for imaging fluoride anions in living cells. *Biosensors and Bioelectronics* **2014**, *52*, 298.

[8] Doroshenko, A. O.; Matsakov, A. Y.; Nevskii, O. V.; Grygorovych, O. V. Excited state intramolecular proton transfer reaction revisited: S1 state or general reversibility? *Journal of Photochemistry and Photobiology A: Chemistry* **2012**, *250*, 40.

[9] Paul, B. K.; Samanta, A.; Guchhait, N. Modulation of Excited-State Intramolecular Proton Transfer Reaction of 1-hydroxy-2-naphthaldehyde in Different Supramolecular Assemblies. *Langmuir* **2010**, *26*, 3214.

[10] Basarić, N.; Cindro, N.; Hou, Y.; Žabčić, I.; Mlinarić-Majerski, K.; Wan, P. Competing photodehydration and excited-state intramolecular proton transfer (ESIPT) in adamantyl derivates of 2-phenylphenols. *Canadian Journal of Chemistry* **2011**, *89*, 221.

[11] Lee, J.; Kim, C. H.; Joo, T. Active role of proton in excited state intramolecular proton transfer reaction. *Journal of Physical Chemistry A* **2013**, *117*, 1400.

[12] Enchev, V.; Markova, N.; Stoyanova, M.; Petrov, P.; Rogozherov, M.; Kuchukova, N.; Timtcheva, I.; Monev, V.; Angelova, S.; Spassova, M. Excited state proton transfer in 3,6-bis(4,5-dihydroxyoxazo-2-yl)benzene-1,2-diol. *Chemical Physics Letters* **2013**, *563*, 43.

[13] Goswami , S.; Das, A. K.; Aich, K.; Manna, A. Competitive intra- and inter-molecular proton transfer in hydroxy-naphthyl benzothiazole: selective ratiometric sensing of acetate. *Tetrahedron Letters* **2013**, *54*, 4215.

[14] Deperasińska, I.; Gryko, D. T.; Karpiuk, E.; Kozankiewicz, B.; Makarewicz, A.; Piechowska, J. 12-Hydroxy-1-azaperylene -Limiting Case of the ESIPT

System: Enol-Keto Tautomerization in S0 and S1 States. *Journal of Physical Chemistry A* **2012**, *116*, 2109.

[15] Nibbering, E. T. J.; Fidder, H.; Pines, E. Ultrafast Chemistry: Using time-resolved vibrational spextroscopy for interrogation of structural dynamics. *Annual Reviews of Physical Chemistry* **2005**, *56*, 337.

[16] Tang, K.-C.; Chen, C.-L.; Chuang, H.-H.; Chen, J.-L.; Chen, Y.-J.; Lin, Y.-C.; Shen, J.-Y.; Hu, W.-P.; Chou, P.-T. A Genuine intramolecular proton relay system undergoing excited-state double proton transfer reaction. *Journal of Physical Chemistry Letters* **2011**, *2*, 3063.

[17] Mahajan, A.; Aulakh, R. K.; Bedi, R. K.; Kumar, S.; Kumar, S.; Aswal, D. K. Synthesis and characterization of excited state intramolecular proton transfer based 2-hydroxylaryl imidazole fluorescent materials. *Synthetic Metals* **2012**, *162*, 58.

[18] Brenlla, A.; Rodríguez-Prieto, F.; Mosquera, M.; Ríos, M. A.; Ríos Rodríguez, M. C. Solvent-Modulated Ground-State Rotamerism and Tautomerism and Excited-State Proton-Transfer Processes in o-Hydroxynaphthylbenzimidazoles. *Journal of Physical Chemistry A* **2009**, *113*, 56.

[19] Yang, G. Q.; Li, S.; Wang, S.; Li, Y. Emissive properties and aggregation-induced emission enhancement of excited-state intramolecular proton-transfer compounds. *Comptes Rendus Chimie* **2011**, *14*, 789.

[20] Daengngern, R.; Kerdpol, K.; Kungwan, N.; Hannongbua, S.; Barbatti, M. Dynamics simulations of excited-state triple proton transfer in 7-azaindole complexes with water, water-methanol and methanol. *Journal of Photochemistry and Photobiology A: Chemistry* **2013**, *266*, 28.

[21] Patil, V. S.; Padalkar, V. S.; Phatangare, K. R.; Gupta, V. D.; Umape, P. G.; Sekar, N. Synthesis of new ESIPT-Fluorescein: Photophysics of pH sensitivity and fluorescence. *Journal of Physical Chemistry A* **2012**, *116*, 536.

[22] Tang, K. C.; Chang, M. J.; Lin, T. Y.; Pan, H. A.; Fang, T. C.; Chen, K. Y.; Hung, W. Y.; Hsu, Y. H.; Chou, P. T. Fine Tuning the Energetics of Excited-State intramolecular Proton transfer (ESIPT): White ligth generation in a single ESIPT system. *Journal of the American Chemical Society* **2011**, *133*, 17738.

[23] Rana, D. K.; Dhar, S.; Sarkar, A.; Bhattacharya, S. C. Dual intramolecular hydrogen bond as a switch for inducing ground and excited-state intramolecular double proton transfer in doxorubicin: an excitation wavelength dependence study. *Journal of Physical Chemistry A* **2011**, *115*, 9169.

[24] Lukeman, M.; Burns, M.-D.; Wan, P. Excited state intramolecular proton transfer in 1-hydroxypyrene. *Canadian Journal of Chemistry* **2011**, *89*, 433.

[25] Lin, T. Y.; Tang, K. C.; Yang, S. H.; Shen, J. Y.; Cheng, Y. M.; Pan, H. A.; Chi, Y.; Chou, P. T. The empirical Correlation between Hydrogen Bonding Strength and Excited-State intramolecular Proton Transfer in 2-Pyridyl Pyrazoles. *The Journal of Physical Chemistry A* **2012**, *116*, 4438.

[26] Chung, M. W.; Lin, T. Y.; Hsieh, C. C.; Tang, K. C.; Fu, H.; Chou, P. T.; Yang, S. H.; Chi, Y. Excited-State Intamolecular Proton Transfer (ESIPT) fine Tuned by Quinoline-Pyrazole Isomerism: π-Conjugation Effect on ESIPT. *Journal of Physical Chemistry A* **2010**, *114*, 7886.

[27] Lin, C. C.; Chen, C. L.; Chung, M. W.; Chen, Y. J.; Chou, P. T. Effects of Multibrnching on 3-Hydroxyflavone-Based chromophores and the excited-state intramolecular proton transfer dynamics. *Journal of Physical Chemistry A* **2010**, *114*, 10412.

[28] Kim, K.; Ha, Y.; Kaufman, L.; Churchill, D. G. Labile Zinc-Assisted Biological Phosphate Chemosensing and Related Molecular Logic Gating Interpretations. *Inorganic Chemistry* **2012**, *51*, 928.

[29] Mech, J.; Grela, M. A.; Szaciłowski, K. Ground and excited state properties of alizarin and its isomers. *Dyes and Pigments* **2014**, *103*, 202.

[30] Helal, A.; Kim, H. S. Carbazole incorporated ratiometric chemosensor for Zn^{2+}. *Spectrochimica Acta Part A: Molecular and Biomolecular Spectroscopy* **2013**, *105*, 273.

[31] Strizhak, A. V.; Postupalenko, V. Y.; Shvadchak, V. V.; Morellet, N.; Guittet, E.; Pivovarenko, V. G.; Klymchenko, A. S.; Mély, Y. Two-Color fluorescent L-amino acid mimic of tryptophan for probing peptide-nucleic acid complexes. *Bioconjugate Chemistry* **2012**, *23*, 2434.

[32] Kazmierczak, S. C.; Gurachevsky, A.; Matthes, G.; Muravsky, V. Electron Spin Resonance Spectroscopy of Serum Albumin: A Novel New Test for Cancer Diagnosis and Monitoring. *Clinical Chemistry* **2006**, *52*, 2129.

[33] Samanta, A.; Paul, B. K.; Guchhait, N. Spectroscopic probe for exploring probe protein interaction: a mapping of native, unfolding and refolding of protein bovine serum albumin by extrinsic fluorescence probe. *Biophysical Chemistry* **2011**, *156*, 128.

[34] Srikun, D.; Albers, A. E.; Nam, C. I.; Iavarone, A. T.; Chang, C. J. Organelle targetable fluorescent probes for imaging hydrogen peroxide in living cells via SNAP-Tag protein labeling. *Journal of the American Chemical Society* **2010**, *132*, 4455.

[35] Garcia, E.; Andrews, C.; Hua, J.; Kim H. L.; Sukumaran, D. K.; Szyperski, T.; Odunsi, K. Diagnosis of Early Stage Ovarian Cancer by 1H NMR metabonomics of Serum Explored by use of a Microflow NMR probe. *Journal of Proteome Research* **2011**, *10*, 1765.

[36] Saroj, M. K.; Sharma, N.; Rastogi, R. C. Photophysical study of some 3-benzoylmethyleneindol-2-ones and estimation of ground and escited states dipole moments from solvatochromic methods using solvent polarity parameters. *Journal of Molecular Structure* **2012**, *1012*, 73.

[37] Sekikawa, T.; Schalk, O.; Wu, G.; Boguslavskiy, A. E.; Stolow, A. Initial Processes of proton transfer in salicylideneaniline studied by time resolved photoelectron Spectroscopy. *Journal of Physical Chemistry A* **2013**, *117*, 2971.

[38] Shen, X. F.; Wang, F.; Xu, S.; Qian, Y.; Liu, Y.; Yuan, H.; Zhao, Q.; Feng, S.; Guo, X.; Xu, J.; Yang, J. Is cardiolipin the target of local anesthetic cardiotoxicity? *Brazilian Journal of Anesthesiology* **2010**, *60*, 445.

[39] Zhao, X. D.; Sun, C. J.; Yao, Q. Q.; Li, W. B. Synthesis of 3-hydroxyflavone fluorescent probes and study of their fluorescence properties. *Chinese Chemical Letters* **2010**, *21*, 529.

[40] Yu, C.; Gestl, E.; Eckert, K.; Allara, D.; Irudayaraj, J. Characterization of human breast epithelial cells by confocal Raman microspectroscopy. *Cancer Detection Prevention* **2006**, *30*, 515.

[41] Valchanov, G.; Ivanova, A.; Tadjer, A.; Chercka, D.; Baumgarten, M. Tuning the optical absorption of potencial blue emitters. *Organic Electronics* **2013**, *14*, 2727.

[42] Wang, J.; Chu, Q.; Liu, X.; Wesdemiotis, C.; Pang, Y. Large fluorescence response by alcohol from a bis(benzoxazole)-Zinc(II) complex: The role of excited state intramolecular proton transfer. *Journal of Physical Chemistry B* **2013**, *117*, 4127.

[43] Tomin, V. I.; Jaworski, R. ESIPT may proceed in 3HF at excitation in S2 state. *Journal of Molecular Structure* **2012**, *1030*, 104.

[44] Zhang, W.; Yang, T.; Jiao, K. Ultrasensitive indicator-free and enhanced self-signal nanohybrid DNA sensing platform based on electrochemically grown poly-xanthurenic acid/Fe2O3. *Biosensensors Bioelectronics* **2012**, *31*, 182.

[45] Stolow, A. Femtosecond time-resolved photoelectron spectroscopy of polyatomic molecules. *Annual Reviews of Physical Chemistry* **2003**, *54*, 89.

[46] Park, J.; Helal, A.; Kim, H. S.; Kim, Y. Fluorogenic assay of alkaline phosphatase activity based on the modulation of excitedstate intramolecular proton transfer. *Bioorganic & Medicinal Chemistry Letters* **2012**, *22*, 5541.

[47] Steiner, G.; Shaw, A.; Choo-Smith, L. P.; Abuid M. H.; Schackert, G.; Sobottka, S.; Steller, W.; Salzer, R.; Mantsch, H. H. Distinguishing and grading human gliomas by IR spectroscopy. *Biopolymers* **2003**, *72*, 464.

[48] Rosspeintner, A.; Lang, B.; Vauthey, E. Ultrafast Photochemistry in Liquids. *Annual Reviews of Physical Chemistry* **2013**, *64*, 247.

[49] Ju, C. C.; Yin, H. J.; Yuan, C. L.; Wang, K. Z. A fluorescent probe for both pH and Zn^{2+} based on 2-(1-phenyl-1H-benzo[d]imidazol-2-yl)phenol. *SpectrochimicaActa Part A: Molecular and Biomolecular Spectroscopy* **2011**, *79*, 1876.

[50] Jayabharathi, J.; Thanikachalam, V.; Kalaiarasi, V.; Jayamoorthy, K. Intramolecular excited charge transfer, radiative and radiationless charge recombination processes in donor-acceptor imidazole derivatives. *Journal of Photochemistry and Photobiology A: Chemistry* **2014**, *275*, 114.

[51] Pahari, B.; Chakraborty, S.; Sengupta, P. K. Encapsulation of 3-hydroxyflavone in Ƴ-ciclodextrin nanocavities: Excited state proton transfer fluorescence and molecular docking studies. *Journal of Molecular Structure* **2011**, *1006*, 483.

[52] Banerjee, S.; Pabbathi, A.; Sekhar, M. C.; Samanta, A. Dual Florescence of Ellipticine: Excited State Proton Transfer from Solvent versus Solvent mediated intramolecular Proton Transfer. *Journal of Physical Chemistry A* **2011**, *115*, 9217.

[53] Chuang, W. T.; Hsieh, C. C.; Lai, C. H.; Lai, C. H.; Shih, C. W.; Chen, K. Y.; Hung, W. Y.; Hsu, Y. H.; Chou, P. T. Excited-State Intramolecular Proton transfer molecules bearing o-hydroxy analogues of Green Fluorescent Protein Chromophore. *The Journal of Organic Chemistry* **2011**, *76*, 8189.

[54] Chandra, M.; Scheiman, J.; Heidt, D.; Simeone, D.; McKenna, B.; Mycek, M. A. Probing pancreatic disease using tissue optical spectroscopy. *Journal Biomedical Optics* **2007**, *12*, 060501.

[55] Goldberg, J. M.; Batjargal, S.; Petersson, E. J. Thioamides as fluorescence Quenching probes: Minimalist Chromophores to Monitor Protein Dynamics. *Journal of the American Chemical Society* **2010**, *132*, 14718.

[56] Chen, W.-H.; Pang, Y. Excited-state intramolecular proton transfer in 2-(2',6'-dihydroxyphenyl)benzoxazole: effect of dual hydrogen bonding on the optical proprieties. *Tetrahedron Letters* **2010**, *51*, 1914.

[57] Erez, Y.; Presiado, I.; Gepshtein, R.; Huppert, D. Excited-State intermolecular Proton transfer of Firefly Luciferin IV. Temperature and pH Dependence. *Journal of Physical Chemistry A* **2011**, *115*, 1617.

[58] Hsieh, C. C.; Jiang, C. M.; Chou, P. T. Recent Experimental advances on Excited-State intramolecular Proton Coupled Electron Transfer Reaction. *Accounts of Chemical Research* **2010**, 43, 1364.

[59] Erez, Y.; Simkovitch, R.; Shomer, S.; Gepshtein, R.; Huppert, D. Effect of Acid on the Ultraviolet-Visible Absorption and Emission Properties of Curumin. *Journal of Physical Chemistry A* **2014**, *118*, 872.

[60] Fang, T.-C.; Tsai, H.-Y.; Luo, M.-H.; Chang, C.-W.; Chen, K.-Y. Excited-State charge coupled proton transfer reaction via the dipolar functionality of salicylideneaniline. *Chinese Chemical Letters* **2013**, *24*, 145.

[61] Oliveira, F. F. D.; Santos, D. C.; Lapis, A. A.; Corrêa, J. R.; Gomes, A. F.; Gozzo, F. C.; Moreira, P. F. Jr.; de Oliveira, V. C.; Quina, F. H.; Neto B. A. On the use of 2,1,3-benzothiadiazole derivatives as selective live cell fluorescence imaging probes. *Bioorganic & Medicinal Chemistry Letters* **2010**, *20*, 6001.

[62] Coelho, F. L.; Rodembusch, F. S.; Campo, L. F. Synthesis, characterization and photophysics of new photoactive ESIPT lipophilic dyes. Partition experiments with different composed liposomes. *Dyes and Pigments* **2014**, *110*, 134.

[63] Holler, M. G.; Campo, L. F.; Brandelli, A.; Stefania, V. Synthesis and spectroscopic characterization of 2-(2'-hydroxiphenyl)benzazole isothiocyanates as new fluorescent probes for proteins. *Journal of Photochemistry and Photobiology A: Chemistry* **2002**, *149*, 217.

[64] Dick, P. F.; Faleiro, N. V. S.; Campo, L. F.; Scroferneker, M. L.; Corbellini, V. A.; Rodembusch, F. S.; Stefani, V. Amphiphilic ESIPT benzoxazole derivates as prospective fluorescent membrane probes. *Tetrahedron Letters* **2014**, *55*, 3024.

[65] Grando, S. R.; Pessoa, C. M.; Gallas, M. R.; Costa, T. M.; Rodembusch, F. S.; Benvenutti, E. V. Modulation of the ESIPT Emission of Benzothiazole Type Dye Incorporated in Silica-Based Hybrid Materials. *Langmuir* **2009**, *25*, 13219.

2. REFERENCIAL TEÓRICO

2.1. Teoria do Funcional de Densidade (DFT)

O desenvolvimento da moderna Teoria do funcional de Densidade (DFT) começou em meados dos anos 60, e, combinado ao progresso da tecnologia computacional fez desse método um dos mais populares no final do século 20 (CHERMETTE, 1998; GÖRLING, 2005; NEESE, 2009; PANTAZIS et al., 2008; TSIPIS, 2014). Em 1964, Pierre Hohenberg e Walter Kohn mostraram que a equação de Schrödinger, formulada como uma equação de N-elétrons com uma função de onda de 3N variáveis, poderia ser reformulada como uma equação da densidade (TSIPIS, 2014). Desta forma, o teorema de Hohenberg e Kohn (HK) estabelece que o estado fundamental de um sistema eletrônico pode ser descrito por um funcional de densidade eletrônico, que em princípio, precisa do conhecimento da densidade para se calcular as demais propriedades do sistema (CHERMETTE, 1998; NEESE, 2009; TSIPIS, 2014).

Uma das etapas importantes para aplicar a DFT a sistema reais foi proposta por Khon e Sham em 1965, quando publicaram as equações de Kohn-Sham (KS) derivadas do teorema de HK. Segundo o teorema de HK, a densidade eletrônica, $\rho(x)$ representa o número de vezes (N) da probabilidade de encontrar um elétron na posição x independente do spin. Dessa forma, a densidade de spin pode ser escrita conforme a equação 1,

$$\rho^{\alpha-\beta}(x) = \rho^{\alpha}(x) - \rho^{\beta}(x) \tag{1}$$

Ao aplicar a equação de Schrödinger para a interação dos elétrons em um potencial externo, o potencial KS ($v_{KS}[n](r)$) é definido como a soma do potencial externo, o termo de Hartree e o potencial de troca e correlação (XC), de acordo com a equação 2,

$$v_{KS}[n](r) = v_{ext}[n](r) + v_{hartree}[n](r) + v_{XC}[n](r) \qquad (2)$$

O potencial externo é tipicamente a soma dos potenciais nucleares centrados nas posições atômicas descrito na equação 3,

$$v_{ext}[n](r) = \sum v_\alpha(r - R_\alpha) \qquad (3)$$

Em que v_α é a atração Coulombica entre a barreira nuclear e os elétrons, $v_\alpha(r) = -\frac{Z_\alpha}{r}$, em que Z_α é a carga nuclear. O potencial de Hartree é definido na equação 4,

$$v_{KS}[n](r) = \int d^3r' \frac{n(r')}{|r-r'|} \qquad (4)$$

O potencial de troca, que é definido através do funcional derivado da energia de troca e correlação, E_{XC}, é apresentado na descrição da equação 5,

$$v_{KS}[n](r) = \frac{\delta E_{XC}}{\delta n(r)} \qquad (5)$$

Nos últimos 40 anos, muitos funcionais DFT foram desenvolvidos para resolver essa aproximação, a consequência disso é a solução de vários problemas químicos (MUSIC; GEYER; SCHNEIDER, 2016; SAN-MIGUEL et al., 2016). Na teoria KS, a energia total pode ser simplificada na equação 6,

$$E_{total} = v_{NN} + v_{eN}[\rho] + J[\rho] + T[\rho] + v_{XC}[\rho] \qquad (6)$$

No qual $J[\rho]$ é termo da energia cinética, $T[\rho]$ é o termo da energia potencial, $v_{XC}[\rho]$ é o termo da energia de troca e correlação e $v_{eN}[\rho]$ é o termo da

interação núcleo e elétron. O termo de repulsão de Coulomb, v_{NN}, conta para as interações descritas na equação 7,

$$v_{NN} = \sum_{\alpha,\beta} \frac{Z_\alpha Z_\beta}{|R_\alpha - R_\beta|} \tag{7}$$

2.1.1. Os funcionais DFT

2.1.1.1. Funcionais do tipo LDA.

O termo do potencial de troca e correlação, $v_{XC}[\rho]$, foi determinado pela aproximação da densidade local (Local Density Approximation, LDA), no qual apenas os elétrons em um ponto do sistema são usados para determinar os pontos que contribuem para a $v_{XC}[\rho]$ total do sistema (CHARAF-EDDIN et al., 2013; CHERMETTE, 1998; TSIPIS, 2014). As energias de correlação foram propostas desde 1970 por Vosko, Perdew e Zunger. Nos anos 80, Perdew e Wang desenvolveram funcionais LDA que são considerados limiares para este nível de aproximação (ANNARAJ et al., 2014; CHERMETTE, 1998; TSIPIS, 2014). Quando a energia de troca e correlação se diferencia lentamente com a posição espacial, ela possui a equação descrita em 8,

$$E_{XC}[n] = \int dr^3 n(r)\xi_{XC}(n(r)) \tag{8}$$

Em que E_{XC} é a energia de troca e correlação por partícula em uma densidade de elétron n(r).

A generalização do funcional LDA, que se aplica a orbitais espacialmente diferentes para elétrons com spin opostos, ficou conhecida como Aproximação da densidade de spin local (Local spin density approximation, LSDA). Os funcionais do tipo LSDA apresentam melhores resultados para moléculas com campo aberto e geometria molecular próximos da dissociação (CHERMETTE, 1998; NEESE,

2009; TSIPIS, 2014). O funcional de troca e correlação LSDA pode ser escrito como a equação 9,

$$E_{XC}[n^\alpha, n^\beta] = \int d^3r\, n(r)\xi_{XC}(n^\alpha(r), n^\beta(r)) \tag{9}$$

2.1.1.2. Funcionais do tipo GGA.

Uma melhoria aplicada aos funcionais LDA e LSDA foi a implementação do gradiente de densidade, $n^\alpha(r)$ e $n^\beta(r)$, a integral dos funcionais, gerando uma expansão de funcionais conhecida como Aproximação do Gradiente Generalizado (Generalized Gradient Approximation, GGA). O primeiro funcional de gradiente corrigido foi proposto em 1986 por Becke, Perdew e Wang para a troca e Perdew para a correlação eletrônica (BP86) (CHERMETTE, 1998; GRITSENKO; SCHIPPER; BAERENDS, 1997; TSIPIS, 2014).

A incorporação dos gradientes de densidade eletrônica aos funcionais LDA e LSDA apresenta a forma da equação 10,

$$E_{XC}[n^\alpha, n^\beta] = \int d^3r\, \xi_X{}^{GGA}(n^\alpha(r), n^\beta(r), \nabla n^\alpha(r), \nabla n^\beta(r)) \tag{10}$$

2.1.1.3. Funcionais do tipo Meta-GGA

Os funcionais que incorporam a densidade eletrônica, seus gradientes e o laplaciano de suas densidades e/ou a energia cinética orbital (interação semi-local) são conhecidos como funcionais meta-GGA, e apresentam a relação descrita na equação 11 (CHERMETTE, 1998; GRITSENKO; SCHIPPER; BAERENDS, 1997; TSIPIS, 2014),

$$E_{XC}[n^\alpha, n^\beta] = \int d^3r\, \xi_X{}^{GGA}(n^\alpha(r), n^\beta(r), \nabla n^\alpha(r), \nabla n^\beta(r), \nabla^2 n^\alpha(r), \nabla^2 n^\beta(r), \tau^\alpha, \tau^\beta) \tag{11}$$

Sendo τ^α a energia cinética orbital KS, $\nabla^2 n^\alpha(r)$ o Laplaciano da

densidade (TSIPIS, 2014).

2.1.1.4. Funcionais do tipo Híbrido

Em 1993, Becke propôs uma mistura dos funcionais GGA com funcionais de troca LSDA. Os funcionais de troca LSDA são descritos como $E_X{}^{XC}$ e empregam a definição de Hartree-Fock para a energia de troca. Os funcionais híbridos substituem parte do funcional de troca com funcionais de troca não locais calculados pela teoria Hartree-Fock, E_{HF-X} (CHERMETTE, 1998; HERTWIG; KOCH, 1997; TSIPIS, 2014; YANAI; TEW; HANDY, 2004). Esses funcionais podem ser escritos de acordo com a equação 12 e 13,

$$E_{XC}[n] = \int d^3 r \xi_X\big(n(r), \nabla n(r)\big) + \alpha_X \xi_{HF-X} + \int \xi_C(n(r), \nabla n(r)) \qquad (12)$$

$$E_{XC} = a_0 \xi_{X(HF)} + a_1 \xi_{X(LSDA)} + a_2 \xi_{X(GGA)} + a_3 \xi_C \qquad (13)$$

Sendo $E_{X(HF)}$ a energia de troca pura, a qual é calculada a partir da metodologia HF; $E_{X(LSDA)}$ é a energia local de troca empregando a aproximação da densidade de spin local para a energia de troca; $E_{X(GGA)}$ é a energia de correção do gradiente generalizado para a energia de troca, chamado de Be88; E_C a energia de correlação do gradiente corrigido, chamado de Lee-Yang-Parr (LYP), com $a_1 = 1.0 - a_0$ (CHERMETTE, 1998; GUAN et al., 1993; MARIAM; MUSIN, 2001; TSIPIS, 2014).

2.1.1.5. Funcionais híbridos duplos

Os funcionais híbridos duplos são funcionais que calculam parte da energia de correlação por outros métodos *ab initio*, por exemplo, o método MP2, como descrito na equação 14 (CHERMETTE, 1998; DABBAGH et al., 2014;

TSIPIS, 2014):

$$E_{XC}[n] = \int d^3r \xi_X\big(n(r), \nabla n(r)\big) + \alpha_X \xi_{HF-X} + (1 - \alpha_C) \int \xi_C(n(r), \nabla n(r)) + \alpha_C \xi_{MP2} \ (14)$$

Os funcionais híbridos duplos combinam os cálculos padrão dos funcionais híbridos-GGA com um tratamento perturbativo de segunda ordem com orbitais KS (HERTWIG; KOCH, 1997; JACQUEMIN et al., 2008b).

2.1.1.6. Funcionais de Longo Alcance

Os funcionais de longo alcance (range-separated hybrid functionals, RSHF) são baseados na separação da interação elétron-elétron em 2 partes, uma de longo alcance e outra de curto alcance, tratando ambas as partes de maneira diferente (CHERMETTE, 1998; TSIPIS, 2014).

2.2. Teoria do Funcional de Densidade Dependente do Tempo

A teoria do funcional de Densidade dependente do tempo estabelece a dependência do tempo (TD) para a densidade eletrônica como o principal objeto de estudo para entender a dinâmica de sistemas moleculares. TDDFT é usualmente empregada para cálculos de propriedades espectroscópicas de moléculas e sólidos (KRISHNA, 2009; MOSQUERA, 2013; RUGGENTHALER; PENZ; VAN LEEUWEN, 2015). A teoria TDDFT tem sido aplicada a muitos problemas de física ou química empregadas para moléculas de diferentes tamanhos (CASIDA; HUIX-ROTLLANT, 2012; RUGGENTHALER; PENZ; VAN LEEUWEN, 2015).

O formalismo da TDDFT pode ser descrito incialmente considerando a equação de Schrödinger dependente do tempo para um sistema de N elétrons, conforme descrito na equação 15,

$$i\partial_t\psi(x,t) = \hat{H}(t)\psi(x,t) \tag{15}$$

Em que x é a coleção de variáveis espaciais e de spin do sistema. O operador Hamiltoniano $\hat{H}(t)$ tem a estrutura descrita na equação 16,

$$\hat{H}(t) = \hat{T} + \hat{W} + \hat{V}(t) \tag{16}$$

Em que $\hat{T}$ representa o operador energia cinética, $\hat{V}(t)$ o potencial externo dependente do tempo e $\hat{W}$ as interações de dois elétrons. Especificando cada termo, temos as descrições das equações 17, 18 e 19, respectivamente,

$$\hat{T} = -\frac{1}{2}\sum_{j=1}^{N} \nabla_j{}^2 \tag{17}$$

$$\hat{V}(t) = \sum_{j=1}^{N} v(r_j, t) \tag{18}$$

$$\hat{W} = \sum_{i>j}^{N} w(r_i - r_j) \tag{19}$$

Dentre os desafios da TDDFT, encontram-se a descrição correta da transferência de carga entre estados excitados, o transporte de elétron através de uma molécula conectada a um centro metálico, a geração de harmônicos de alta ordem e de duplas excitações e interações de van der Waals (MOSQUERA; JENSEN; WASSERMAN, 2013; RUGGENTHALER; PENZ; VAN LEEUWEN, 2015).

2.3. Efeitos Relativísticos de átomos e moléculas

Os efeitos relativísticos são especialmente importantes para sistemas que contenham átomos pesados, ou seja, para átomos com alta massa molecular (NAKAJIMA; HIRAO, 2000; NAKAJIMA; SUZUMURA; HIRAO, 1999). Enquanto a descrição de Schrödinger não relativística é suficiente para elementos

leves, uma descrição mais geral pode ser desenvolvida conciliando os princípios da teoria da relatividade para átomos e moléculas (GORIN; TOSTE, 2007; ILIAŠ; KELLÖ; URBAN, 2010; PYYKKÖ, 2004, 2012).

A teoria da Relatividade Restrita apresenta dois postulados gerais:

1. O princípio da Relatividade descreve que as leis físicas são as mesmas em todos os referenciais inerciais;
2. A Luz se propaga com velocidade constante, c, no espaço livre.

A teoria da relatividade de Einstein descreve a energia em termos do momento e da massa, m_0, como descrito na equação 20,

$$E^2 = p^2 c^2 + {m_0}^2 c^4 \tag{20}$$

Este termo pode ser empregado no Hamiltoniano clássico para a partícula livre. Substituindo o momento clássico pelo operador momento apresentado na equação 21,

$$\hat{\rho} = -i\hbar\nabla \tag{21}$$

A energia total, então, assume a forma da equação 22,

$$i\hbar \frac{\partial \psi(r,t)}{\partial t} = \pm c\sqrt{(-\hbar^2 \nabla^2 + {m_0}^2 c^2)}\, \boldsymbol{\psi(r,t)} \tag{22}$$

O resultado da equação de onda é conhecido como a equação de Klein-Gordon. (ILIAŠ; KELLÖ; URBAN, 2010; SHIOZAKI; MIZUKAMI, 2015; VAARA; PYYKKÖ, 2003).

2.3.1. A equação de Dirac

Dirac deduziu sua função de onda relativística para um elétron empregando a forma dependente do tempo para a equação de Schrödinger descrita na equação 23 (ILIAŠ; KELLÖ; URBAN, 2010),

$$i\frac{\partial \psi}{\partial t} = \hat{\mathbb{h}}_D \boldsymbol{\psi} \qquad (23)$$

Como princípio, as transformações de Lorentz requerem que ambos os termos (tempo e espaço) sejam de primeira ordem quanto a derivada, isso não acontece com a equação independente do tempo. Dessa forma, para que a equação 29 fosse apresentasse todos os termos na mesma ordem, Dirac reformulou a equação de Schrödinger descrevendo a equação 24,

$$i\frac{\partial \psi}{\partial t} = -ic\left(\hat{\alpha}_x \frac{\partial \psi}{\partial x} + \hat{\alpha}_y \frac{\partial \psi}{\partial y} + \hat{\alpha}_z \frac{\partial \psi}{\partial z}\right) + \beta c^2 \psi \qquad (24)$$

Na qual, ele adiciona dois termos, α e β, para que a equação atendesse as transformações de Lorentz. A equação descrita por Dirac satisfaz a equação de Klein-Gordon e os termos α e β apresentam a forma das equações 25 e 26, respectivamente,

$$\hat{\alpha} = \begin{bmatrix} 0 & \hat{\sigma} \\ \hat{\sigma} & 0 \end{bmatrix} \qquad (25)$$

$$\beta = \begin{bmatrix} I & 0 \\ 0 & -I \end{bmatrix} \qquad (26)$$

A equação de Dirac pode ser escrita como uma matrix 4x4, usualmente mencionada como "Hamiltoniano de quatro componentes" para o elétron livre conforme equação 27,

$$\hat{h}_D{}^{fe} = c\hat{\alpha} \cdot \hat{\mathbf{p}} + \beta c^2 = \begin{pmatrix} c^2 I & c\hat{\alpha} \cdot \hat{\mathbf{p}} \\ c\hat{\alpha} \cdot \hat{\mathbf{p}} & -c^2 I \end{pmatrix} \tag{27}$$

A função de onda de Dirac relativística possui quatro graus de liberdade para o espaço-tempo descrita na equação 28: spin-up (α) and spin-down (β) ambos para o elétron.

$$\psi = \begin{pmatrix} \psi^L \\ \psi^S \end{pmatrix} = \begin{pmatrix} \psi^{L\alpha} \\ \psi^{L\beta} \\ \psi^{S\alpha} \\ \psi^{S\beta} \end{pmatrix} \tag{28}$$

2.3.2. Métodos Relativísticos para átomos e moléculas

A equação de Dirac de quatro componentes demanda uma capacidade computacional muito grande e sua aplicação a sistema com um número considerável de átomos é limitado (LENTHE et al., 2014). Dessa forma, métodos quase-relativísticos tem sido desenvolvido para resolver isso.

2.3.2.1. Hamiltoniano de Douglas-Kroll

A Transformação de Douglas-Kroll (DK) foi desenvolvida por Hess e colaboradores e pode desacoplar os componentes "small" e "large" da equação de Dirac na presença de um potencial externo data de 1974, e chamou a atenção da comunidade por ser um método poderoso computacionalmente para a química quântica relativística (NAKAJIMA; HIRAO, 2000; WOLF; REIHER, 2006). O hamiltoniano de DK é bem estável e apresenta fácil inclusão dos termos de correlação para os elétrons empregando os métodos quânticos não relativísticos (NAKAJIMA; HIRAO, 2000; NAKAJIMA; SUZUMURA; HIRAO, 1999). Numericamente, os resultados obtidos pelos métodos generalizados de Douglas-Kroll para sistemas de um ou alguns elétrons e suas interações com átomos

hidrogenóides apresentam valores exatos com os obtidos com a equação de Dirac (WOLF; REIHER; HESS, 2002).

A ideia central do método de Douglas-Kroll é reduzir a função de onda de quatro componentes ("large" e "small") para uma função de base contendo apenas dois componentes (removendo o termo "small") através de progressivas eliminações dessa componente. Dessa forma, o hamiltoniano generalizado para o método de Douglas-Kroll apresenta o formato da equação 29, no qual ε_k é uma matriz operador de ordem (4x4) (WOLF; REIHER; HESS, 2002).

$$H_{DKn} = \sum_{k=0}^{\infty} \varepsilon_k \qquad (29)$$

A geração dos diferentes tipos de ordens para o método se deve a decomposição e ao número de etapas a serem executadas para a eliminação do componente "small" (TSIPIS, 2014). Ordens maiores tem sido amplamente pesquisado para o Hamiltoniano DK. Muitos artigos relatam o desenvolvimento de métodos de terceira ordem, quarta ordem e até ordem infinita (BELPASSI et al., 2011; REIHER; WOLF, 2004; WOLF; REIHER; HESS, 2002). Ordens superiores tem demonstrado serem mais eficientes e aproximar cada vez mais da resolução exata da equação de Dirac, porém, o custo computacional é elevado e a aplicabilidade a sistemas maiores dificultada pela complexidade das equações (HONG; DOLG; LI, 2001; NAKAJIMA; HIRAO, 2000; NAKAJIMA; SUZUMURA; HIRAO, 1999; WOLF; REIHER; HESS, 2002).

2.3.2.2. Hamiltoniano ZORA

Um dos mais populares Hamiltonianos Escalares Relativísticos é a Aproximação Regular de Ordem Zero (Zeroth-order regular approximation, ZORA). Tanto o Hamiltoniano ZORA como o Hamiltoninano de Douglas-Kroll-Hess (DKH) foram implementados em programas que utilizam métodos DFT e

apresentam calibrações para diversos cálculos, como monohidratos, monóxidos e monofluoretos de La, Lu, Ac e Lr (HONG; DOLG; LI, 2001).

O Hamiltoniano ZORA é obtido pela expansão regular da equação de Dirac. As equações relativísticas KS são resolvidas no escalar relativístico e em casos relativísticos totais, incluindo o operador spin-órbita (FILATOV; CREMER, 2003; SADLEJ, 2006; VAN LENTHE; SNIJDERS; BAERENDS, 1996). O Hamiltoniano ZORA sem o operador spin-órbita emprega as equações de Kohn-Sham como descrito na equação 30,

$$H^{ZORA}\Phi^{ZORA} = \left(T[V] + V_{eff}[\rho]\right)\Phi^{ZORA} \tag{30}$$

No qual, T[V] é a energia cinética e a energia potencial efetiva é descrita como a soma do potencial externo, potencial de Coulomb e o potencial de troca e correlação para a densidade eletrônica, conforme a equação 31,

$$V_{eff}[\rho] = V_{ext} + V_{coul}[\rho] + V_{XC}[\rho] \tag{31}$$

Ao substituir as funções de onda por funções de base, o hamiltoniano ZORA apresenta a configuração dada pela equação 32,

$$H^{ZORA}\phi_i{}^{ZORA} = \left(\mathbf{p}\,\frac{c^2}{2c^2 - V}\,\mathbf{p} + V_{eff}[\rho]\right)\phi_i{}^{ZORA} \tag{32}$$

Em que $p = -i\nabla$ é o operador momento e V_{eff} é o potencial escalar efetivo alto consistente (DE BOEIJ; KOOTSTRA; SNIJDERS, 2001).

2.3.3 Acoplamento spin-órbita

O acoplamento spin-órbita (SOC) tem apresentado grande importância nas propriedades espectroscópicas de metais de transição e em transições eletrônicas entre a superfície de energia potencial adiabática com o mesmo ou diferentes estados de spin (KOSEKI; SCHMIDT; GORDON, 1998; NEESE et al., 2007). O acoplamento spin-órbita aparece quando elétrons se movimentam em um campo elétrico E e um campo magnético B com o perfil determinado na equação 33 com a velocidade da Luz (*c*) produz uma energia de momento angular de Zeeman conforme a equação 34 (MANCHON et al., 2015).

$$B_{eff} \sim E \times \frac{\boldsymbol{p}}{mc^2} \tag{33}$$

$$E = \mu_B \boldsymbol{\sigma} \cdot \boldsymbol{B_{eff}} \tag{34}$$

No qual, $\mu_B = 9,27 \times 10^{-24} JT^{-1}$ é o Magneton de Bohr e $\boldsymbol{\sigma}$ é o vetor de matrizes de spin de Pauli.

O Operador Spin-Órbita de Pauli-Breit é dado pela equação 35, o qual é conhecido como primeiro e segundo operador SOC para dois elétrons.

$$\hat{H}_{SO} = \frac{\Omega^2}{2} \left\{ \sum_{i=1}^{N_{el}} \sum_{\alpha=1}^{N_{átomos}} \frac{Z_\alpha}{|\vec{r}_i - \vec{r}_j|^3} \left[(\vec{r}_i - \vec{r}_j) \times \vec{p}_i \right] \cdot \vec{S}_i - \sum_{i=1}^{N_{el}} \sum_{j \neq 1}^{N_{el}} \frac{1}{|\vec{r}_i - \vec{r}_j|^3} \left[(\vec{r}_i - \vec{r}_j) \times \vec{p}_i \right] \cdot \left[\vec{S}_i + 2\vec{S}_j \right] \right\} \tag{35}$$

Na qual Ω é a constante de estrutura fina, Z_α são as cargas nucleares, r_i e r_α são as coordenadas dos elétrons e do núcleo, respectivamente, $\vec{p}_i$ é o operador momento eletrônico e $\vec{S}_i$ é o operador de spin eletrônico (FEDOROV; GORDON, 2000).

O hamiltoniano spin-órbita pode ser aproximado para um elétron pela introdução de um termo semiempírico, a carga nuclear efetiva (Z_{eff}) (KOSEKI; SCHMIDT; GORDON, 1998). Esse termo foi previamente determinado para a sexta coluna de elementos da tabela periódica e quando empregado com funções de base do tipo ECP (effective core potential – potencial efetivo de caroço) essas cargas não explicam o efeito de campo nuclear no sentido tradicional do termo, mas são simplesmente parâmetros empíricos para compensar o negligenciamento da interação entre dois elétrons no modelo ECP orbital para o modelo spin-órbita (KOSEKI; SCHMIDT; GORDON, 1998). Essa aproximação tem sido muito bem aplicada em sistemas moleculares pequenos e para a primeira e terceira série de metais de transição (KOSEKI; SCHMIDT; GORDON, 1998). A estrutura básica do hamiltoniano spin-órbita para a aproximação de um elétron está descrita na equação 36.

$$H_{SO} \approx \frac{\alpha^2}{2} \sum_i \sum_A \frac{Z_{eff}(A)}{r^3{}_{iA}} L_{iA} S_i \tag{36}$$

Em que α^2 é a constante da estrutura fina, Z_{eff} é carga nuclear efetiva, L_{iA} é momento angular orbital e S_i é momento angular de spin.

2.4. Métodos Quimiométricos de Análise de Dados

O *design* de experimentos (DOE) é um procedimento eficiente para planejamento de experimentos no qual os dados obtidos podem ser analisados por um campo válido e apresentar conclusões objetivas. DOE começa com a determinação dos objetivos do experimento e seleção dos fatores do estudo. Um DOE é um planejamento detalhado de como fazer um experimento. O DOE pode ser empregado em diferentes tipos de problemas encontrados na pesquisa, desenvolvimento e produção (LUNDSTEDT et al., 1998).

Os modelos mais comuns são os lineares ou quadráticos. Os modelos lineares com 2 fatores, X_1 e X_2 podem ser escritos pela equação 37,

$$Y = \beta_0 + \beta_1 X_1 + \beta_2 X_2 + \beta_{12} X_1 X_2 + erro\ experimental \tag{37}$$

Em que Y é a resposta para os níveis dados para os fatores X_1 e X_2 e o termo $X_1 X_2$ contém a possibilidade de interação entre esses fatores. A constante β_0 é a resposta de Y quando os efeitos são zero. Os modelos podem apresentar maiores ordens, com 3 fatores (X_1, X_2 e X_3) ou mais, o que deixa os modelos mais complexos, porém, adicionam mais informações que influenciam a resposta Y (LUNDSTEDT et al., 1998).

O modelo de segunda ordem ou quadrático (tipicamente empregado na metodologia de superfície de resposta) não inclui interações de componentes, mas adiciona termos quadráticos ao modelo linear, como na equação 38,

$$Y = \beta_0 + \beta_1 X_1 + \beta_2 X_2 + \beta_{11} X_1{}^2 + \beta_{22} X_2{}^2 + erro\ experimental \tag{38}$$

2.4.1. Planejamento Fatorial

No planejamento fatorial as influências de todas as variáveis, fatores e interação de fatores na resposta ou respostas são investigadas. Se as combinações dos K fatores são investigadas em 2 níveis, o fatorial será designado como 2^K. Os níveis dos fatores são dados por – (menos) para o menor nível e + (mais) para o maior nível. Um nível zero é também incluído, um centro, no qual as variáveis possuem valores médios. Três ou quatro centros experimentais podem também ser incluídos no planejamento fatorial, pelas seguintes razões (CHEN et al., 2015; LUNDSTEDT et al., 1998):

   a) O risco de perder uma relação não linear no meio do intervalo de minimização;

b) Repetição para determinar o intervalo de confiança.

Os valores de – e + correspondem aos valores assumidos como uma razoável variação a ser investigada. Dessa forma o tamanho do domínio do experimento é selecionado. Para um planejamento de duas variáveis os valores de – e + são os cantos de um quadrado, para um com três variáveis são os cantos de um cubo (CHEN et al., 2015; LUNDSTEDT et al., 1998). O sinal da interação é dado pela multiplicação simples entre os valores das variáveis, dessa forma pode-se construir uma coluna de sinais representando todas as interações do planejamento fatorial.

Tabela 1 – Planejamentos Fatoriais contendo dois ou três variáveis mostrando os níveis de cada variável e das interações do conjunto de variáveis.

Duas variáveis				Três variáveis						
Exp. Nº.	Variáveis			Exp. Nº.	Variáveis						
	X_1	X_2	X_1X_2		X_1	X_2	X_3	X_1X_2	X_1X_3	X_2X_3	$X_1X_2X_3$
1	-	-	+	1	-	-	-	+	+	+	-
2	+	-	-	2	+	-	-	-	-	+	+
3	-	+	-	3	-	+	-	-	+	-	+
4	+	+	+	4	+	+	-	+	-	-	-
				5	-	-	+	+	-	-	+
				6	+	-	+	-	+	-	-
				7	-	+	+	-	-	+	-
				8	+	+	+	+	+	+	+

A tabela de sinais, ou matriz de planejamento, para 2 ou 3 variáveis está apresentada na Tabela 1. No planejamento adiciona-se o ponto central se pretende avaliar a não linearidade entre as variáveis e a resposta. Se o valor do ponto central é muito diferente da média β_0, então, é necessário incluir termos quadráticos ao modelo. Dessa maneira experimentos adicionais devem ser desenvolvidos (CHEN et al., 2015).

O efeito β_0 é a média das respostas obtidas em cada experimento, os efeitos β_1, β_2 e β_3 são calculados empregando a resolução com os sinais da matriz

de planejamento com a resposta para cada experimento. Admitindo o planejamento de três variáveis e considerando que cada experimento gere uma resposta Y_n (Y_1, Y_2, ..., Y_8) o cálculo dos efeitos é dado pelas equações 39, 40, 41 e 42 (LUNDSTEDT et al., 1998),

$$\beta_0 = \frac{Y_1+Y_2+Y_3+Y_4+Y_5+Y_6+Y_7+Y_8}{8} \tag{39}$$

$$\beta_1 = \frac{-Y_1+Y_2-Y_3+Y_4-Y_5+Y_6-Y_7+Y_8}{8} \tag{40}$$

$$\beta_2 = \frac{-Y_1-Y_2+Y_3+Y_4-Y_5-Y_6+Y_7+Y_8}{8} \tag{41}$$

$$\beta_3 = \frac{-Y_1-Y_2-Y_3-Y_4+Y_5+Y_6+Y_7+Y_8}{8} \tag{42}$$

De forma análoga se faz para as interações X_1X_2, X_1X_3, X_2X_3 e para a interação entre as três variáveis $X_1X_2X_3$. A estimativa dos efeitos são então um modelo polinomial descrevendo a relação entre as variáveis, essa função é agora descrita como a variação experimental e suas interações que influenciam a resposta Y. O modelo mostra quais variáveis apresentam alta influência no estudo e permite avaliar em qual direção as variáveis influenciam, dependendo do sinal $(-, +)$ de cada efeito β_n pode-se determinar se é o nível menor ou o maior que mais influencia a resposta Y (LUNDSTEDT et al., 1998; WILLIAMS; STAND; SCHLEYER, 1968).

Para comparar a estimativa dos efeitos, (β_n), pode-se usar o erro experimental, calculado pela repetição do experimento e determinação do s^2. Porém, essa comparação não é muito útil por causa do baixo grau de liberdade. Outro método de estudar o erro experimental é usando a distribuição normal. Esse é um método simples e rápido para indicar se a estimativa dos efeitos é

significativamente divergente a distribuição normal. Se um efeito desvia muito da distribuição normal é provável que ele descreva mais do que só o ruído experimental (CHEN et al., 2015; LUNDSTEDT et al., 1998).

A Variância Explicada, R^2, e a Variância Predita, Q^2, apresentam boas indicações de que o modelo está satisfatório. R^2 é a fração da variância total da resposta que é explicada pelo modelo, e é calculada conforme a equação 43,

$$R^2 = \frac{(SS - SS_{resid})}{SS} \tag{43}$$

SS é a soma dos quadrados da variância total da resposta selecionada, corrigido com a média. A SS total consiste de duas partes, uma parte resultado do modelo de regressão SS_{regr} e outro dos resíduos SS_{resid}. Resíduos pequenos renderam um alto grau de explicação da variância (CHEN et al., 2015; LUNDSTEDT et al., 1998). A variância predita Q2 é a fração da variância total da resposta que pode ser predita no modelo, e é calculada como na equação 44,

$$Q^2 = \frac{(SS - PRESS)}{SS} \tag{44}$$

PRESS é o resíduo predito pela soma dos quadrados e é determinado através da validação cruzada. Pequenos desvios entre o resíduo atual e o predito rendem baixo PRESS e um alto valor da variância predita.

Na análise de variância, ANOVA, o total de variação da resposta é definido como a soma de dois componentes; a componente regressão (SS_{regr}) e a componente dos resíduos (SS_{resid}) (LUNDSTEDT et al., 1998). A soma dos quadrados da variância total, corregida com a média (SS), pode ser escrita pela equação 45,

$$SS = SS_{regr} + SS_{resid} \tag{45}$$

Na ANOVA a componente regressão da variância total é comparada com o componente residual, se o desvio médio da resposta explicada no modelo é maior que o desvio médio dos resíduos multiplicado pela raiz quadrada do modelo teste F $\left(RSD * \sqrt{F}\right)$, então o modelo é significativo no nível de probabilidade usada (usualmente P=0,05%) (LUNDSTEDT et al., 1998).

2.4.2. Metodologia de Superfície de Resposta

Superfície de Resposta são usadas para determinar o ótimo, sendo uma excelente maneira gráfica de relação entre as diferentes variáveis experimentais e as respostas. Para determinar o ótimo é necessário que a função polinomial contenha termos quadráticos, conforme mostrado na equação 46 (CHEN et al., 2015; LUNDSTEDT et al., 1998).

$$y = \beta_0 + \sum_i^k \beta_i x_i + \sum_i^k \beta_{ii} x^2{}_i + \sum \sum_{i<j}^k \beta_{ij} x_i x_j + \varepsilon \qquad (46)$$

Um modelo de superfície de resposta é quando uma otimização simplex com 2 variáveis circula o valor ótimo, um hexágono é formado. Esse planejamento é chamado de Doehlert e segue o cálculo da superfície de resposta para minimizar o experimento. Outra qualidade atrativa desse planejamento é que o domínio da vizinhança é facilmente explorado pela adição de poucos pontos (CHEN et al., 2015; LUNDSTEDT et al., 1998).

Outro modelo é desenvolvido com ponto central. Este planejamento possui algumas características:

a) O fatorial completo ou fracionário.

b) Apresentam ponto central, ou seja, as variáveis apresentam valores $x_i = 0$, para todos os i.

c) Experimentos onde $x_i = \pm\alpha$ e com $x_j \neq x_i = 0$. Esse ponto são

situados nos eixos no sistema de coordenadas e com distância $\pm\alpha$ da origem; esses são pontos axiais.

O fatorial do tipo Box-Behnken segue o modelo quadrático predito pela superfície de resposta e permite avaliar em três níveis diferentes o número de variáveis que se pretende estudar (CHEN et al., 2015).

2.5. Análise das Componentes Principais (PCA)

Muitas aplicações químicas de análise de dados são de natureza multivariada e um dos métodos mais empregados é a PCA (FERREIRA, 2002). Esse é um método de compreensão de dados baseados na correlação entre as variáveis (CANTARELLI et al., 2014). O objetivo da metodologia é agrupar essas variáveis correlacionadas, substituindo os descritores originais por novos chamados de componentes principais, PCs, onde os dados são projetados (FERREIRA, 2002). Estes PCs são completamente não correlacionados e são construídos como uma combinação linear simples das variáveis originais. É importante que as variáveis contenham a maior variação do conjunto de dados. A primeira componente, PC1, é definida como a direção de maior variância do conjunto de dados, a PC2 é a direção que descreve a máxima variância no subespaço ortogonal da PC1 (CANTARELLI et al., 2014). As componentes seguintes são ortogonais às escolhas prévias e descrevem o máximo de variância restante (FERREIRA, 2002). Apenas as redundâncias é removido, apenas a primeira componente é requerida para descrever o maior número de informações contido no conjunto de dados originais (SILVA et al., 2015a). A matriz de dados X(*I*x*J*) é decomposta em duas matrizes, T e L, como na equação 47:

$$X = TL^T \tag{47}$$

A matriz T representa os eixos, a matriz L descreve as colunas dos novos

eixos, assim, as PCs são construídas com os eixos antigos.

Outra forma de resolver a PCA é usando a técnica de decomposição do valor singular, SVD, que decompõe a matriz X em três novas matrizes, U, S e V, onde U e V são auto vetores ortogonais constituídos por matrizes quadradas e S é a matriz diagonal contendo os valores singulares (equivalente ao quadrado dos autovalores). O produto U*S é a matriz T, enquanto V corresponde a matriz L. O quadrado de cada elemento diagonal é igual a variância dos dados originais descrito pela componente principal correspondente (FERREIRA, 2002; SILVA et al., 2015a).

2.6. Análise Hierárquica de Clusters (HCA)

Análise Hierárquica de Clusters é outro método multivariado importante na análise de dados (CANTARELLI et al., 2014; SILVA et al., 2015a). O propósito dessa técnica é distribuir os dados de modo a enfatizar a natureza das ramificações e padrões. Os resultados, que é de natureza qualitativa, são apresentados na forma de um Dendograma através da visualização simples no espaço 2D (FERREIRA, 2002; SILVA et al., 2015a). As distâncias entre as amostras ou variáveis são calculadas e transformadas na matriz de similaridade S, no qual os elementos são fixados similarmente. Para duas amostras quaisquer k e l, a similaridade é definida pela equação 48,

$$S_{kl} = 1.0 - \frac{d_{kl}}{d_{max}} \qquad (48)$$

Onde S_{kl} é um elemento de S, d_{max} é a maior distância para um par de amostras no conjunto de dados, d_{kl} é a distância Euclidiana entre as amostras k e l calculadas pela equação 49,

$$d_{kl} = \sqrt{(x_{k1} - x_{1l})^2 + (x_{k2} - x_{2l})^2 + \cdots + (x_{kl} - x_{kl})^2} \qquad (49)$$

Em que x_{ij} é um elemento da matriz de dados X. A similaridade muda de zero até 1. S_{kl} reflete diretamente a similaridade do conjunto de dados (FERREIRA, 2002).

3. OBJETIVOS

Os Objetivos do trabalho são: 1) Estudar computacionalmente os parâmetros cinéticos e termodinâmicos do processo ESIPT em derivados de naftoquinonas, utilizando a teoria do funcional de densidade (DFT) e a teoria do funcional de densidade dependente do tempo (TDDFT). 2) Avaliar, por métodos computacionais, os efeitos relativísticos (hamiltoniano relativístico, função de base relativística e o efeito spin-órbita) em derivados halogenados de naftoquinonas e sua influência sobre o processo ESIPT. 3) Avaliar, por métodos computacionais (DFT e TDDFT), o efeito dos substituintes sobre as energias de absorção, emissão e transferência de hidrogênio em derivados de naftoquinonas, aplicando metodologias quimiométricas para racionalização dos resultados.

Os resultados computacionais dos parâmetros termodinâmicos, cinéticos, dos efeitos relativísticos e das energias envolvidas no processo ESIPT estão relatados nos artigos 1, 2 e 3.

REFERÊNCIAS BIBLIOGRÁFICAS

ANNARAJ, B. et al. DFT study on the ground state and excited state intramolecular proton transfer of propargyl arm containing Schiff bases in solution and gas phases. **Computational and Theoretical Chemistry**, Amsterdam, NL: Elseiver Scientific Publishing, v. 1028, p. 19–26, 2014.

BELPASSI, L. et al. Recent advances and perspectives in four-component Dirac–Kohn–Sham calculations. **Physical Chemistry Chemical Physics**,

Cambridge, Inglaterra, GB: Royal Society of Chemistry, v. 13, n. 27, p. 12368–12394, 2011.

CANTARELLI, M. Á. et al. Authentication and Discrimination of Whiskies of High Commercial Value by Pattern Recognition. **Food Analytical Methods**, New York, USA: Springer, US, v. 8, n. 3, p. 790–798, 2014.

CASIDA, M. E.; HUIX-ROTLLANT, M. Progress in Time-Dependent Density-Functional Theory. **Annual Review of Physical Chemistry**, Stanford, Conn., US: Annual Reviews, v. 63, n. 1, p. 287–323, 2012.

CHARAF-EDDIN, A. et al. Choosing a functional for computing absorption and fluorescence band shapes with TD-DFT. **Journal of Chemical Theory and Computation**, Washington, DC: ACS Publications, v. 9, n. 6, p. 2749–2760, 11 jun. 2013.

CHEN, K. et al. Optimization of Process Variables in the Synthesis of Isoamyl Isovalerate Using Sulfonated Organic Heteropolyacid Salts as Catalysts. **Journal of the Brazilian Chemical Society**, São Paulo, SP: Sociedade Brasileira de Química, v. 26, n. 3, p. 600–608, 2015.

CHERMETTE, H. Density functional theory. **Coordination Chemistry Reviews**, Amsterdam, NL: Elseiver Scientific Publishing, v. 178-180, p. 699–721, 1998.

DABBAGH, H. A. et al. Theoretical study on structure, conformation, stability and electronic transition of C4 and C5 anions of ascorbic acid stereoisomers. **Journal of Molecular Structure**, Amsterdam, NL: Elseiver Scientific Publishing, v. 1061, p. 69–75, 2014.

DE BOEIJ, P. L.; KOOTSTRA, F.; SNIJDERS, J. G. Relativistic effects in the optical response of HgSe by time-dependent density functionals theory. **International Journal of Quantum Chemistry**, New York, US: John Wiley & Sons, v. 85, n. 4-5, p. 449–454, 2001.

FEDOROV, D. G.; GORDON, M. S. A study of the relative importance of one

and two-electron contributions to spin–orbit coupling. **The Journal of Chemical Physics**, New York, US: American Institute of Physics, v. 112, n. 13, p. 5611, 2000.

FERREIRA, M. M. C. Multivariate QSAR. **Journal of the Brazilian Chemical Society**, São Paulo, SP: Sociedade Brasileira de Química, v. 13, n. 6, p. 742–753, 2002.

FILATOV, M.; CREMER, D. On the physical meaning of the ZORA Hamiltonian. **Molecular Physics**, London, GB: Taylor & Francis, v. 101, n. 14, p. 2295–2302, 2003.

GORIN, D. J.; TOSTE, F. D. Relativistic effects in homogeneous gold catalysis. **Nature**, London, GB: Macmillan Journals, v. 446, n. 7134, p. 395–403, 22 mar. 2007.

GÖRLING, A. Orbital- and state-dependent functionals in density-functional theory. **The Journal of Chemical Physics**, New York, US: American Institute of Physics, v. 123, n. 6, p. 062203, 2005.

GRITSENKO, O. V.; SCHIPPER, P. R. T.; BAERENDS, E. J. Exchange and correlation energy in density functional theory: Comparison of accurate density functional theory quantities with traditional Hartree–Fock based ones and generalized gradient approximations for the molecules Li_2, N_2, F_2. **The Journal of Chemical Physics**, New York, US: American Institute of Physics, v. 107, n. 13, p. 5007, 1997.

GUAN, J. et al. Comparison of local-density and Hartree–Fock calculations of molecular polarizabilities and hyperpolarizabilities. **The Journal of Chemical Physics**, New York, US: American Institute of Physics, v. 98, n. 6, p. 4753, 1993.

HERTWIG, R. H.; KOCH, W. On the parameterization of the local correlation functional. What is Becke-3-LYP? **Chemical Physics Letters**, Amsterdam, NL: North-Holland, v. 268, n. 5-6, p. 345–351, 1997.

HONG, G.; DOLG, M.; LI, L. A comparison of scalar-relativistic ZORA and DKH density functional schemes: Monohydrides, monooxides and monofluorides of La, Lu, Ac and Lr. **Chemical Physics Letters**, Amsterdam, NL: North-Holland, v. 334, n. 4-6, p. 396–402, 2001.

ILIAŠ, M.; KELLÖ, V.; URBAN, M. Relativistic effects in atomic and molecular properties. **Acta Physica Slovaca. Reviews and Tutorials**, Bratislava, SVK, v. 60, n. 3, 1 jan. 2010.

JACQUEMIN, D. et al. TD-DFT Performance for the Visible Absorption Spectra of Organic Dyes: Conventional versus Long-Range Hybrids. **Journal of Chemical Theory and Computation**, Washington, DC: ACS Publications, v. 4, n. 1, p. 123–135, jan. 2008.

KOSEKI, S.; SCHMIDT, M. W.; GORDON, M. S. Effective Nuclear Charges for the First- through Third-Row Transition Metal Elements in Spin−Orbit Calculations. **The Journal of Physical Chemistry A**, Washington, DC, US: ACS Publications, v. 102, n. 50, p. 10430–10435, 1998.

KRISHNA, V. Time-dependent density-functional theory for nonadiabatic electronic dynamics. **Physical Review Letters**, New York, US: American Institute of Physics, v. 102, n. 5, p. 1–4, 2009.

LENTHE, E. VAN et al. Relativistic total energy using regular approximations Relativistic total energy using regular approximations. v. 9783, n. 1994, 2014.

LUNDSTEDT, T. et al. Experimental design and optimization. **Chemometrics and Intelligent Laboratory Systems**, Amsterdam, NL: Elsevier Science, v. 42, n. 1-2, p. 3–40, ago. 1998.

MANCHON, A et al. New perspectives for Rashba spin–orbit coupling. **Nature Materials**, London, GB: Nature Publishing Group, v. 14, n. 9, p. 871–882, 20 ago. 2015.

MARIAM, Y. H.; MUSIN, R. N. A B3LYP study of intramolecular hydrogen bonding and proton transfer in naphthazarin: A model system for

daunomycin/adriamycin. **Journal of Molecular Structure: THEOCHEM**, Amsterdam, NL: Elsevier Science, v. 549, n. 1-2, p. 123–136, 2001.

MOSQUERA, M. A. Action formalism of time-dependent density-functional theory. **Physical Review A - Atomic, Molecular, and Optical Physics**, New York, US: American Physical Society, v. 88, n. 2, p. 1–6, 2013.

MOSQUERA, M. A.; JENSEN, D.; WASSERMAN, A. Fragment-based time-dependent density functional theory. **Physical Review Letters**, New York, US: American Institute of Physics, v. 111, n. 2, p. 1–5, 2013.

MUSIC, D.; GEYER, R. W.; SCHNEIDER, J. M. Recent progress and new directions in density functional theory based design of hard coatings. **Surface and Coatings Technology**, Lausanne, Suica, CH: Elsevier Sequoia, v. 286, p. 178–190, jan. 2016.

NAKAJIMA, T.; HIRAO, K. The higher-order Douglas–Kroll transformation. **The Journal of Chemical Physics**, New York, US: American Institute of Physics, v. 113, n. 18, p. 7786, 2000.

NAKAJIMA, T.; SUZUMURA, T.; HIRAO, K. A new relativistic scheme in Dirac–Kohn–Sham theory. **Chemical Physics Letters**, Amsterdam, NL: North-Holland, v. 304, n. February, p. 271–277, 1999.

NEESE, F. et al. Advanced aspects of ab initio theoretical optical spectroscopy of transition metal complexes: Multiplets, spin-orbit coupling and resonance Raman intensities. **Coordination Chemistry Reviews**, Amsterdam, NL: Elsevier Scientific Publishing, v. 251, n. 3-4, p. 288–327, fev. 2007.

NEESE, F. Prediction of molecular properties and molecular spectroscopy with density functional theory: From fundamental theory to exchange-coupling. **Coordination Chemistry Reviews**, Amsterdam, NL: Elsevier Scientific Publishing, v. 253, n. 5-6, p. 526–563, 2009.

PANTAZIS, D. A. et al. All-Electron Scalar Relativistic Basis Sets for Third-Row Transition Metal Atoms. **Journal of Chemical Theory and Computation**,

Washington, DC: ACS Publications, v. 4, n. 6, p. 908–919, jun. 2008.

PYYKKÖ, P. Theoretical Chemistry of Gold. **Angewandte Chemie International Edition**, Weinheim, Alemanha, DE: Verlag Chemie, v. 43, n. 34, p. 4412–4456, 27 ago. 2004.

PYYKKÖ, P. Relativistic Effects in Chemistry: More Common Than You Thought. **Annual Review of Physical Chemistry**, Stanford, Conn., US: Annual Reviews, v. 63, n. 1, p. 45–64, jan. 2012.

REIHER, M.; WOLF, A. Exact decoupling of the Dirac Hamiltonian. I. General theory. **The Journal of chemical physics**, New York, US: American Institute of Physics, v. 121, n. 5, p. 2037–47, 1 ago. 2004.

RUGGENTHALER, M.; PENZ, M.; VAN LEEUWEN, R. Existence, uniqueness, and construction of the density-potential mapping in time-dependent density-functional theory. **Journal of Physics: Condensed Matter**, Bristol, Inglaterra, GB: Institute of Physic, v. 27, n. 20, p. 203202, 2015.

SADLEJ, A. J. Improving upon the ZORA Hamiltonian. **International Journal of Quantum Chemistry**, New York, US: John Wiley & Sons, v. 106, n. 12, p. 2518–2524, 27 ago. 2006.

SAN-MIGUEL, M. A. et al. In situ growth of Ag nanoparticles on α -Ag 2 WO 4 under electron irradiation: probing the physical principles. **Nanotechnology**, Bristol, Inglaterra, GB: IOP Publishing, v. 27, n. 22, p. 225703, 3 jun. 2016.

SHIOZAKI, T.; MIZUKAMI, W. Relativistic Internally Contracted Multireference Electron Correlation Methods. **Journal of Chemical Theory and Computation**, Washington, DC: ACS Publications, v. 11, n. 10, p. 4733-4739, 14 set. 2015.

SILVA, F. L. DO N. et al. Quantitation of organic acids in wine and grapes by direct infusion electrospray ionization mass spectrometry. **Analytical Methods**, Cambridge, Inglaterra, GB: Royal Society of Chemistry, v. 7, n. 1, p. 53–62, 2015.

TSIPIS, A. C. DFT flavor of coordination chemistry. **Coordination Chemistry Reviews**, Amsterdam, NL: Elseiver Scientific Publishing, v. 272, p. 1–29, 2014.

VAARA, J.; PYYKKÖ, P. Relativistic, nearly basis-set-limit nuclear magnetic shielding constants of the rare gases He-Rn: A way to absolute nuclear magnetic resonance shielding scales. **Journal of Chemical Physics**, New York, US: American Institute of Physics, v. 118, n. 7, p. 2973–2976, 2003.

VAN LENTHE, E.; SNIJDERS, J. G.; BAERENDS, E. J. The zero-order regular approximation for relativistic effects: The effect of spin–orbit coupling in closed shell molecules. **The Journal of Chemical Physics**, New York, US: American Institute of Physics, v. 105, n. 15, p. 6505–6516, 1996.

WILLIAMS, J. E.; STAND, P. J.; SCHLEYER, P. R. Physical Organic Chemistry: Quantitative Conformational Analysis; Calculation Methods. **Annual Review of Physical Chemistry**, Stanford, Conn., US: Annual Reviews, v. 19, n. 1, p. 531–558, out. 1968.

WOLF, A.; REIHER, M. Exact decoupling of the Dirac Hamiltonian. III. Molecular properties. **Journal of Chemical Physics**, New York, US: American Institute of Physics, v. 124, n. 6, 2006.

WOLF, A.; REIHER, M.; HESS, B. A. The generalized Douglas-Kroll transformation. **Journal of Chemical Physics**, New York, US: American Institute of Physics, v. 117, n. 20, p. 9215–9226, 2002.

YANAI, T.; TEW, D. P.; HANDY, N. C. A new hybrid exchange-correlation functional using the Coulomb-attenuating method (CAM-B3LYP). **Chemical Physics Letters**, Amsterdam, NL: North-Holland, v. 393, n. 1-3, p. 51–57, 2004.

SEGUNDA PARTE – ARTIGOS

ARTIGO 2 PROBING THE ESIPT PROCESS IN 2-AMINO-1,4-NAPHTHOQUINONE: THERMODYNAMICS PROPERTIES, SOLVENT EFFECT AND CHEMOMETRIC ANALYSIS

Probing the ESIPT process in 2-amino-1,4-naphthoquinone: thermodynamics properties, solvent effect and chemometric analysis

Abstract

The developing of fluorescent probes for disease diagnosis is a very important task, which favors precision in the diagnosis and success in the treatment. Recently, amino-naphthoquinone derivatives showed to be efficient fluorescent probes for disease diagnosis. Those compounds exhibit excited-state intramolecular proton transfer (ESIPT), which is the main mechanism responsible for their use as fluorescent probes. The understanding of the ESIPT mechanism for naphthoquinones is an important way of developing more efficient and selective fluorescent probes. In this work, the ESIPT process for ANQ was performed at the TD-DFT/CAM-B3LYP/DGTZVP and DFT/B3LYP/DGTZVP level for the electronic and geometric studies. These parameters were selected for the PCA analysis. The solvent effect was investigated by using PCM and IEF-PCM in chloroform, water and methanol. 2-Amino-1,4-naphthoquinone (ANQ) showed blue emission for fluorescence, having keto–keto* absorption at 4.50 eV and the enol–enol* decay at 2.75 eV. The solvent effect was evaluated, and the ESIPT process of ANQ was favorable in nonpolar and polar solvents. Furthermore, the thermodynamics properties showed that the ESIPT is favorable with a proton transfer equilibrium constant of $\sim 10^5$.

1 Introduction

Despite recent technological advances, cancer is still one of the most serious problems of humanity [1–3]. This outlook is aggravated due to difficulty of preoperative and postoperative diagnoses. In this line, one of the greatest challenges of diagnostic imaging is to develop a system able to locate species in different environments with high resolution for detecting focus of cancer in

surgical margins for clinical use [1, 4]. However, due to sensitivity and easy operation analysis in live systems, the interest in fluorescence probes and their application to the detection of tumors by spectroscopic techniques has increased [5–7].

Recently, amino-naphthoquinone derivatives, such as 2-amino-1,4-naphthoquinone (ANQ keto), have been used with success as fluorescent probes. Laurieri et al. showed that ANQ keto interacts with arylamine *N*-acetyltranspherase 1 (NAT1) enzyme, [1, 8], which was used for in vivo and in vitro detection of breast cancer. The authors related a color change in the compounds tested when they interact with the target enzyme [1, 5, 9].

It is well known that the fluorescence process can be modulated by different mechanisms, such as intramolecular charge transfer (ICT), excited-state proton transfer (ESPT) and excited-state intramolecular proton transfer (ESIPT) [10, 11]. So far, the fluorescence mechanism in ANQ has not been totally defined in the literature. Some previous studies suggest an amine group deprotonation, but there has been no further investigation into whether the proton transfer comes from an intramolecular chemical reaction or whether it is a chemical reaction between solvent and the amino group of the substrate [12, 13]. The ESIPT process can be one mechanism for the fluorescence process, and despite its great importance, there is no theoretical study reported for the ANQ derivatives. It is also important to keep in mind that the ESIPT process has attracted special attention due to very large fluorescence emission, allowing compounds that exhibit it to be used as spectroscopic probes in biological organisms [10]. Therefore, the investigation and understanding of the ESIPT mechanism in ANQ are important ways of developing more efficient and selective fluorescent probes [12–14].

The ESIPT process occurs when the keto form in the excited state is converted to an enol form through the fluorescence emission [15, 16]. During the

ESIPT process, a proton on the amino group of ANQ migrates to the neighboring carboxyl group to give the ANQ-enol form [5].

In fact, the understanding of the ESIPT mechanism has an important impact on the development of fluorescent probes. In spite of its great importance, only a few theoretical studies involving the ESIPT process with 2-amino-1,4-naphthoquinone have been reported in the literature [10, 12, 13, 17, 18]. It is important to mention that ANQ derivatives reveal promising applications as fluorescence probes, as well as in anti-tumor, anti-leishmania, anti-bacterial, anti-inflammatory, anti-HIV and anti-Chagas activity [10, 12, 13, 17–19].

Previous theoretical studies for the ESIPT process have been carried out by using the time-dependent density functional theory (TD-DFT) [20]. This methodology is used to evaluate electronic properties and dynamics of manybody systems in the presence of time-dependent potentials, which is an extension of the formal foundation of DFT [20]. In fact, recent findings support the good agreement between TD-DFT and some multi-reference methods, such as CASSCF, for excited-state calculations [21].

A great concern with DFT is that the exact functional for exchange and correlation is not known except for the free electron gas [21]. However, some approximations exist and accurately permit the calculations of several physical properties. Currently, DFT functionals are classified into some groups, for instance the global hybrid functional (B3LYP, B3PW91 and mPW1PW91) [21] and long-range corrected hybrid functional (CAM-B3LYP and ωb97X-D) and GGA family (PBE), for the TD-DFT study of the ESIPT process [21–23]. Each one has its advantages and drawbacks, and careful validation is necessary in order to identify a particular functional (or a combination thereof) that affords reliable results.

In this context, the use of chemometric methods can significantly assist in the choice of the best density functional to describe the spectroscopic properties

of compounds in solution, such as naphthoquinone derivatives [24, 25]. In this context, Barboza et al. employed principal component analysis (PCA) and hierarchical component analysis (HCA) for identifying similarities among different families of functionals for analysis of spectroscopic properties employed in TD-DFT study [23, 26–29].

Despite its great importance, surprisingly little detailed computational work on fluorescent probes based on naphthoquinone derivatives has appeared. For instance, in 2010, Jacquemin et al. studied the absorption and fluorescence parameters of hydroxy-naphthoquinone as well as the ESIPT process [23, 28, 30]. In 2013, Boo et al. [29] studied the ESIPT process for 5,8-dihydroxy-1,4-naphthoquinone. They evaluated the absorption and fluorescence processes via TD-DFT calculations, employing the B3LYP functional and cc-pVTZ basis set [29].

It is also important to keep in mind that the conformational analysis plays a crucial role in the ESIPT process, because changes in the dihedral angle of the compounds have great impact on the fluorescence emission [31, 32].

During the formation of keto–enol forms, the changes in the compound structure revealed new dihedral angles, and analysis of these modifications can generate high computational cost [31, 33, 34]. For the minimization of this cost, the use of surface response, in which the potential energy surface is investigated, employed the minimum number of structures necessary for the analysis of the global surface [35–37].

The goal of the present work is to study the ESIPT process of 2-amino-1,4-naphthoquinone by using TD-DFT and chemometric analysis in order to evaluate the solvent and the thermodynamics parameters, as well as to identify the best DFT functional for electronic and structural calculations by using chemometric calculations [24]. Thus, the work is divided into four parts. In the first, we have discussed the most appropriate exchange and correlation functional

to obtain absorption values of ANQ keto and enol forms. In the second part, we have selected the best DFT geometry by chemometric analysis. In the third, we perform a conformational search of the ANQ keto and enol forms and also apply the DFT and TD-DFT functionals previously selected for the reaction mechanism of the ESIPT process. Finally, in the fourth part, by using the previous results, the solvent effects on thermodynamics parameters for the ESIPT process were obtained.

2 Computational details

For the ground state, the compounds were optimized with the DGTZVP basis set by two theoretical methods, second-order Møller–Plesset perturbation theory (MP2) [38–41] and density functional theory (DFT) with B3LYP, B3PW91, mPW1PW91, PBE, ωB97X-D and CAMB3LYP. The MP2 geometry was used as reference, because MP2 geometries are in a good agreement with experimental values of X-ray [39, 40, 42]. Furthermore, a force constant calculation was made to verify whether the optimized structures were indeed local minima (no imaginary frequencies) or transition states (one imaginary frequency) [43]. From the ground state geometry, ANQ structures, enol and keto forms, were optimized in the excited state and electronic parameters, such as absorption, fluorescence wavelength and oscillator force, were calculated at the TDDFT level. In this stage, the functional B3LYP, B3PW91, mPW1PW91, PBEPBE, CAM-B3LYP and ωB97X-D were employed for electronic structure calculations (The oscillator strength and wavelength and energy values were reported in Table S1.B in Supplementary Material) [22, 42, 44]. The absorption energy and the wavelength were compared to the experimental values. The error values (See in Supplementary Material Table S5.F) were applied to PCA analysis for determining the adequate functional for the electronic property calculations. In addition, the potential energy surface along the dihedral angles angle C–C–O–H

and C–C–N–H (Fig. 1b) of ANQ in ground and excited states, as well as in solution and gas phase, was evaluated by chemometric techniques based on response surface calculations [34] (for more information about potential energy curves, see Fig. S1 in Supplementary Material).
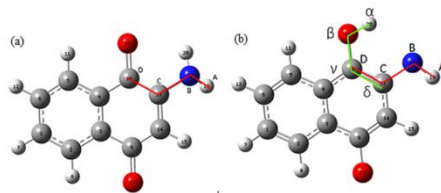
Fig. 1 a Structure for the keto form of the ANQ and the dihedral angle (in *red dihedral angle ABCD*) employed to build the potential energy surface, **b** structure for the enol form of the ANQ and the two dihedral angles (in *green αβγδ* and in *red ABCD*) used for the surface response.

For the reaction mechanism of the ESIPT process, the thermodynamics properties were computed at the DFT and TD-DFT levels employing B3LYP/DGTZVP and CAMB3LYP/DGTZPVP for ground and excited states, respectively. All the transition states, intermediates and precursors involved were calculated and characterized. The solvent effects were evaluated by using the polarization continuum model (PCM) and integral equation formalism polarization continuum model (IEF-PCM) [45–47] for methanol, water and chloroform. All electronic structure calculations were carried out with Gaussian program and visualized in the GaussView program [48, 49], while chemometrics techniques, such as PCA, HCA and response surface calculations, were performed in Statistica software [27, 35, 50].

3 Results and discussion

3.1 Chemometric analysis for the selection of the best DFT method for geometry

It should be kept in mind that the reaction mechanism for the ESIPT process should be completely studied at the same theoretical level, in other words, at the DFT level. Although having an appropriate density functional for the optimization structure in ground state is important, MP2 geometries are in a better agreement with experimental values of X-ray for some naphthoquinone derivatives in ground state [38–41]. Thus, the MP2 geometries are considered as reference for the optimization step in ground state.

The ANQ geometry for the enol and keto forms was optimized at the DFT level employing six DFT functionals, one of the GGA families (PBE), three others of the global hybrid family (B3LYP, B3PW91 and mPW1PW91) and, finally, two functionals of the long-range corrected hybrid functional (CAM-B3LYP and ωB97X-D) following the classification according to Miranda et al. [22, 51–53]. The electronic effects were also evaluated for the reference geometry of ANQ structures in ground state by using the MP2 calculations. Afterward, the excited state was calculated at the TD-DFT level with CAM-B3LYP/DGTZVP functional to obtain the absorption wavelength. That was the best theoretical methodology obtained in the previous section. Then, the error between theoretical and experimental wavelength values was calculated. The solvent effects were taken into account by IEF-PCM and PCM.

Table 1 Eigenvalues and percentage of variance for each component for the PCA.

Factor	Eigenvalues	% Total Variance	Accumulated Eigenvalues	% Accumulated
1	7.94	99.21	7.94	99.21
2	0.05	0.73	7.99	99.93
3	0.00	0.04	7.99	99.98
4	0.00	0.01	7.99	99.99

Table 2 Theoretical wavelength values calculated for the four wavelengths of the ANQ and the relative error for the six TD-DFT functional and the two solvents tested.

Optimization Method	Solvatation Method	Solvent	Wave-length	B3LYP	CAM-B3LYP	B3PW91	MPW1PW91	PBEPBE	ωB97XD
MP2	IEF-PCM	Methanol	λ_1	465.11 (-5.89)	408.13 (-62.87)	463.37 (-7.63)	447.78 (-23.22)	535.53 (64.53)	410.37 (-60.63)
			λ_2	344.38 (10.88)	302.91 (-30.59)	341.55 (8.05)	331.65 (-1.85)	385.49 (51.99)	302.06 (-31.44)
			λ_3	308.89 (24.89)	274.25 (-9.75)	307.08 (23.08)	298.52 (14.52)	346.24 (62.24)	273.5 (-10.5)
			λ_4	304.28 (25.28)	273.18 (-5.82)	304.46 (25.46)	296.75 (17.75)	330.16 (51.16)	268.82 (-10.18)
		Chloroform	λ_1	460.59 (46.59)	404.61 (-9.39)	458.91 (44.91)	443.56 (29.56)	529.8 (115.8)	406.93 (-7.07)
			λ_2	344.59 (9.35)	302.75 (-32.25)	341.6 (6.6)	331.11 (-3.53)	386 (51)	301.95 (-33.05)
			λ_3	308.31 (21.31)	274.31 (-12.69)	306.53 (19.53)	298.11 (11.11)	345.23 (58.23)	273.61 (-13.39)
			λ_4	303.48 (47.48)	272.43 (16.43)	303.42 (47.42)	295.35 (39.35)	335.32 (79.32)	268.25 (12.25)
	I-PCM	Methanol	λ_1	544.09 (73.09)	469.44 (-1.56)	547.76 (76.76)	526.62 (55.62)	642.94 (171.94)	478.09 (7.09)
			λ_2	335.63 (2.13)	298.5 (-35)	332.35 (-1.15)	323.56 (-9.94)	371.57 (38.39)	296.88 (-36.62)
			λ_3	309.92 (25.92)	273.21 (-10.79)	308.78 (24.78)	299.04 (15.04)	357.57 (73.57)	272.17 (-11.83)
			λ_4	287.66 (8.66)	245.47 (-33.53)	287.51 (8.51)	278.43 (-0.57)	353.39 (74.39)	243.86 (-35.14)
		Chloroform	λ_1	520.53 (106.53)	444.96 (30.96)	523.6 (109.6)	501.81 (87.81)	619.74 (205.74)	453.37 (39.37)
			λ_2	330.11 (-4.89)	293.96 (-41.04)	326.96 (-8.04)	318.38 (-8.04)	366.39 (31.39)	292.4 (-42.6)
			λ_3	305.7 (18.7)	269.07 (-17.93)	304.54 (17.54)	294.67 (7.67)	355.07 (68.07)	268.07 (-18.93)
			λ_4	285.15 (29.15)	241.8 (-14.2)	284.89 (28.89)	275.42 (19.42)	350.26 (94.26)	240.39 (-15.61)

		Solvent	λ_1	λ_2	λ_3	λ_4			
Experimental Value		*Methanol [30]*	*471*	*333.5*	*284*	*279*			
		Chloroform [22]	*414*	*335*	*274*	*256*			

*Wavelength values in nm; **Values in parenthesis refer a difference between calculated and experimental wavelength.

To evaluate the best functional for the optimization structure, PCA and HCA calculations were evoked. Initially, HCA also showed three groups. The groups were formed for the global hybrid functional (B3LYP, B3PW91,

mPW1PW91), GGA functional (PBE) and long-range hybrid functional (CAM-B3LYP, ωb97X-D). It is worth mentioning that ωb97X-D incorporates dispersive interactions, whose standard DFT functionals lack in the description of noncovalent interactions. For more information about PCA, see Supplementary Material in Table S4.

The PCA revealed four components with an explanation of 99.99 % of the total variance, component one being 99.21 % of accumulated explanation and component two, 0.72 % of explanation, as given in Table 1. The analysis of the two components showed a distribution of the functional into three groups and as in the previous section, Fig. 2a displays the hierarchical cluster analysis. This analysis revealed that in the long-range corrected hybrid functional, CAM-B3LYP functional showed less significance for the error when compared to ωB97X-D. It is also important to notice that B3LYP showed to be the best functional for the structure optimization. The order and distribution of the other functionals are shown in Fig. 2b.
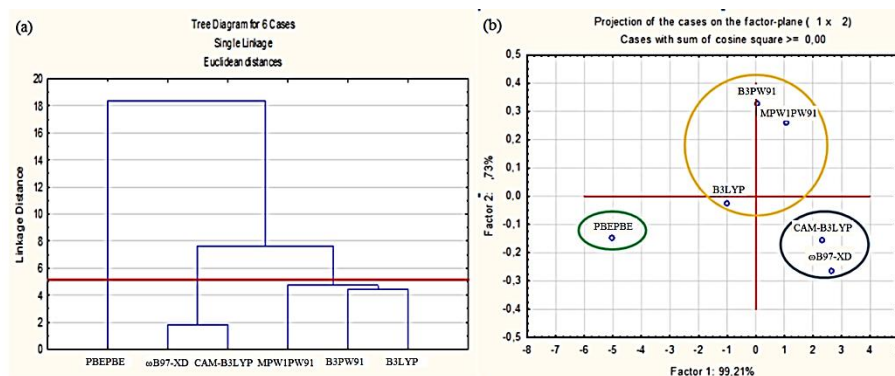
Fig. 2 a Hierarchical clustering of the distances for the DFT functionals, **b** diagram of Factor 1 and Factor 2 for scores factors.

The PCA method employed in this study can evaluate the best functional for the electronic and geometric properties. The study of the more stable

conformation for the keto–enol form of the ANQ was carried out by using B3LYP and CAM-B3LYP in ground and excited states, respectively. The current findings are supported by previous results [43, 51, 52, 54, 55].

3.2 Selection of the best TD-DFT method for absorption calculations

The selection of the best functional for the electronic properties was performed with the same six DFT functionals employed previously, PBE, B3LYP, B3PW91, mPW1PW91, CAM-B3LYP and ωB97X-D according to Yanai et al. and Kobayashi et al. [51–53]. The electronic effects were firstly evaluated for the reference geometry of ANQ structures in ground state by using B3LYP and MP2 calculations. The absorption and emission results were carried out at MP2 and B3LYP levels, and both geometric results were used for electronic properties calculations. Bearing in mind the high similarity of the obtained values, we have reported just the absorption results employing B3LYP geometries. Afterward, the absorption values were calculated for all functionals tested. The IEF-PCM and PCM were employed for reproducing the solvent effects in each case.

From the experimental data, ANQ exhibits two absorption regions in the UV–VIS spectra relative to benzenoid electron transfer bands [43, 52], which did not affect the amino group in the 256 and 335 nm regions. This absorption in chloroform and methanol is 279 and 333 nm, respectively. Also, ANQ exhibits two other bands in relation to quinoid electron transfer bands [43], which have great influence from the amino group. Those transitions occur in the regions of 287 and 414 nm, while in chloroform and methanol they occur at 284 and 471 nm, respectively [43,52]. The absorption values in water were not found in the literature and for this reason were not employed in the discussion.

The triplets and singlet states of the molecule were calculated in the TD-DFT model. It should be kept in mind that triplet states were neglected during in

the analysis, because they showed oscillator force equal to zero. However, the singlet states showed four signals with oscillator force different from zero.

The solvent effect was evaluated by IEF-PCM and PCM. By using the IEF-PCM in methanol with the B3LYP functional, the smallest error in relation to the experimental wavelength of 471 nm was obtained [17, 18]. The B3PW91 functional offers the second best result, followed by mPW1PW91, ωB97X-D and CAM-B3LYP. In the PCM method, the functional CAM-B3LYP showed smallest error for the 471 nm wavelength, followed by ωB97X-D, mPW1PW91, B3LYP and B3PW91.

In chloroform, the functional analysis showed the same trend obtained in methanol. Regarding the PCM and IEFPCM, the CAM-B3LYP functional showed the smallest error. The PCM generated larger relative errors as compared to IEF-PCM.

Since the study of error in the wavelength showed wide variation, the PCA analysis was employed for understanding how the DFT method influences the error between theoretical and experimental findings. Thus, the PCA can assist in the interpretation of the best functional for the electronic properties calculations (Table 2).

Table 3 Eigenvalues and percentage of explained variance of each component for the PCA.

Factor	Eigenvalues	% Total Variance	Accumulated Eigenvalues	% Accumulated
1	15.95	99.68	15.95	99.68
2	0.04	0.26	15.99	99.93
3	0.00	0.04	15.99	99.97
4	0.00	0.02	15.99	99.99

The multivariate analysis was performed on both methanol and chloroform with all error values found in the parameters. The HCA approach, based on the Euclidian distance, revealed three groups separated according to the

functional family, see Fig. 3a (for more information about HCA, see Table S4 in Supplementary Material). The first group is formed by the PBE functional, while the second group is formed by CAM-B3LYP and ωB97X-D functional and the third highlighted the functionals mPW1PW91, B3LYP and B3PW91.

The PCA showed four components with explanation of 99.996 % of the variability, which provides a good rationalization and separation of the DFT functional, see Table 3. This analysis showed that the first component explains 99.676 % of all variance of the collected data and the second component explains just 0.256 % of the variability. Figure 3b shows the same three groups shown in Fig. 3a. Thus, the PCA was developed for each functional family; the first is for GGA, the second and third groups for longrange corrected hybrid functional and global hybrid functional, respectively.

Within groups, the LDA/GGA functional PBE showed more to the left and exhibit more significance for Factors 1 and 2. In the second group, ωB97X-D exhibited large distance from the center relative to the two factors; however, CAM-B3LYP showed distance only from Factor 2. The ωB97X-D exhibits more significance for the error in the wavelength represented in Factor 1. The hybrid functional family that forms the third group exhibits a central position in relation to the two components. The mPW1PW91 functional is less significant for the error in relation to experimental values; however, B3LYP is more significant. The B3PW91 functional showed intermediate significance by the experiment.

The CAM-B3LYP functional was selected for theoretical calculations in the excited states. The studies for the best functional generated the best geometry for the keto and enol forms for ANQ involving applied DFT/DGTZVP methodology with the functional cited in the methodology, and after that, the excited state was investigated with TDDFT/CAM-B3LYP/DGTZVP for the error calculation in terms of absorption values.
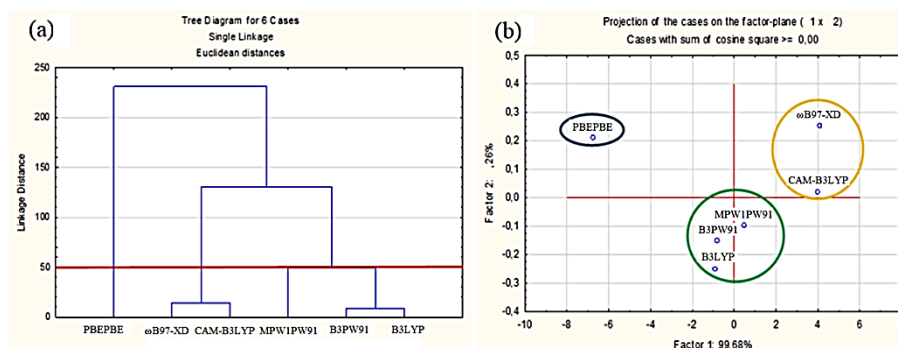
Fig. 3 a Hierarchical clustering dendrogram for DFT functionals in terms of electronic parameters, **b** diagram of Factor 1 and Factor 2 for scores factors

3.3 Potential energy surface and reaction mechanism for the ESIPT process

It is worth mentioning that the ESIPT process takes place for the proton transfer from the amino group to the carbonyl group, which can produce the tautomer, i.e., enol form. However, in order to investigate the reaction mechanism of the ESIPT process, it is important to ensure that the reaction pathway comes from the global minimum reactant structures and reaction intermediates in solution. In this line with that, to determine the global minimal the potential energy surface for the enol structure of ANQ, we have employed a chemometric method, named chemometric response surface [34]. This method is able to evaluate the variation in the two or more variables at the same time [34]. In the surface analysis, the dihedral angles 1 (C–C–O–H) and 2 (C–C–N–H) were used as variables, Fig. 1. The potential energy surface, shown in Fig. 4a, was employed in the ground state with DFT/B3LYP/DGTZVP in gas phase. The PES in solution showed some minimum energy (see Supplementary Material).

From our PES calculations, the most stable structure is formed by dihedral angles 1 and 2 of 180° and 0°, respectively. These angles were selected in the response surface calculation, see Fig. 4a. Thus, this conformation was employed for the absorption and fluorescence calculation in the enol form in the ESIPT process.
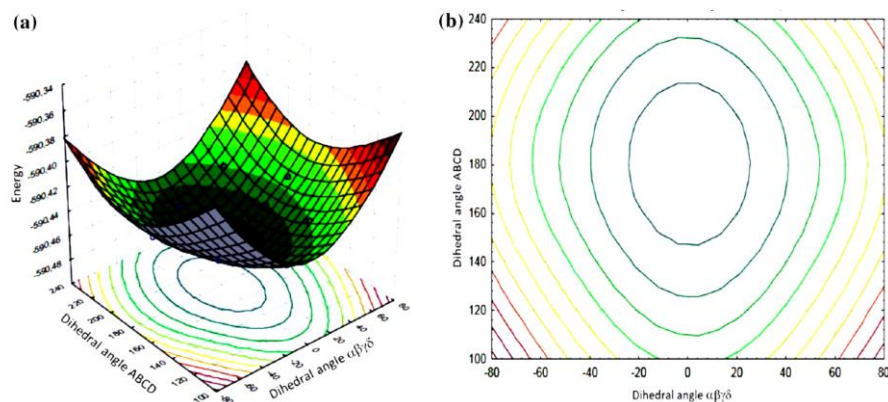
Fig. 4 a Potential energy surface for the enol form of ANQ, **b** graph of contours for the potential energy surface in gas phase for the enol form of ANQ.

This methodology was employed to allow a robust analysis of the potential energy surface along the dihedral angles C–C–O–H and C–C–N–H (Fig. 1b) of ANQ. The selected conformations from the potential energy surface calculations were optimized with DFT/TD-DFT methodologies and used as the initial point for the reaction mechanism in ground and excited states.

The ESIPT process study, shown in Fig. 5, for ANQ was carried out from the DFT selected geometries of the enol form in ground and excited states in the response surface analysis. Bearing in mind that the first step of the ESIPT mechanism is the energy absorption for keto form of ANQ (Fig. 5), the TD-DFT method was employed to compute six absorption bands. However, only four of the six bands showed oscillator force different from zero, coincident with the four experimental absorption bands [43]. The energy value for the first excited state in gas phase was 3.23 eV corresponding to 383.79 nm (violet color) from the UV–VIS results. The maximum absorption value was 4.35 eV, which represents the first step of the process, corresponding to excited state transfer to the keto compounds at 284.43 nm (ultraviolet region).
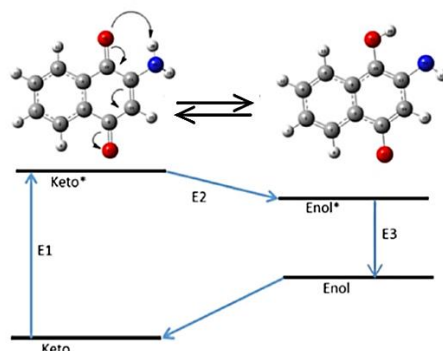
Fig. 5 Reaction mechanism for the ESIPT process, exhibiting keto to keto* absorption energy (ΔE_1) and enol to enol* emission energy (ΔE_3).

The second step was to determine the energy value of the proton transfer from the keto* to enol* form (Fig. 5). In the excited state, this transfer occurs from the amino group to the carbonyl group. The process showed an energy barrier of 0.51 eV for the proton transfer. The third step involves the emission energy between enol* and enol forms. The energy difference from enol* to the enol was 2.79 eV, which corresponds to a fluorescence emission in the region of the spectra of 445.18 nm, emitting blue color. Afterward, the enol form in the ground state is converted to keto form, emitting 1.07 eV of energy. Figure 5 shows the ESIPT process mechanism.

Table 4 Energy values (eV) associated to transition between keto–enol in the solvents tested.

Solvent	ΔE_1[a]	ΔE_2	ΔE_3	ΔE_4
Chloroform	5.74	-1.98 [b]	2.67	-1.08
Gas Phase	4.35	-0.50	2.78	-1.06
Methanol	4.53	-0.77	2.70	-1.06
Water	4.50	-0.75	2.68	-1.06

[a] See Fig. 5 [b] The negative values indicate the initial energy level is more energetic in relation to other levels.

Theoretical calculations suggest a small energy barrier between keto* and enol* in the excited states. Certainly, this energy barrier can be influenced by

solvent effects as well as modification in the ANQ structure. Actually, the solvent effect can favor or hinder the transfer process and the application of the compounds as fluorescent probes.

3.4 Solvent effects and thermodynamics properties for the ESIPT process mechanism

The solvent effects were taken into account by using the IEF-PCM for the water and methanol, polar solvents, and chloroform, nonpolar solvent. The methodology employed was similar to that previously employed in the gas phase calculations; the energy values are given in Table 4.

On going from the ground state transition to the excited state in keto form, the absorption energy (ΔE_1) is higher in the gas phase and is 4.53 eV for the methanol and 4.50 eV for water, although in chloroform, the energy was 5.74 eV. The proton transfer energy (ΔE_2) between keto and enol in the excited state is higher in solution than in the gas phase. The ΔE_2 observed was 0.77, 0.75 and 1.98 eV for methanol, water and chloroform, respectively. The noncompetition for the proton by the solvent chloroform could, in principle, explain the higher energy barrier, which indicated that the enol form is more stable in the nonpolar solvent.

$$K^* \underset{}{\overset{k^*}{\rightleftharpoons}} E^*$$

$$K \underset{}{\overset{k}{\rightleftharpoons}} E$$
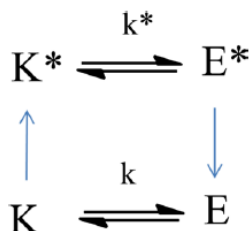
Fig. 6 Thermodynamics cycle of keto (*K*) and enol (*E*) form excitation during proton transfer. From the thermodynamic cycle in this figure, the equilibrium constant was calculated through Eqs. 1 and 2 in the ground and excited state [36].

The ANQ-enol form emitted fluorescence in a longer wavelength than in gas phase, being 462, 458 and 463 nm in water, methanol and chloroform,

respectively. All emission fluorescence was blue. The Gibbs free energy was calculated for the keto–enol form in ground state. Turning now to the excited state, the Gibbs free energy was calculated employing a similar theoretical strategy reported previously by Jacquemin et al. [28, 56, 57]. In line with that, a thermodynamics cycle is shown in Fig. 6 for the equilibrium constant (K) calculation in the ground and excited states.

$$\Delta G^0 = -RT \ln K \tag{1}$$

$$pK = \frac{\Delta G^0}{RT \ln 10} \tag{2}$$

The excited-state equilibrium constant was calculated adding the variation between the keto form absorption energy (ΔE_1) and the enol form emission energy (ΔE_3), since the proton transfer in excited state is very rapid and the equilibrium not is completed [28, 56, 57]. The Franck–Condon principle was employed, and the compounds geometry is equal in the ground state. Thus, the theoretical K calculation in the excited states was performed with the incorporation of the term ΔE, which is the difference between the keto form transition energy and the enol form transition energy. In this perspective, the excited-state equilibrium constant calculated is according to Eq. 3 [57].

$$pK^* = pK + \frac{\Delta E}{RT \ln 10} \tag{3}$$

The equilibrium constant values are given in Table 5. The proton transfer in ground state showed to be unfavorable. The K value is on the order of $\sim 10^{-8}$; this means that the keto form has more concentration than enol form in the thermodynamic equilibrium. Our theoretical findings, then, put in evidence that the proton transfer is not able to occur in these conditions. On the other hand, in excited states, the K* value is higher, on the order of 10^5, and the enol form is

favorable in relation to the keto form; therefore, the proton transfer process can occur.

Table 5 Constant values in the ground state (K) and excited state (K^*), and their respective pK and pK^* values for the proton transfer in ANQ.

Solvent	pK[a]	pK*	K	K*
Chloroform	17.70	-34.42	2.04×10^{-8}	8.91×10^{14}
Gas Phase	18.35	-8.41	1.07×10^{-8}	4.50×10^{3}
Methanol	17.48	-13.73	2.56×10^{-8}	9.14×10^{5}
Water	17.46	-13.50	2.60×10^{-8}	7.26×10^{5}

[a] Calculated values at 295 K and 1 atm.

The constant value also revealed that the nonpolar solvent was more favorable for the proton transfer in the excited state, 8.91×10^{14}, 9.14×10^{5} and 7.26×10^{5} in chloroform, methanol and water, respectively. In polar solvents, the proton transfer is favorable; however, a competition mechanism between solvent and substrate can occur.

4 Conclusions

From the theoretical data, the TD-DFT calculations were satisfactory for ANQ, the CAM-B3LYP functional exhibited better absorption and fluorescence properties results. However, for the optimization step, the B3LYP/DGTZVP functional was the best theoretical method. Furthermore, chemometric models based on the PCA analysis was satisfactory for selection of the best functional for the optimization step as well as spectroscopic properties. The solvent effect was better modeled by the IEF-PCM method. In fact, the IEF-PCM was employed in the calculations for the ESIPT process and thermodynamics properties. The ESIPT process showed blue emission in solution; chloroform was the most favorable solvent for the ESIPT process, revealing an equilibrium constant of 8.91

$\times\ 10^{14}$. The polar solvents were favorable to the process, having constant values of 9.14×10^5 in methanol and 7.26×10^5 in water. Our current findings showed that the ESIPT process was thermodynamically as well as kinetically favorable in all solvents tested and it is the most probable mechanism for the fluorescent process involving 2-amino-naphthoquinone. From our findings, ANQ reveals versatility in different solvents and potential fluorescent probe application. To our knowledge, this is the first application of this methodology to amino-naphthoquinone derivatives in the condensed phase. We strongly feel that this study could be helpful for the design and selection of fluorescent probes.

References

1. Egleton JE, Thinnes CC, Seden PT et al (2014) Structure-activity relationships and colorimetric properties of specific probes for the putative cancer biomarker human arylamine N-acetyltransferase 1. Bioorganic Med Chem 22:3030–3054. doi:10.1016/j.bmc.2014.03.015

2. Cheng L, Stopkowicz S, Gauss J (2014) Analytic energy derivatives in relativistic quantum chemistry. Int J Quantum Chem 114:1108–1127. doi:10.1002/qua.24636

3. Chaudhuri S, Pahari B, Sengupta PK (2009) Ground and excited state proton transfer and antioxidant activity of 7-hydroxyflavone in model membranes: absorption and fluorescence spectroscopic studies. Biophys Chem 139:29–36. doi:10.1016/j.bpc.2008.09.018

4. Li D, Cheng L, Jin B (2014) Investigation on PCET–accompanied dimerization of 5–hydroxy–1, 4–naphthoquinone in the process of electrochemical reduction by in situ FT–IR spectroelectrochemistry and density functional calculation. Electrochim Acta 130:387–396. doi:10.1016/j.electacta.2014.03.049

5. Laurieri N, Egleton JE, Varney A et al (2013) A novel color change mechanism for breast cancer biomarker detection: naphthoquinones as specific ligands of human arylamine N-acetyltransferase 1. PLoS ONE. doi:10.1371/journal.pone.0070600

6. Zhu B, Kan H, Liu J et al (2014) A highly selective ratiometric visual and red-emitting fluorescent dual-channel probe for imaging fluoride anions in living cells. Biosens Bioelectron 52:298–303. doi:10.1016/j.bios.2013.09.010

7. Beleites C, Steiner G, Sowa MG et al (2005) Classification of human gliomas by infrared imaging spectroscopy and chemometric image processing. Vib Spectrosc 38:143–149. doi:10.1016/j.vibspec.2005.02.020

8. Wu J, Liu W, Ge J et al (2011) New sensing mechanisms for design of fluorescent chemosensors emerging in recent years. Chem Soc Rev 40:3483–3495. doi:10.1039/c0cs00224k

9. Russell AJ, Westwood IM, Crawford MHJ et al (2009) Selective small molecule inhibitors of the potential breast cancer marker, human arylamine N-acetyltransferase 1, and its murine homologue, mouse arylamine N-acetyltransferase 2. Bioorganic Med Chem 17:905–918. doi:10.1016/j.bmc.2008.11.032

10. Li M, Xu C, Wu L et al (2013) Self-assembled peptide-polyoxometalate hybrid nanospheres: two in one enhances targeted inhibition of amyloid β-peptide aggregation associated with Alzheimer's disease. Small 9:3455–3461. doi:10.1002/smll.201202612

11. Henary MM, Wu Y, Fahrni CJ (2004) Zinc(II)-selective ratiometric fluorescent sensors based on inhibition of excited-state intramolecular proton transfer. Chem A Eur J 10:3015–3025. doi:10.1002/chem.200305299

12. Munday R, Smith BL, Munday CM (2005) Effect of inducers of DT-diaphorase on the haemolytic activity and nephrotoxicity of 2-amino-1,4-naphthoquinone in rats. Chem Biol Interact 155:140–147. doi:10.1016/j.cbi.2005.06.001

13. Doroshenko AO, Matsakov AY, Nevskii OV, Grygorovych OV (2012) Excited state intramolecular proton transfer reaction revisited: S1 state or general reversibility? J Photochem Photobiol A Chem 250:40–49. doi:10.1016/j.jphotochem.2012.09.010

14. Paul BK, Guchhait N (2011) TD-DFT investigation of the potential energy surface for Excited-State Intramolecular Proton Transfer (ESIPT) reaction of 10-hydroxybenzo[h]quinoline: topological (AIM) and population (NBO) analysis of the intramolecular hydrogen bonding interaction. J Lumin 131:1918–1926. doi:10.1016/j.jlumin.2011.04.046

15. Lee J, Kim CH, Joo T (2013) Active role of proton in excited state intramolecular proton transfer reaction. J Phys Chem A 117:1400–1405. doi:10.1021/jp311884b

16. Basarić N, Cindro N, Hou Y et al (2011) Competing photodehydration and excited-state intramolecular proton transfer (ESIPT) in adamantyl derivatives of 2-phenylphenols. Can J Chem 89:221–234. doi:10.1139/V10-102

17. Pushpam S, Kottaisamy M, Ramakrishnan V (2013) Dynamic quenching study of 2-amino-3-bromo-1,4-naphthoquinone by titanium dioxide nano particles in solution (methanol). Spectrochim Acta Part A Mol Biomol Spectrosc 114:272–276. doi:10.1016/j.saa.2013.05.038

18. Salunke-Gawali S, Pawar O, Nikalje M et al (2014) Synthesis, characterization and molecular structures of homologated analogs of 2-bromo-3-

(n-alkylamino)-1,4-napthoquinone. J Mol Struct 1056–1057:97–103. doi:10.1016/j.molstruc.2013.10.016

19. Pal S, Jadhav M, Weyhermüller T et al (2013) Molecular structures and antiproliferative activity of side-chain saturated and homologated analogs of 2-chloro-3-(n-alkylamino)-1,4-napthoquinone. J Mol Struct 1049:355–361. doi:10.1016/j.molstruc.2013.06.062

20. Charaf-Eddin A, Planchat A, Mennucci B et al (2013) Choosing a functional for computing absorption and fluorescence band shapes with TD-DFT. J Chem Theory Comput 9:2749–2760. doi:10.1021/ct4000795

21. Laurent AD, Jacquemin D (2013) TD-DFT benchmarks: a review. Int J Quantum Chem 113:2019–2039. doi:10.1002/qua.24438

22. Miranda FS, Ronconi CM, Sousa MOB et al (2014) 6-Aminocoumarin-naphthoquinone conjugates: design, synthesis, photophysical and electrochemical properties and DFT calculations. J Braz Chem Soc 25:133–142. doi:10.5935/0103-5053.20130279

23. Jacquemin D, Perpte EA, Scuseria GE et al (2008) TD-DFT performance for the visible absorption spectra of organic dyes: conventional versus long-range hybrids TD-DFT performance for the visible absorption spectra of organic dyes: conventional versus long-range hybrids. J Chem Theory Comput 123–135. doi:10.1021/ct700187z

24. Castilho-Almeida EW, De Almeida WB, Dos Santos HF (2013) Conformational analysis of lignin models: a chemometric approach. J Mol Model 19:2149–2163. doi:10.1007/s00894-012-1689-4

25. de Azevedo ALMS, Neto BB, Scarminio IS et al (1996) A chemometric analysis of ab initio vibrational frequencies and infrared intensities of methyl fluoride. J Comput Chem 17:167–177. doi:10.1002/(SICI)1096-987X(19960130)17:2<167:AIDJCC4>3.0.CO;2-U

26. Barboza CA, Vazquez PAM, Mac-Leod Carey D, Arratia-Perez R (2012) A TD-DFT basis set and density functional assessment for the calculation of electronic excitation energies of fluorene.Int J Quantum Chem 112:3434–3438. doi:10.1002/qua.24300

27. Ferreira MMC (2002) Multivariate QSAR. J Braz Chem Soc 13:742–753. doi:10.1590/S0103-50532002000600004

28. Jacquemin D, Peltier C, Ciofini I (2010) Visible spectrum of naphthazarin investigated through time-dependent density functional theory. Chem Phys Lett 493:67–71. doi:10.1016/j.cplett.2010.04.071

29. Boo BH, Lee JK, Lim EC (2008) Ab initio, DFT, and spectroscopic studies of excited-state structure and dynamics of 9-ethylfluorene. J Mol Struct 892:110–115. doi:10.1016/j.molstruc.2008.05.004

30. Perpète EA, Lambert C, Wathelet V et al (2007) Ab initio studies of the λmax of naphthoquinones dyes. Spectrochim Acta Part A Mol Biomol Spectrosc 68:1326–1333. doi:10.1016/j.saa.2007.02.012

31. Kavitha R, Stalin T (2014) A highly selective chemosensor for colorimetric detection of Hg2+ and fluorescence detection of pH changes in aqueous solution. J Lumin 149:12–18. doi:10.1016/j.jlumin.2013.11.044

32. Imberty A, Tran V, Pérez S (1990) Relaxed potential energy surfaces of N-linked oligosaccharides: the mannose-$\alpha(1 \rightarrow 3)$-mannose case. J Comput Chem 11:205–216. doi:10.1002/jcc.540110206

33. Poleshchuk OK, Yureva AG, Filimonov VD, Frenking G (2009) Study of a surface of the potential energy for processes of alkanes free-radical iodination by B3LYP/DGDZVP method. J Mol Struct THEOCHEM 912:67–72. doi:10.1016/j.theochem.2009.03.001

34. Chen K, Yan W, Zhang X et al (2015) Optimization of process variables in the synthesis of isoamyl isovalerate using sulfonated organic heteropolyacid salts as catalysts. J Braz Chem Soc 26:600–608. doi:10.5935/0103-5053.20150015

35. Box GEP, Draper NR (1987) Empirical model-building and response surfaces, 1st edn. Wiley, New York

36. Katti DR, Schmidt SR, Ghosh P, Katti KS (2005) Modeling the response of pyrophyllite interlayer to applied stress using steered molecular dynamics. Clays Clay Miner 53:171–178. doi:10.1346/CCMN.2005.0530207

37. Stanton JF, Gauss J, Ishikawa N, Head-Gordon M (1995) A comparison of single reference methods for characterizing stationary points of excited state potential energy surfaces. J Chem Phys 103:4160–4174. doi:10.1063/1.469601

38. Sandhoefer B, Kossmann S, Neese F (2013) Derivation and assessment of relativistic hyperfine-coupling tensors on the basis of orbital-optimized second-order Møller–Plesset perturbation theory and the second-order Douglas–Kroll–Hess transformation. J Chem Phys 10(1063/1):4792362

39. Glaser R, Chen N, Wu H et al (2004) 13C NMR study of halogen bonding of haloarenes: measurements of solvent effects and theoretical analysis. J Am Chem Soc 126:4412–4419. doi:10.1021/ja0383672

40. Solimannejad M, Malekani M, Alkorta I (2010) Theoretical study of the halogen-hydride complexes between XeH2 and carbon halogenated derivatives. J Mol Struct THEOCHEM 955:140–144. doi:10.1016/j.theochem.2010.06.004

41. Poorabdollah H, Omidyan R, Solimannejad M, Azimi G (2014) Hydrogen bond strengthening of cis-trans glyoxal dimers in electronic excited states: a theoretical study. Spectrochim Acta A Mol Biomol Spectrosc 122:337–342. doi:10.1016/j.saa.2013.11.034

42. Li X-H, Yong Y-L, Cui H-L et al (2015) Theoretical investigation on vibrational spectra, first order hyperpolarizability and NBO analysis of 4-phenylpyridinium hydrogen squarate. Spectrochim Acta A Mol Biomol Spectrosc 147:14–19. doi:10.1016/j.saa.2015.03.060

43. Kobayashi K, Sasaki A, Takeuchi H, Suginome H (1992) Photoinduced molecular transformations. Part 127. A new [2 + 2] photoaddition of 2-amino-1,4-

naphthoquinone with vinylarenes and the synthesis of 2,3-dihydronaphtho[1,2-b]furan-4,5-diones and 2,3-dihydronaphtho[2,3-b]furan-4,9-diones. J Chem Soc Perkin Trans 1:115–121. doi:10.1039/P19920000115

44. Yasumatsu H, Jeung GH (2014) Ab initio study on electronically excited states of lithium isocyanide, LiNC. Chem Phys Lett 591:25–28. doi:10.1016/j.cplett.2013.11.005

45. Jacquemin D, Planchat A, Adamo C, Mennucci B (2012) TD-DFT assessment of functionals for optical 0-0 transitions in solvated dyes. J Chem Theory Comput 8:2359–2372. doi:10.1021/ct300326f

46. Cancès E, Mennucci B, Tomasi J (1997) A new integral equation formalism for the polarizable continuum model: theoretical background and applications to isotropic and anisotropic dielectrics. J Chem Phys 107:3032. doi:10.1063/1.474659

47. Cossi M, Barone V, Cammi R, Tomasi J (1996) Ab initio study of solvated molecules: a new implementation of the polarizable continuum model. Chem Phys Lett 255:327–335. doi:10.1016/0009-2614(96)00349-1

48. Thompson LM, Lasoroski A, Champion PM et al (2014) Analytical harmonic vibrational frequencies for the green fluorescent protein computed with ONIOM: chromophore mode character and its response to environment. J Chem Theory Comput 10:751–766. doi:10.1021/ct400664p

49. Trani F, Scalmani G, Zheng G et al (2011) Time-dependent density functional tight binding: new formulation and benchmark of excited states. J Chem Theory Comput 7:3304–3313. doi:10.1021/ct200461y

50. Radulović NS, Blagojević PD, Skropeta D (1997) Average mass scan of the total ion chromatogram versus percentage chemical composition in multivariate statistical comparison of complex volatile mixtures. J Braz Chem Soc 21:2319–2326. doi:10.1590/S0103-50532010001200020

51. Yanai T, Tew DP, Handy NC (2004) A new hybrid exchangecorrelation functional using the Coulomb-attenuating method (CAM-B3LYP). Chem Phys Lett 393:51–57. doi:10.1016/j.cplett.2004.06.011

52. Kobayashi R, Amos RD (2006) The application of CAM-B3LYP to the charge-transfer band problem of the zincbacteriochlorin-bacteriochlorin complex. Chem Phys Lett 420:106–109. doi:10.1016/j.cplett.2005.12.040

53. Dos Santos JC, De França JA, Do Nascimento Aquino LE et al (2014) Theoretical calculation and structural studies for a new nitrogen derivative from nor-lapachol. J Mol Struct 1060:233–238. doi:10.1016/j.molstruc.2013.12.047

54. Hertwig RH, Koch W (1997) On the parameterization of the local correlation functional. What is Becke-3-LYP? Chem Phys Lett 268:345–351. doi:10.1016/S0009-2614(97)00207-8

55. Peach MJG, Helgaker T, Sałek P et al (2006) Assessment of a Coulomb-attenuated exchange-correlation energy functional. Phys Chem Chem Phys 8:558–562. doi:10.1039/b511865d

56. Jacquemin D, Preat J, Wathelet V, Perpète EA (2006) Time dependent density functional theory determination of the absorption spectra of naphthoquinones. Chem Phys 328:324–332. doi:10.1016/j.chemphys.2006.07.037

57. Jacquemin D, Perpète Ea, Ciofini I, Adamo C (2008) Fast and reliable theoretical determination of pKa* for photoacids. J Phys Chem A 112:794–796. doi:10.1021/jp7105814

Supplementary Material

S1. Potential Energy Surface
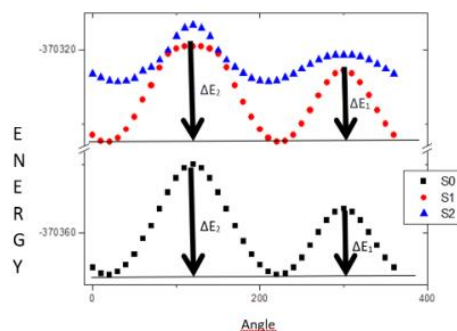
Figure S1.A – Potential energy Surface for the keto form of ANQ in ground state (S0) and excited State (S1 and S2).
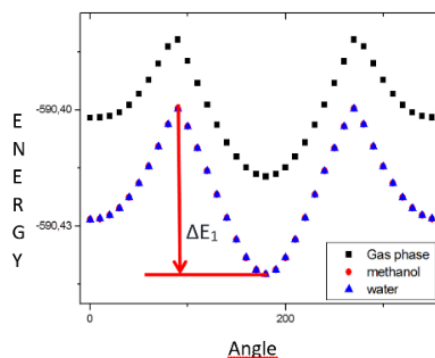
Figure S1.B – Potential Energy Surface for the Enol form of ANQ in ground state (S0) and excited State (S1 and S2).

Table S1.A – Energy values for the each Functional DFT tested in ground State and Excited State for the keto form of ANQ.

Functional	$\Delta E1$ (kcal/mol)	$\Delta E2$ (kcal/mol)
ANQ - B3LYP	9.58	16.04
ANQ - B3PW91	9.62	16.09
ANQ - MPW1PW91	9.30	15.81
ANQ – PBEPBE	11.37	17.72
ANQ (ES) – B3LYP	1.06	7.09
ANQ (ES) – B3PW91	6.30	9.55
ANQ (ES) – MPW1PW91	5.77	9.20
ANQ (ES) – PBEPBE	7.15	10.01

Table S1.B – Energy values for ground state and excited-state, wavelength and Oscillator strength from ANQ.

Funcional	E0 (a.u.)	E1 (eV)	λ (nm)	f
PBEPBE	-589.82	2.97	417.38	0,11
B3PW91	-590.21	3.30	375.52	0,20
B3LYP	-590.45	3.72	333.21	0.30
CAM-B3LYP	-590.25	3.85	321.81	0.16
ωB97XD	-590.25	3.50	353.81	0.18
MPW1PW91	-590.39	3.86	320.41	0.34

S2. Geometry and Structure parameters.

Table S2.A – Dihedral angle and distances interatomic values in keto form of ANQ using DFT/B3LYP and MP2 level.

Level	Solvents	Dihedral Angle (O=C-C-N)	D (C = O)	D (N – H)	D (N – C)	D (C – C)	D (C = C)
B3LYP	Gas Phase	-3.13	1.23*	1.01	1.36	1.51	1.37
	Methanol	-0.081	1.23	1.01	1.34	1.51	1.37
	Chloroform	-1.27	1.23	1.01	1.35	1.51	1.37
MP2	Gas Phase	-4.58	1.24	1.01	1.36	1.50	1.37
	Methanol	-3.01	1.24	1.01	1.36	1.51	1.38
	Chloroform	-3.65	1.24	1.01	1.36	1.50	1.38

* Distance in Angstrons;

Table S2.B – Dihedral angle and distances interatomic values in enol form of ANQ using DFT/B3LYP and MP2 level.

Level	Solvents	Dihedral Angle (O-C-C-N)	D* (C – O)	D (O – H)	D (N – C)	D (N – H)	D (C – C)
B3LYP	Gas Phase	0.013	1.43*	0.96	1.47	1.00	1.37
	Methanol	0.013	1.43	0.96	1.47	1.00	1.37
	Water	0.013	1.43	0.96	1.47	1.00	1.37
MP2	Gas Phase	0.013	1.43	0.96	1.47	1.00	1.37
	Methanol	0.013	1.43	0.96	1.47	1.00	1.37
	Water	0.013	1.43	0.96	1.47	1.00	1.37

*Distances in Angstrons.

S3. Response Surface
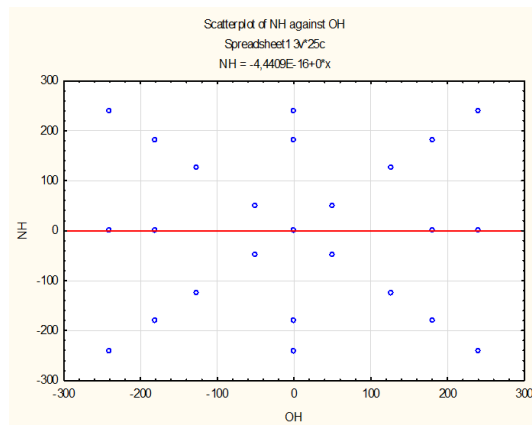
Figure S3.A – Map of points for calculation of the Response Surface relative for the dihedral angle NH and OH.
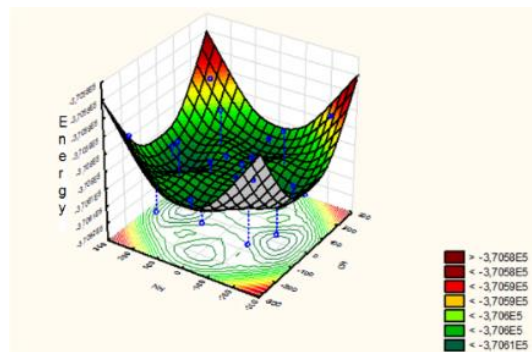
Figure S3.B – Response Surface for the Ground State in Gas Phase for the enol form of ANQ.
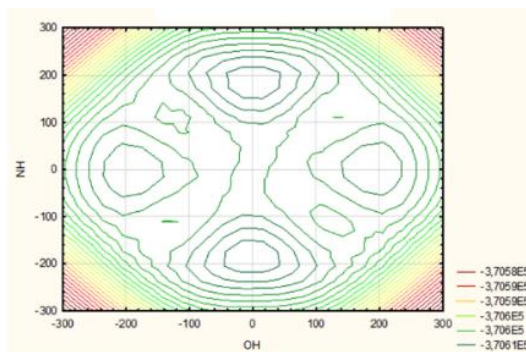
Figure S3.C – Map of contours for the ground state in gas Phase.
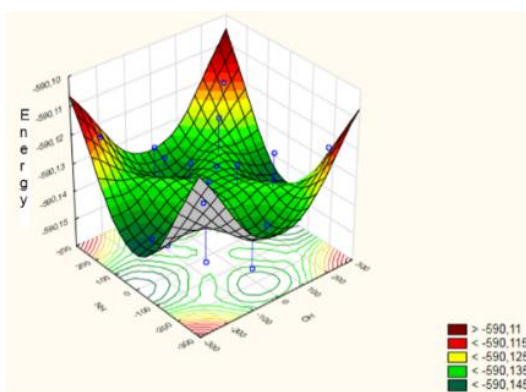
Figure S3.D – Response Surface for the Excited State in Gas Phase for the Enol Form of ANQ.
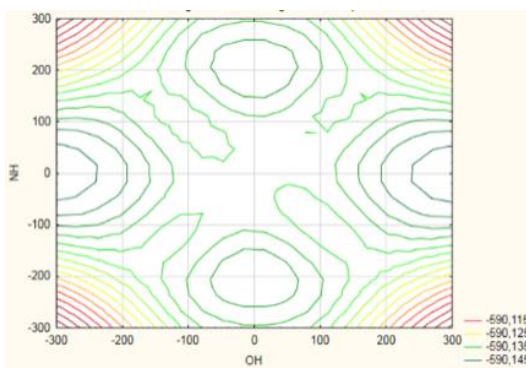
Figure S3.E – Map of Contours for the Excited State in Gas Phase.
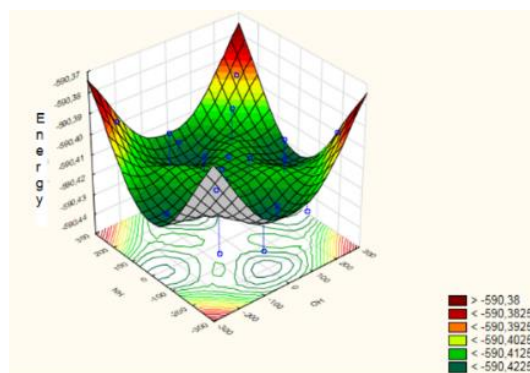
Figure S3.F – Response surface for the ground state in water for the enol form of ANQ.
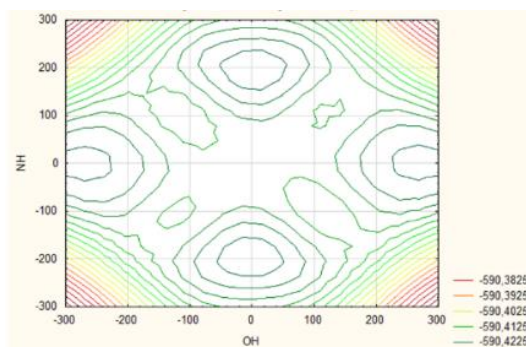
Figure S3.G – Map of contours for the ground state in water.
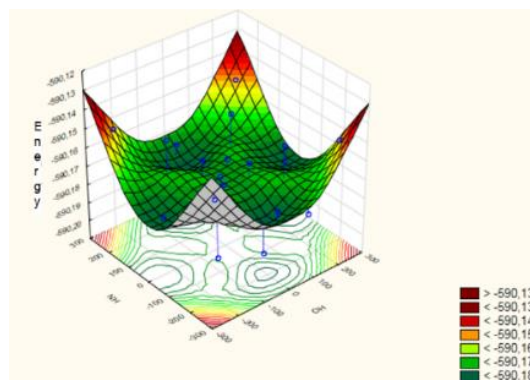
Figure S3.H – Response surface for the ground state in methanol for the enol form of ANQ.
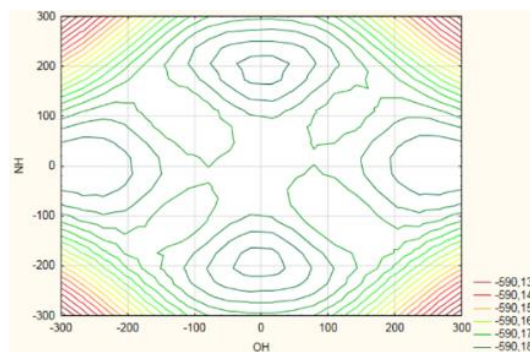
Figure S3.I – Map of contours for the ground state in methanol.

Table S3.A - Dihedral angle values employed in the response surface and their respective energy values.

Point	Dihedral Angle 1	Dihedral Angle 2	Energy (kcal.mol^{-1})
1	-40	220	17.37*
2	-40	180	11.60
3	-40	140	18.56
4	40	220	17.43
5	40	180	10.97
6	40	140	17.05
7	0	220	5.83
8	0	180	0.00
9	0	140	6.14
10	0	120	12.60
11	0	200	1.50
12	-60	180	20.82
13	60	180	20.25

*Relative value for the minimum result in kcal/mol.

S4. HCA and PCA

Table S4.A - Factor coordinates of the variables based on correlations.

Variable	Factor 1	Factor 2	Factor 3	Factor 4	Factor 5	Factor 6
1	-0.99	0.04	-0.01	0.00	-0.00	-0.00
2	-0.99	-0.03	-0.00	0.01	0.00	0.00
3	-0.99	-0.01	0.00	0.00	0.00	0.00
4	-0.99	-0.13	-0.00	-0.02	0.00	-0.00
5	-0.99	0.04	-0.01	0.00	-0.00	-0.00
6	-0.99	-0.02	-0.00	0.01	0.00	0.00
7	-0.99	-0.01	0.00	0.00	0.00	0.00
8	-0.99	-0.12	-0.01	-0.01	-0.01	0.00
9	-0.99	0.06	-0.03	-0.00	0.00	0.00
10	-0.99	-0.03	0.00	0.01	0.00	-0.00
11	-0.99	0.02	0.01	-0.00	-0.00	0.00
12	-0.99	0.06	0.02	-0.02	0.00	-0.00
13	-0.99	0.06	-0.03	-0.00	0.00	0.00
14	-0.99	-0.02	0.00	0.01	0.00	-0.00
15	-0.99	0.03	0.01	-0.00	-0.00	0.00
16	-0.99	0.05	0.02	-0.02	0.00	-0.00

Table S4.B - Factor coordinates of cases based on correlations.

Functional	Factor 1	Factor 2	Factor 3	Factor 4	Factor 5	Factor 6
B3LYP	0.05	-0.30	0.01	0.10	0.00	-0.00
CAM-B3LYP	4.40	0.08	0.08	-0.02	-0.01	-0.01
B3PW91	0.17	-0.26	-0.07	-0.04	-0.02	0.01
MPW1PW91	1.28	-0.16	0.01	-0.06	0.03	0.00
PBEPBE	-4.93	0.09	0.09	0.00	-0.00	0.02
ωB97XD	4.48	0.33	-0.05	0.04	0.00	0.01

Table S4.C - Principal Components Analysis Summary.

Component	R^2X	R^2X (Cumul.)	Eigenvalues	Q^2	Limit	Q^2 (Cumul.)	Significance	Iterations
1	0.99	0.99	15.93	0.99	0.21	0.99	S	2
2	0.01	0.99	0.06	0.77	0.25	0.99	S	3

Table S4.D - Eigenvalues of correlation matrix and related statistics.

	Eigenvalue	% Total Variance	Cumulative Eigenvalue	Cumulative %
1	15.93	99.56	15.93	99.56
2	0.06	0.38	15.99	99.94
3	0.00	0.03	15.99	99.97
4	0.00	0.02	15.99	99.99
5	0.00	0.00	16.00	99.99
6	0.00	0.00	16.00	100.00

Table S4.E - Descriptive Statistics for Cluster contains 14 variables.

Functional	Mean	Standard	Variance
B3LYP	9.95	14.54	211.64
CAM-B3LYP	-30.01	21.38	457.25
B3PW91	8.44	15.07	227.11
MPW1PW91	-1.59	16.79	282.23
PBEPBE	56.40	13.49	182.09
ωB97XD	-31.09	20.05	402.09
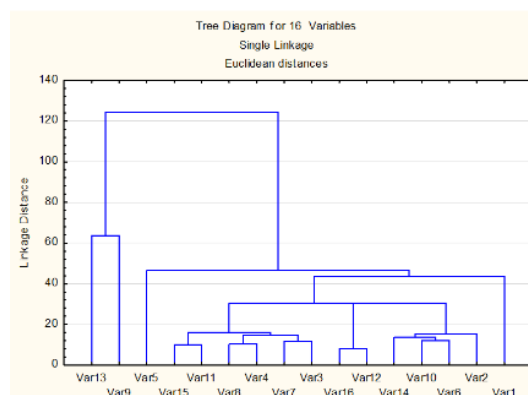
Figure S4.A – Dendogram for the variables.

Table S4.F – Error matrices from ANQ in methanol solvent using IEFPCM and I-PCM methods for calculating the wavelength

	IEFPCM						
	Methanol						
	λ1	λ2		λ3		λ4	
Experimental	471	337	330	281	287	264	294
B3LYP	-14,02	-0,87	6,13	22,33	16,33	37,85	7,85
CAM-B3LYP	-70,48	-40,44	-33,44	-11,51	-17,51	5,46	-24,54
B3PW91	-15,66	-3,6	3,4	21,29	15,29	37,54	7,54
MPW1PW91	-31,13	-13,16	-6,16	14,04	8,04	29,14	-0,86
PBEPBE	56,45	38,9	45,9	59,06	53,06	63,77	33,77
ωB97XD	-68,3	-41,23	-34,23	-12,3	-18,3	1,55	-28,45
	I-PCM						
	Methanol						
	λ1	λ2		λ3		λ4	
Funcional	471	337	330	281	287	264	294
B3LYP	69	-8,93	-1,93	25,76	19,76	21,89	-8,11
CAM-B3LYP	-7,95	-44,18	-37,18	-11,87	-17,87	-19,17	-49,17
B3PW91	72,68	-11,94	-4,94	25,07	19,07	21,25	-8,75
MPW1PW91	50,98	-20,4	-13,4	14,91	8,91	12,71	-17,29
PBEPBE	168,64	28,14	35,14	73,92	67,92	87,85	57,85
ωB97XD	0,8	-45,7	-38,7	-12,91	-18,91	-20,75	-50,75

S5. ESIPT process.
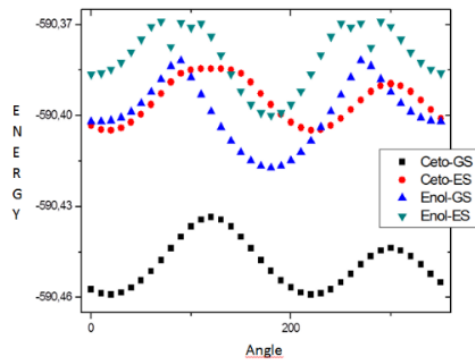
Figure S5.A – Potential energy surface for keto-Enol form in ground and excited state in gas phase.
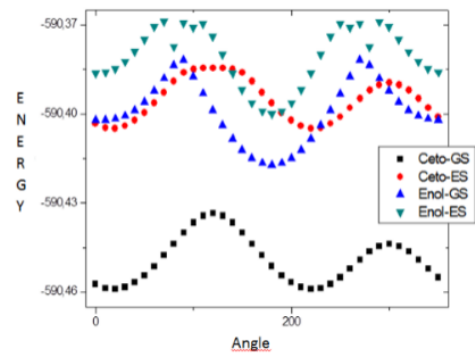
Figure S5.B – Potential energy surface for keto-enol form in ground and excited state in methanol.
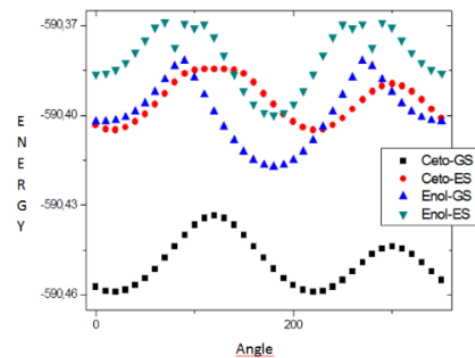
Figure S5.C – Potential energy surface for keto-enol form in ground and excited state in water.

ARTIGO 3 INSIGHTS INTO THE VALUE OF STATISTICAL MODELS AND RELATIVISTIC EFFECTS FOR THE INVESTIGATION OF HALOGENATED DERIVATIVES OF FLUORESCENT PROBES.

Insights into the value of statistical models and relativistic effects for the investigation of halogenated derivatives of fluorescent probes

Abstract

In recent years, diagnosis of diseases worldwide has been of much interest to the scientific community. Among these diagnosis methods, fluorescence spectroscopy has shown promise. Naphthoquinone and their halogenated derivatives have fluorescent properties and the presence of such substituents promote changes in the spectroscopic properties of the compounds. These properties can be studied by time dependent density functional theory methods. Relativistic effects such as spin–orbit coupling, the Hamiltonian relativistic and the basis set including relativistic corrections are essential for the accurate calculation of spectroscopic properties. For the selection of which of these factors are important for the halogenated derivatives naphthoquinone (F, Cl, Br and I) were employed in a factorial design of the 33 Type, known as a Box–Benhken design. It was observed that the DKH2 Hamiltonian and the basis set TVZ_DKH were significant for studying spectroscopic properties of these compounds. Using these parameters, the ESIPT process was investigated for halogenated compounds of naphthoquinone. It was observed that compounds containing Cl, Br and I do not have the ESIPT process, while a compound containing F showed the process having energy values, 4.69 eV for absorption energy, −1.58 eV for the proton transfer energy and 1.87 eV for the emission energy. We believe that the current study can assist in understanding the ESIPT behavior of ANQ derivatives and why the relativistic effects affect this process.

1 Introduction

In the last decade, the interest in photo physics and photochemistry processes has dramatically grown [2]. To date, fluorescence techniques exhibit several industrial and biomedical applications, such as photocatalytic [2], photo

induced isomerization of cis–trans [3], white organic light emitted dye [4] and can be used as fluorescent probes for image diagnosis [5]. This outlook is currently also reinforced by the large number of fluorescent compounds with biological and technological interest. In this context, one important class of compounds that exhibit fluorescent properties are the naphthoquinone derivatives [6]. These compounds of natural origin can be considered antitumor, antifungal, and antimalarial drugs [7]. Naphthoquinone derivatives have also been tested by many research groups [6, 8] as fluorescent probes for breast and buccal cancer with promising results [6, 9].

It is well known that structural modifications, such as a halogen addition, of potential fluorescent probe candidates can provide dramatic changes in their spectroscopic properties, exhibiting new absorption and emission regions, which can be appreciated for the generation of more efficient fluorescent probes [10]. In this context, halogen derivatives of naphthoquinones were studied by fluorescent spectroscopy [11], Raman [12] and UV–VIS techniques [3] for evaluation of their absorption and emission parameters [11]. Recently, theoretical calculations [13] have also been employed for the study of the Homo–Lumo barrier and other electronic properties [11] of this class of compounds.

Nevertheless, one of the greatest challenges is to investigate the spectroscopic parameters of halogen derivatives due to several electronic and structural effects that can modulate the excited-state properties of those compounds [11]. Despite several efforts, surprisingly little detailed theoretical work has appeared on the analysis of the different fluorescence mechanisms for naphthoquinone derivatives as well as the development of computational strategies, including relativistic effects, able to accurately reproduce spectroscopic parameters of halogen derivatives.

Different theoretical methodologies such as the complete active space self-consistent field (CASSCF), complete active space with second-order

perturbation theory (CASPT2), multireference methods and TDDFT techniques can be used for analysis of emission and absorption parameters [3, 14]. It should be kept in mind, however, that the use of time dependent density functional theory (TD-DFT) has provided a promising and accurate alternative for the study of spectroscopic properties, such as vertical energy values, fluorescent parameters or excitation properties of molecules in condensed phase [15–17].

In this context, the accurate description of electronic properties of each atom has great impact on the spectroscopic parameters of the molecule [18]. Among the various parameters and effects that can modulate the electronic properties of heavy atoms, relativistic effects play a crucial role on the spectroscopic properties [18]. However, these effects are complicated to model and generally neglected. In fact, various aspects of the emission and absorption process of organic compounds containing bromide and iodide atoms reveal a great influence of relativistic effects [19].

Currently, relativistic effects are in general employed for theoretical calculations of gold [19], platinum [20], and gadolinium [21] atoms as well as metallic complexes with heavy atoms. Even though this kind of effect in organic systems has been widely neglected spin–orbit coupling, mass/velocity and Darwin effects can strongly influence spectroscopic properties, such as emission and absorption parameters of organic molecules in condensed phase [19,22].

One way of including the relativistic effects is to apply the relativistic Hamiltonian, which involves the resolution of Dirac's equation [23, 24]. The Douglas–Kroll–Hess (DKH) approximation, which transforms the Dirac's Hamiltonian of four components into two components, is one of the most used methods to access the relativistic effects [25]. Another method extensively cited in the literature is the zero-order of regular approximation (ZORA) [26], employing the Pauli's approximation for the resolution of Dirac's equation for chemical compounds [27, 28]. This method points out an alternative to solve the

Dirac's equation for the non-relativistic limit and ignores the contributions of the first order within the Pauli method [25, 29].

Besides modifying, the Hamiltonian [30] of the system to take basis sets that include relativistic correction is another way of introducing the relativistic effects in the calculations [28]. The basic sets simulate the relativistic corrections implemented by the Dirac equation, by incorporating the relativistic correction for electronic properties. Many research groups have developed basis sets that have generated similar results to the ZORA [31] and DKH approximations [32]. For instance, the Ahlrichs TZV basis set [31–33] has some basis set with relativistic approximation, like TZV_DKH or TZV_ZORA [32]. Finally, relativistic effects can also be included into the system by the introduction of spin–orbit coupling. The spin–orbit coupling is related to the splitting of the energy levels for the heavy atoms. In many cases, this splitting can influence electronic properties of the compounds [34]. The spin–orbit coupling can be investigated using approaches, such as effective nuclear charge (SOC-ENC) or effective nuclear charge with mean field approach (SOC-ENC-MFA) [32, 35, 36].

Since many theoretical strategies exist to incorporate the relativistic effects on the electronic structure calculation, to select one specific approach is a difficult task and a critical evaluation is necessary. This outlook is aggravated in the case of fluorescent probes that contain heavy atoms, because the impact of relativistic effects on spectroscopic properties of those organic molecules has been little explored in literature and can be significant.

Keeping this in view, the Hamiltonian used the incorporation or not of spin–orbit coupling and relativistic corrections for basis sets are the three main parameters in relativistic calculations, which in turn can provide vital clues about the type of modifications that might be desirable to increase the accuracy.

Chemometric techniques such as the experimental design or factorial model can assist in the choosing the best conditions and parameter calculation

evaluations [37]. Actually, the factorial model is a statistical approach involving the building of the factor combinations selecting those that are significant from the parameters under study [38, 39]. The factorial model can be modeled in different ways employing two or three levels for each parameter (2^K, 3^K…), and in each level employing two (2^2, 2^3,…), three (3^2, 3^3,…) or a larger number of parameters in order to obtain the correct interpretation of the results [40].

In the present work, the 3^3 factorial model, the Hamiltonian, the spin–orbit coupling and the basis sets including relativistic corrections have been applied for the evaluation of the relativistic methods effect on the absorption process of halogen derivatives of 2-amino-1,4-naphthoquinones. The energy barriers involved in the excited-state intramolecular proton transfer (ESIPT) process for these halogen derivatives employing the selected methodology were evaluated afterward.

2 Computational details

The theoretical calculations were performed in the ORCA program [41]. The calculations for the ground state (S_0) and eight excited states were carried out at DFT and TDDFT level of theory using the B3LYP functional [42], respectively. The basis set employed in the study is described in Table 1 as the parameter B. The halogen derivatives for the 2-amino-3-halo-1,4-naphthoquinone were evaluated for the four halogens, F, Cl, Br and I [43] according to Fig. 1. In order to take into account environment effect methanol was taken, as there are experimental results available for this solvent [43, 44]. The COSMO approximation [11, 28, 35] was used in the absorption and fluorescence properties calculations. The Tamm–Dancoff approximation (TDA) [45] method was employed for simulation of the relaxation effect of the solvent in the excited state within the TD-DFT method.
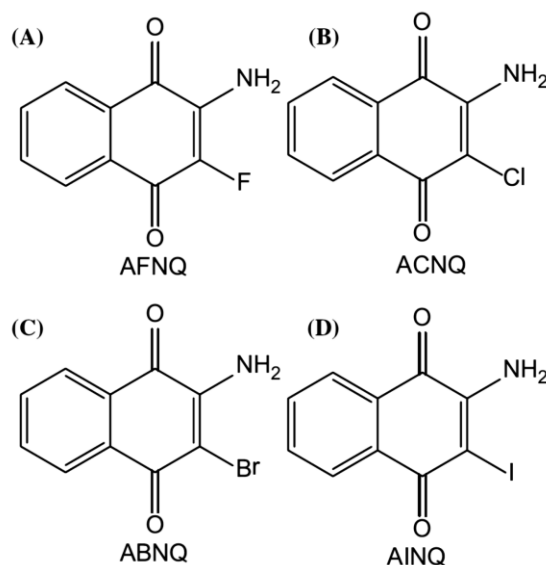
Fig. 1 Chemical structures of 3-halogen derivatives of 2-amino-1,4-naphthoquinone: **a** AFNQ, **b** ACNQ, **c** ABNQ and **d** AINQ

The factorial model calculations were performed in the Statistica® program [46]. The Factorial model employed the 3^K method called the Box–Behnken design [40]. The parameters and levels of the model are reported in Table 1. The first factorial model parameter was the presence of the spin–orbit coupling, in which we evaluate the influence of the spin–orbit coupling on the system, by means of the method spin–orbit coupling effective charge nuclear (SOC-ECN) [41] as well as employing the most complete method spin–orbit coupling effective charge nuclear with mean-field approach (SOC-ECN-MFA) [41] and finally removing the SOC effect. The second parameter in the factorial model was the basis set, and its levels were a nonrelativistic basis set was employed (TVZ) [31, 32], the basis set with ZORA implementation (TVZ_ZORA) [41] was used as a second level of a basis set and the third level was a DKH basis set (TVZ_DKH) [41] implemented in the ORCA program. The third parameter of the factorial model was the Hamiltonian of the system; thus, the non-relativistic Hamiltonian was the first level, the ZORA Hamiltonian the second and the DKH Hamiltonian

was established as the third level [47]. The Box–Behnken design [40, 48, 49] was developed as the twenty-seven (27) cases involving the three parameters and the three levels, which are reported in Table 2. In all the cases, the parameters were evaluated using the ANOVA analysis [50, 51] (Supplementary Material Table S2A), and the acceptance criteria was the Student's t test [38–40].

The study of the ESIPT process was based on the absorption energy (ΔE_1), the proton transfer energy (ΔE_2), as well as the difference in the excited-state (S_1) energies between the keto and enol forms of the compounds. Finally, the fluorescence energy (F_2 or F_1), see Fig. 2, for the energy difference between the excited state (S_1) and ground state (S_0) was also evaluated. Those calculations were carried out at the DFT and TD-DFT levels for ground and excited states, respectively.

Table 1 Levels and parameters for the 3^3 factorial model

Parameters	Level		
	-1	0	+1
(A) Spin-Orbit Coupling	No-SOC	SOC-ECN	SOC-ENC-MFA
(B) Basis set	TVZ	TVZ_ZORA	TVZ_DKH
(C) Relativistic Hamiltonian	No-Relativistic	ZORA	DKH2

3 Results and discussion

3.1 The Box–Behnken design

To our knowledge, there are only two compounds, 2-amino-3-chloro-1,4-naphthoquinone (ACNQ) [44], and 2-amino-3-Bromo-1,4-naphthoquinone (ABNQ) [43], for which experimental values of absorption have been reported, which can be used to develop our statistical model based on the Box–Behnken design [40]. Thus, the other two compounds used in this paper, 2-amino-3-fluor-1,4-naphthoquinone (AFNQ) and 2-amino-3-Iodo-1,4-naphthoquinone (AINQ), will have their energy barriers for the ESIPT process theoretically estimated.

The Box–Behnken design for the four compounds, see Fig. 1, was evaluated according to the combination of the levels reported in Table 1, whose results are described in Table 2.

Through the factorial model, three parameters have been investigated: (1) spin–orbit coupling (parameter A), (2) the basis set used (parameter B), and (3) the relativistic correction for the Hamiltonian of the system (parameter C). The lower level of each parameter was estimated without relativistic effects (no spin–orbit coupling, no relativistic basis set and no relativistic Hamiltonian), the medium level includes spin–orbit coupling SOC-ECN, ZORA basis set and ZORA Hamiltonian and at the high level spin–orbit coupling SOC-ENC-MFA, DKH basis set and DKH2 Hamiltonian. These levels are called levels −1, 0 and +1 on Tables 1 and 2, respectively. It is important to keep in mind that the factorial model 3^3 was developed with twenty-seven combinations from the three levels with three parameters and their interactions.

The TD-DFT method and the COSMO model were employed to calculate the absorption and emission values for the four compounds as well as the values used for the statistical calculations. The selected model for the system was the quadratic model, and the significant effects selected were evaluated for statistical analyses, such as variance analysis (ANOVA), see Supplementary Material Table S2A. It is well known that with this model can get a better description of the interactions and the significance for the studied parameters [38].

3.2 The factorial model for the ACNQ and ABNQ

The experimental values of the absorption wavelength for ACNQ and ABQN are 476 nm [44] and 452 nm [43], respectively. The construction of the factorial design was performed using the error values from the difference between the experimental and theoretical values. According to ANOVA analysis [10, 52] reported in Supplementary Material (Table S2A), only the B and C parameters

were significant for the factorial model for ACNQ, i.e., the basis set and Hamiltonian.

Table 2 3^3 Factorial model listing the levels for the twenty seven cases and the results (wavelength in nm) for the four compounds

Cases	Levels for each parameter			Results			
	A	B	C	AFNQ	ACNQ	ABNQ	AINQ
1	−1	−1	−1	487.8	466.5 (+9.5)	458.7 (+6.7)*	461
2	−1	−1	0	487.8	466.4 (+9.6)	457.2 (+5.2)	460.8
3	−1	−1	1	487.9	466.6 (9.4)	457.7 (+5.7)	462.9
4	−1	0	−1	488	466.7 (+9.3)	457.1 (+5.1)	463.2
5	−1	0	0	488.4	466.9 (+9.1)	458.4 (+6.4)	460.8
6	−1	0	1	488	466.5 (+9.5)	454.2 (+2.2)	460.6
7	−1	1	−1	488	466.7 (+9.3)	459.4 (+7.4)	463.4
8	−1	1	0	488.4	467 (+9)	459.4 (+7.4)	461
9	−1	1	1	488	466.5 (+9.5)	452.7 (+0.7)	460.6
10	0	−1	−1	487.8	466.5 (+9.5)	458.7 (+6.7)	461
11	0	−1	0	487.8	466.4 (+9.6)	457.2 (+5.2)	460.8
12	0	−1	1	487.9	466.6 (+9.4)	457.7 (+5.7)	462.9
13	0	0	−1	488	466.7 (+9.3)	457.1 (+5.1)	463.2
14	0	0	0	488.4	466.9 (+9.1)	458.4 (+6.4)	460.8
15	0	0	1	488	466.5 (+9.5)	454.2 (+2.2)	460.6
16	0	1	−1	488	466.7 (+9.3)	459.4 (+7.4)	463.4
17	0	1	0	488.4	467 (+9)	459.4 (+7.4)	461
18	0	1	1	488	466.5 (+9.5)	452.7 (+0.7)	460.6
19	1	−1	−1	487.8	466.5 (+9.5)	458.7 (+6.7)	461
20	1	−1	0	487.8	466.4 (+9.6)	457.2 (+5.2)	460.8
21	1	−1	1	487.9	466.6 (+9.4)	457.7 (+5.7)	462.9
22	1	0	−1	488	466.7 (+9.3)	457.1 (+5.1)	463.2
23	1	0	0	488.4	466.9 (+9.1)	458.4 (+6.4)	460.8
24	1	0	1	488	466.5 (+9.5)	454.2 (+2.2)	460.6
25	1	1	−1	488	466.7 (+9.3)	459.4 (+7.4)	463.4
26	1	1	0	488.4	467 (+9)	459.4 (+7.4)	461
27	1	1	1	488	466.5 (+9.5)	452.7 (+0.7)	460.6

* Values in parenthesis are errors related to experimental values of 452 and 476 nm for ABNQ and ACNQ, respectively [43, 44]

The variance analysis (ANOVA) is a statistical model used to employ the differences among group means and their associated methods [46, 49, 53]. In the

ANOVA setting, the variance in a variable is divided into parts attributable to different fonts of variation. In other words, ANOVA can be useful for comparing (testing) three or more means (groups or variables) for statistical significance. In this context, Eqs. 1 and 2 represent statistical models to describe the dependence of a factor on the parameters *A*, *B* and *C*.

$$R = 9.35 - 0{,}23B - 0.08B^2 + 0.10C - 0{,}18C^2 + 0.15B * C \qquad \text{eq 1}$$

$$R = 5.20 - 0.70B - 0.95B^2 - 3.53C + 1.70C^2 - 2.85B * C \qquad \text{eq 2}$$

The value 9.35 is the average population of all factorial design responses in Eq. 1 and 5.20 is the value of the average population in Eq. 2. For the B parameter, when the nonrelativistic basis set (TVZ) is modified to the relativistic basis set (TVZ_DKH2), the error value decreases around 0.46 % according to Eq. 1. For the C parameter, the error value increases 0.10 % with the change of the Hamiltonian of the system ongoing from the nonrelativistic to the relativistic Hamiltonian (ZORA or DKH2). The factorial model equation exhibits significant value for the interaction between B and C parameters for ACNQ. An increase in the error value to 0.15 % when the lower level is modified to the high level was observed.

The factorial model for ABNQ showed that only the C parameter was significant. According to ANOVA analysis (see Supplementary Material (Table S2A)) when the level from lower to the higher was modified, the error value decreases 3.53 %, see Table 3.

This feature showed that the relativistic Hamiltonian was essential for the absorption calculation for the bromide derivatives. Interestingly, the relativistic effects were more significant for the bromide derivatives than chloride derivatives.

Table 3 Estimate of the effects, standard error (Std. Err.), the t analysis [t(17)], and the coefficient limit for the 3^3 factorial model for the four compounds.

Factor	Effect	Std.Err.	t (17)	p	−95.% conf. limit	+95.% conf. limit
(a) AFNQ						
Average	488.03	0.02	20,029.61	0.00	487.98	488.08
A	0.00	0.05	−0.00	1.00	−0.12	0.12
A^2	0.00	0.05	−0.00	1.00	−0.10	0.10
B	0.30	0.05	5.03	0.00	0.17	0.42
B^2	0.15	0.05	2.90	0.01	0.04	0.25
C	0.03	0.05	0.56	0.58	−0.09	0.15
C^2	0.25	0.05	4.84	0.00	0.14	0.35
A*B	0.00	0.07	0.00	1.00	−0.15	0.15
A*C	0.00	0.07	0.00	1.00	−0.15	0.15
B*C	−0.05	0.07	−0.68	0.50	−0.20	0.10
(b) ACNQ						
Average	9.35	0.02	331.38	0.00	9.29	9.41
A	0.00	0.06	0.00	1.00	−0.14	0.14
A^2	0.00	0.05	0.00	1.00	−0.12	0.12
B	−0.23	0.06	−3.37	0.01	−0.37	−0.08
B^2	−0.08	0.05	−1.39	0.18	−0.20	0.04
C	0.10	0.06	1.44	0.16	−0.04	0.24
C^2	−0.18	0.05	−3.06	0.01	−0.30	−0.05
A*B	0.00	0.08	0.00	1.00	−0.17	0.17
A*C	0.00	0.08	0.00	1.00	−0.17	0.17
B*C	0.15	0.08	1.77	0.09	−0.02	0.32
(c) ABNQ						
Average	5.20	0.22	23.16	0.00	4.72	5.67
A	0.00	0.54	0.00	1.00	−1.16	1.16
A^2	0.00	0.47	0.00	1.00	−1.00	1.00
B	−0.70	0.54	−1.27	0.22	−1.86	0.46
B^2	−0.95	0.47	−1.99	0.06	−1.95	0.05
C	−3.53	0.54	−6.42	0.00	−4.69	−2.37
C^2	+1.7	0.47	3.56	0.00	0.69	2.70
A*B	0.00	0.67	0.00	1.00	−1.42	1.42
A*C	0.00	0.67	0.00	1.00	−1.42	1.42
B*C	−2.85	0.67	−4.23	0.00	−4.27	−1.42
(d) AINQ						
Average	461.58	0.10	4588.06	0.00	461.37	461.80
A	0.00	0.24	0.00	1.00	−0.51	0.51
A^2	0.00	0.21	0.00	1.00	−0.45	0.45
B	0.10	0.24	0.40	0.68	−0.41	0.61
B^2	−0.08	0.21	−0.39	0.70	−0.53	0.36
C	−1.16	0.24	−4.73	0.00	−1.68	−0.64
C^2	−1.08	0.21	−5.07	0.00	−1.53	−0.63
A*B	0.00	0.30	0.00	1.00	−0.63	0.63
A*C	0.00	0.30	0.00	1.00	−0.63	0.63
B*C	−2.35	0.30	−7.78	0.00	−2.98	−1.71

The B parameter was not relevant for the factorial model analysis for ABNQ compounds. However, it was important for the interaction between B and C parameters. Going on from the lowest level (-1) to the highest ($+1$), the error value decreases 2.85 % as reported in Table 3, indicating that the interaction was significant for the absorption calculation for ABNQ and ACNQ compounds. The equation generated for the ABNQ factorial model is described in Eq. 2. The Pareto graph shown in Supplementary Material Figure S1 exhibits the significant parameters according to Student's t test.

The analysis of those graphics indicates that in all cases the B and C parameters are always significant and for two compounds (ABNQ and AINQ), the interaction between parameter B and C was significant as well. The factorial model generated optimized values for the parameter B (TVZ_DKH) and C (DKH2 Hamiltonian). The parameters described will be used for the wavelength and the energy calculation of the ESIPT process in the third step.

3.3 The factorial model for AFNQ and AINQ

So far, experimental results for AFNQ and AINQ have still not been reported, for this reason, the factorial model used in these cases was developed in comparison with ACNQ and ABNQ. For AFNQ, the ANOVA analysis (in Supplementary Material Table S2A) showed that the B parameter is significant for the absorption calculation, but the C parameter is not.

This feature indicated that the relativistic effects were not important for the fluoride derivatives. In fact, since fluoride is a small atom, the relativistic effects can be neglected for fluoride derivate compounds. Surprisingly, the C^2 quadratic parameter is not neglected in this model. Comparing to the other two models, the relativistic contribution was important to the B parameter. In this case, ongoing from the lower level to the higher level, the wavelength value increases 5.02 %, (see Table 3). The B^2 and C^2 quadratic values increase the wavelength

value of 4.83 and 2.90 %, respectively. Equation 3 shows the factorial model for AFNQ.

Just as the Eqs. 1 and 2, Eqs. 3 and 4 represent statistical models to describe the dependence of a factor on the parameters A, B and C.

$$R = 488.03 + 0.30B + 0.15B^2 + 0.25C^2 \qquad\qquad \text{eq 3}$$

$$R = 461,58 - 1.16C - 1.08C^2 - 2.35B * C \qquad\qquad \text{eq 4}$$

In the factorial model described by Eq. 3, the interaction between B and C is not significant for the absorption calculation. This feature implies that only the isolated parameter was significant for the AFNQ compound. However, for other three models, the interaction between B and C parameters was significant.

For AINQ, for which experimental values are not available, the ANOVA analysis showed that the C parameter is significant according to Eq. 4. Ongoing from the lower level to the medium or higher level, the wavelength decreases 1.16 %. Comparatively, the ABNQ factorial model had a decrease in the wavelength value when going from the lower to the higher level, showing less error for ABNQ. In this way, the AINQ factorial model showed a lesser value for the wavelength and for comparison the lesser error when the DKH2 Hamiltonian is used. The bromide, chloride and iodine atoms have high influence on the relativistic Hamiltonian [35, 54]. The factorial model reinforced this finding. It is important note that the statistical models did not show that the basis set has a significant value for the three compounds; actually, only fluoride was significant. Therefore, the interaction between B and C was significant for ABNQ and AINQ. The interaction between B and C parameters decreased the wavelength values 2.85 and 2.35 %, respectively. ABNQ exhibits the lowest error values ongoing from the lower to the higher level. AINQ displays comparatively the same behavior. In this way, when the level goes from lower to the medium level, the AINQ factorial model decreases 2.35 %. In the other hand, going from the

medium to the higher level, the value decreases another 2.35 %. All ANOVA analyses are shown in Supplementary Material Table S2A for the four compounds regarding the 3^3 factorial model.

3.4 Theoretical calculations for the ESIPT process

The factorial model confirmed that the ideal parameters for spectroscopic properties are the DKH2 Hamiltonian calculation and the relativistic basis set (TVZ_DKH). The spin–orbit coupling is not required. In this regard, we have applied this selected methodology and investigated the ESIPT process for all previous studied compounds and their halogen derivatives
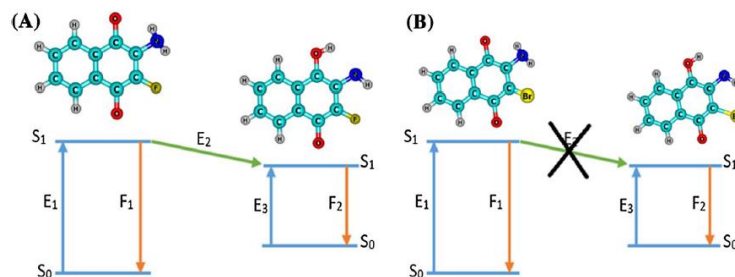
Fig. 2 Energy diagram of the excited-state intramolecular proton transfer (ESIPT) for the four halogen derivative compounds for the 2-amino-1,4-naphthoquinone: **a** the diagram for the ANQ and AFNQ; **b** the diagram for the ACNQ, ABNQ and AINQ.

. The energy analysis considers three different energies: (1) the energy required for the keto form to reach the excited state, the absorption energy (ΔE_1); (2) the energy needed for the conversion from the keto to enol form of the compounds in the excited state, the proton transfer energy (ΔE_2); (3) the energy emitted when the enol form decays from the excited state to the ground state, emission (fluorescence) energy (ΔF_2). The energy values are reported in Table 4. When the ΔE_2 energy was positive, the enol form was more energetic than the keto form and the ESIPT process cannot occur.

In this way, the compounds ACNQ, ABNQ and AINQ cannot exhibit the ESIPT process and the fluorescence occurs by the decaying of the keto form, emitting ΔF_1 energy. But, when the ΔE_2 energy is negative or close to zero, the ESIPT process can occur emitting ΔF_2 energy, the emission energy from the enol form is observed for ANQ and AFNQ. The two possibilities for the emission are showed in Fig. 2 where the first diagram shows the ESIPT process in which the keto form in the excited state is converted to an enol form before decaying to the ground state. In the second diagram, the conversion was not possible and the emission occurs in the keto form. The absorption wavelength calculated showed lower error for ABNQ compared to ANQ, this feature indicated that the model is more accurate for the heavy atoms.

Table 4 Absorption values (ΔE_1), proton transfer (ΔE_2) and emission (ΔF_1 and ΔF_2) energy, fluorescence wavelength (λ_1) and emission color for the four compounds.

Compounds	Absorption Energy (ΔE_1) (eV)	Proton transfer Energy (ΔE_2) (eV)	Emission Energy (ΔF_1) (eV)	Emission Energy (ΔF_2) (eV)	Emission Wavelength (λ_1) (nm)	Emission Color
ANQ	4.69	-1.58	----	1.87	663	Red
AFNQ	4.53	0.56	----	3.12	397	Violet
ACNQ	3.45	1.51	2.93	----	423	Violet
ABNQ	3.48	1.33	2.76	----	449	Blue
AINQ	3.35	1.30	2.81	----	441	Blue

The emission wavelength values (λ_1) observed refers to emission energy (ΔF_1 or ΔF_2, respectively) of each compound, and the value decreases with the increase in substituent mass, see Table 4. These results provide evidence that the increase in mass dispersed more energy into the environment promoting a bathochromic shift. The heavy atoms promoted better dispersion of the electronic density, and this decreases the possibility of the ESIPT process amino group less susceptible to transfer the proton. ANQ emitted at 445 nm (the experimental value

for ANQ is 471 nm) emitting a red color at 663.4 nm. AFNQ emitted at 488 nm and ACNQ emitted at 467 nm (the experimental value for ACNQ is 476 nm [44]). The blue emission was observed for ABNQ, which emitted at 453 nm (the experimental value for ABNQ is 452 nm [43]) and AINQ emitted at 460 nm.

4 Conclusion

The 3^3 factorial model used for the study of the influence of the relativistic effects on spectroscopic parameters showed adequate for the halogen derivatives of ANQ. The experimental design was adequate to evaluate the best theoretical strategy to be employed in the investigation of relativistic effects on spectroscopic properties. The model pointed out that DKH2, the relativistic basis set, as well as the interaction between them, are important parameters for the study. The study showed that the presence of the halogen atoms Cl, Br and I does not favor the ESIPT process. The two compounds exhibit the ESIPT process, ANQ and AFNQ, emitting the red and violet color, respectively. Other compounds do not exhibit ESIPT process, but emit violet (ACNQ) and blue color (ABNQ and AINQ) fluorescence for the keto decay. We believe that the current study can assist in understanding the ESIPT behavior of ANQ derivatives and why the relativistic effects affect the process, as well as what theoretical strategy for the theoretical calculations of this class of compounds is the most appropriate.

References

1. Zhao J, Ji S, Chen Y, et al (2012) Excited state intramolecular proton transfer (ESIPT): from principal photophysics to the development of new chromophores and applications in fluorescent molecular probes and luminescent materials. Phys Chem Chem Phys 14:8803–8817. doi:10.1039/c2cp23144a

2. Zhao G, Northrop BH, Han K, Stang PJ (2010) The effect of intermolecular hydrogen bonding on the fluorescence of a bimetallic platinum complex. J Phys Chem A 114:9007–9013. doi:10.1021/jp105009t

3. Levine BG, Martínez TJ (2007) Isomerization through conical intersections. Annu Rev Phys Chem 58:613 – 634. doi:10.1146/annurev.physchem.57.032905. 104612

4. Park S, Kwon JE, Kim SH, et al (2009) A white-light-emitting molecule : frustrated energy transfer between constituent emitting centers. J Am Chem Soc 131:14043–14049. doi:10.1021/ja902533f

5. Dugave C, Demange L (2003) Cis− trans isomerization of organic molecules and biomolecules : implications and applications †. Chem Rev 103:2475–2532. doi:10.1021/cr0104375

6. Laurieri N, Egleton JE, Varney A et al (2013) A novel color change mechanism for breast cancer biomarker detection: naphthoquinones as specific ligands of human arylamine n-acetyltransferase 1. Plos One. doi:10.1371/journal.pone.0070600

7. Ferreira VF, Jorqueira A, Souza AMT et al (2006) Trypanocidal agents with low cytotoxicity to mammalian cell line: a comparison of the theoretical and biological features of lapachone derivatives. Bioorganic Med Chem 14:5459–5466. doi:10.1016/j.bmc.2006.04.046

8. Ramalho TC, Rocha EP (2016) Probing the ESIPT process in 2-amino-1,4-naphthoquinone: Thermodynamics properties, solvent effect and chemometric analysis. Theor Chem Acc 135:39. doi:10.1007/s00214-015-1786-4

9. Luo Y, Li Y, Qiu KM et al (2011) Metronidazole acid acyl sulfonamide: A novel class of anticancer agents and potential EGFR tyrosine kinase inhibitors. Bioorganic Med Chem 19:6069–6076. doi:10.1016/j.bmc.2011.08.038

10. Bermejo-Bescós P, Martín-Aragón S, Jiménez-Aliaga KL et al (2010) In vitro antiamyloidogenic properties of 1,4-naphthoquinones. Biochem Biophys Res Commun 400:169–174. doi:10.1016/j.bbrc.2010.08.038

11. Guzow K, Milewska M, Czaplewski C, Wiczk W (2010) A DFT/TD DFT study of the structure and spectroscopic properties of 5-methyl-2-(8-quinolinyl)benzoxazole and its complexes with Zn(II) ion. Spectrochim Acta - Part A Mol Biomol Spectrosc 75:773–781. doi:10.1016/j.saa.2009.11.053

12. Tucker SC, Honn KV (2013) Emerging targets in lipid-based therapy. Biochem Pharmacol 85:676–688. doi:10.1016/j.bcp.2012.11.028

13. Yang D, Zhao F, Zheng R et al (2015) A detailed theoretical investigation on the excited-state intramolecular proton-transfer mechanism of 3-BTHPB chemosensor. Theor Chem Acc 134:62. doi:10.1007/s00214-015-1664-0

14. López-de-Luzuriaga JM, Manso E, Monge M, Sampedro D (2015) Dual fluorescence of 4-(dimethylamino)-pyridine: a comparative linear response TDDFT versus state-specific CASSCF study including solvent with the PCM model. Theor Chem Acc 134:55. doi:10.1007/s00214-015-1659-x

15. Jana S, Dalapati S, Ghosh S, Guchhait N (2013) Excited state intramolecular charge transfer process in 5-(4-dimethylaminophenyl)-penta-2,4-dienoic acid ethyl ester and effect of acceptor functional groups. J Photochem Photobiol A Chem 261:31–40. doi:10.1016/j.jphotochem.2013.04.005

16. Rocha MV, Carvalho HW, Lacerda LC et al (2014) Ionic desorption in PMMA-gamma-Fe2O3 hybrid materials induced by fast electrons: an experimental and theoretical investigation. Spectrochim Acta A Mol Biomol Spectrosc 117:276–283. doi:10.1016/j.saa.2013.08.029

17. Mancini DT, Sen K, Barbatti M et al (2015) Excited-state proton transfer can tune the color of protein fluorescent markers. ChemPhysChem 16:3444–3449. doi:10.1002/cphc.201500744

18. Brejc K, Sixma TK, Kitts PA et al (1997) Structural basis for dual excitation and photoisomerization of the Aequorea Victoria green fluorescent protein. Proc Natl Acad Sci 94:2306–2311. doi:10.1073/pnas.94.6.2306

19. Gorin DJ, Toste FD (2007) Relativistic effects in homogeneous gold catalysis. Nature 446:395–403. doi:10.1038/nature05592

20. Philipsen P, van Lenthe E, Snijders J, Baerends E (1997) Relativistic calculations on the adsorption of CO on the (111) surfaces of Ni, Pd, and Pt within the zeroth-order regular approximation. Phys Rev B 56:13556–13562. doi:10.1103/PhysRevB.56.13556

21. Hemmilä I, Laitala V (2005) Progress in lanthanides as luminescent probes. J Fluoresc 15:529–542. doi:10.1007/s10895-005-2826-6

22. Dyall KG, van Lenthe E (1999) Relativistic regular approximations revisited: an infinite-order relativistic approximation. J Chem Phys 111:1366. doi:10.1063/1.479395

23. Kutzelnigg W (1997) Relativistic one-electron Hamiltonians "for electrons only" and the variational treatment of the Dirac equation. Chem Phys 225:203–222. doi:10.1016/S0301-0104(97)00240-1

24. Pyykkö P (2012) Relativistic effects in chemistry: more common than you thought. Annu Rev Phys Chem 63:45–64. doi:10.1146/annurev-physchem-032511-143755

25. Wolf A, Reiher M, Hess BA (2002) The generalized Douglas–Kroll transformation. J Chem Phys 117:9215. doi:10.1063/1.1515314

26. Cheng L, Stopkowicz S, Gauss J (2014) Analytic energy derivatives in relativistic quantum chemistry. Int J Quantum Chem 114:1108–1127. doi:10.1002/qua.24636

27. Wolff SK, Ziegler T, van Lenthe E, Baerends EJ (1999) Density functional calculations of nuclear magnetic shieldings using the zeroth-order regular approximation (ZORA) for relativistic effects: ZORA nuclear magnetic resonance. J Chem Phys 110:7689. doi:10.1063/1.478680

28. Green TFG, Yates JR (2014) Relativistic nuclear magnetic resonance J-coupling with ultrasoft pseudopotentials and the zeroth-order regular approximation. J Chem Phys 140:234106. doi:10.1063/1.4882678

29. Reiher M, Wolf A (2004) Exact decoupling of the Dirac Hamiltonian. II. The generalized Douglas–Kroll–Hess transformation up to arbitrary order. J Chem Phys 121:10945. doi:10.1063/1.1818681

30. Christiansen PA, Ermler WC, Pitzer KS (1985) Relativistic Effects in Chemical Systems. Annu Rev Phys Chem 36:407–432. doi:10.1146/annurev.pc.36.100185.002203

31. Bühl M, Reimann C, Pantazis DA et al (2008) Geometries of third-row transition-metal complexes from density-functional theory. J Chem Theory Comput 4:1449–1459. doi:10.1021/ct800172j

32. Pantazis DA, Chen X, Landis CR, Neese F (2008) All-electron scalar relativistic basis sets for third-row transition metal atoms. J Chem Theory Comput 4:908–919. doi:10.1021/ct800047t

33. Kubica A, Kowalewski J, Kruk D, Odelius M (2013) Zero-field splitting in nickel(II) complexes: a comparison of DFT and multi-configurational wavefunction calculations. J Chem Phys 138:064304. doi:10.1063/1.4790167

34. Arumugam K, Becker U (2014) Computational redox potential predictions: applications to inorganic and organic aqueous complexes, and complexes adsorbed to mineral surfaces. Minerals 4:345–387. doi:10.3390/min4020345

35. Elkechai A, Kias F, Talbi F, Boucekkine A (2014) Redox properties of biscyclopentadienyl uranium(V) imido-halide complexes: a relativistic DFT study. J Mol Model 20:2294. doi:10.1007/s00894-014-2294-5

36. Kühn M, Weigend F (2014) Phosphorescence lifetimes of organic light-emitting diodes from two-component time dependent density functional theory. J Chem Phys 141:224302. doi:10.1063/1.4902013

37. Bonatsou S, Benítez A, Rodríguez-Gómez F et al (2015) Selection of yeasts with multifunctional features for application as starters in natural black table olive processing. Food Microbiol 46:66–73. doi:10.1016/j.fm.2014.07.011

38. de Azevedo ALMS, Neto BB, Scarminio IS et al (1996) A chemometric analysis of ab initio vibrational frequencies and infrared intensities of methyl fluoride. J Comput Chem 17:167–177. doi:10.1002/(SICI)1096-987X(19960130)17:2<167:AIDJCC4>3.0.CO;2-U

39. Ribeiro RLV, Grespan CB, Collins CH et al (1999) Optimization through Factorial Planning of the Use of Ethanol: Water as a Mobile Phase for Reversed Phase HPLC. J High Resolut Chromatogr 22:52–54. doi:10.1002/(SICI)1521-4168(19990101)22:1<52:AID-JHRC52>3.0.CO;2-T

40. Ferreira SLC, Bruns RE, Ferreira HS et al (2007) Box–Behnken design: An alternative for the optimization of analytical methods. Anal Chim Acta 597:179–186. doi:10.1016/j.aca.2007.07.011

41. Neese F (2012) The ORCA program system. Wiley Interdiscip Rev Comput Mol Sci 2:73–78. doi:10.1002/wcms.81

42. Pyykkö P (2004) Theoretical chemistry of gold. Angew Chem Int Ed Engl 43:4412–4456. doi:10.1002/anie.200300624

43. Pushpam S, Kottaisamy M, Ramakrishnan V (2013) Dynamic quenching study of 2-amino-3-bromo-1,4-naphthoquinone by titanium dioxide nano particles in solution (methanol). Spectrochim Acta - Part A Mol Biomol Spectrosc 114:272–276. doi:10.1016/j.saa.2013.05.038

44. Pal S, Jadhav M, Weyhermüller T et al (2013) Molecular structures and antiproliferative activity of side-chain saturated and homologated analogs of 2-

chloro-3-(n-alkylamino)-1,4-napthoquinone. J Mol Struct 1049:355–361. doi:10.1016/j.molstruc.2013.06.062

45. Roemelt M, Beckwith MA, Duboc C et al (2012) Manganese K-edge X-ray absorption spectroscopy as a probe of the metalligand interactions in coordination compounds. Inorg Chem 51:680–687. doi:10.1021/ic202229b

46. Scherzer-Attali R, Farfara D, Cooper I et al (2012) Naphthoquinone-tryptophan reduces neurotoxic Aβ*56 levels and improves cognition in Alzheimer's disease animal model. Neurobiol Dis 46:663–672. doi:10.1016/j.nbd.2012.03.005

47. Haiduke RLA, Comar M, da Silva ABF (2006) The employment of relativistic adapted Gaussian basis sets in Douglas–Kroll–Hess scalar calculations with diatomic molecules. Chem Phys 331:173–177. doi:10.1016/j.chemphys.2006.10.009

48. Aslan N, Cebeci Y (2007) Application of Box–Behnken design and response surface methodology for modeling of some Turkish coals. Fuel 86:90–97. doi:10.1016/j.fuel.2006.06.010

49. Ferreira SLC, Bruns RE, da Silva EGP et al (2007) Statistical designs and response surface techniques for the optimization of chromatographic systems. J Chromatogr A 1158:2–14. doi:10.1016/j.chroma.2007.03.051

50. Owens EA, Hyun H, Tawney JG, et al. (2015) Correlating Molecular Character of NIR Imaging Agents with Tissue-Specific Uptake. J Med Chem 58:4348–4356. doi:10.1021/acs.jmedchem.5b00475

51. Tiang JM, Butcher NJ, Minchin RF (2010) Small molecule inhibition of arylamine N-acetyltransferase Type I inhibits proliferation and invasiveness of MDA-MB-231 breast cancer cells. Biochem Biophys Res Commun 393:95–100. doi:10.1016/j.bbrc.2010.01.087

52. Di Rosso ME, Barreiro Arcos ML, Elingold I et al (2013) Novel o-naphthoquinones induce apoptosis of EL-4 T lymphoma cells through the increase

of reactive oxygen species. Toxicol Vitr 27:2014–2094. doi:10.1016/j.tiv.2013.08.002

53. Bezerra MA, Santelli RE, Oliveira EP et al (2008) Response surface methodology (RSM) as a tool for optimization in analytical chemistry. Talanta 76:965–977. doi:10.1016/j.talanta.2008.05.019

54. Gourlaouen C, Eng J, Otsuka M et al (2015) Quantum chemical interpretation of ultrafast luminescence decay and intersystem crossings in rhenium(I) carbonyl bipyridine complexes. J Chem Theory Comput 11:99–110. doi:10.1021/ct500846n

Supplementary Material

S1. Pareto Chart of Standardized Effects
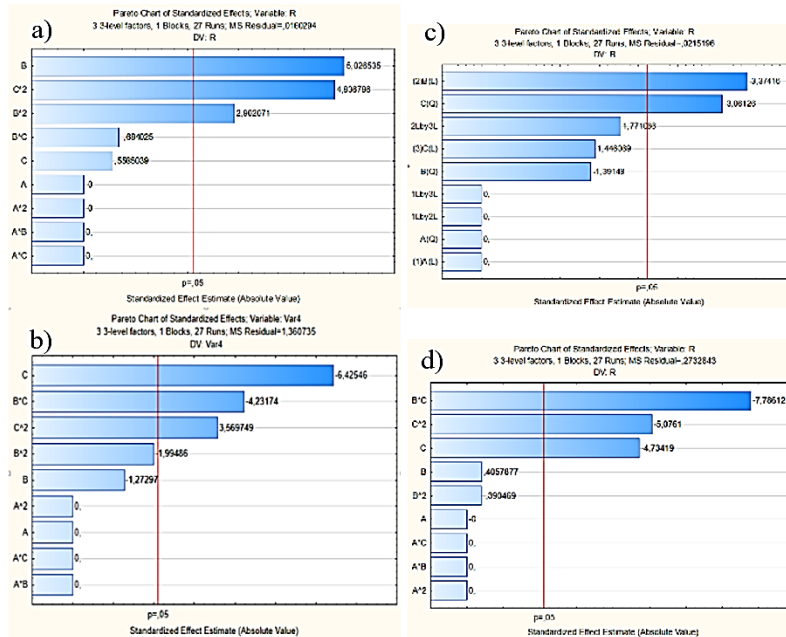
Figure S1A Pareto Chart of Standardized Effects for the 3^3 factorial model of the four compounds: a AFNQ; b ACNQ; c ABNQ and d AINQ.

S2. ANOVA Analysis

Table S2A ANOVA values for the 3^3 factorial model of four compounds.

	AFNQ						**ACNQ**				
Factor	*SS*	*df*	*MS*	*F*	*p*	*Factor*	*SS*	*Df*	*MS*	*F*	*P*
A	0.00	1	0.00	0.00	1.00	A	0.00	1	0.00	0.00	1.00
A^2	0.00	1	0.00	0.00	1.00	A^2	0.00	1	0.00	0.00	1.00
B	0.40	1	0.40	25.26	0.00	B	0.24	1	0.24	11.38	0.01
B^2	0.13	1	0.13	8.42	0.01	B^2	0.04	1	0.04	1.93	0.18
C	0.01	1	0.01	0.31	0.58	C	0.04	1	0.04	2.09	0.16
C^2	0.37	1	0.37	23.39	0.00	C^2	0.20	1	0.20	9.37	0.01
A*B	0.00	1	0.00	0.00	1.00	A*B	0.00	1	0.00	0.00	1.00
A*C	0.00	1	0.00	0.00	1.00	A*C	0.00	1	0.00	0.00	1.00
B*C	0.01	1	0.01	0.46	0.50	B*C	0.06	1	0.06	3.13	0.09
Error	0.27	17	0.01			Error	0.36	17	0.02		
Total SS	1.20	26				Total SS	0.96	26			
	ABNQ						**AINQ**				
Factor	*SS*	*df*	*MS*	*F*	*p*	*Factor*	*SS*	*Df*	*MS*	*F*	*P*
A	0.00	1	0.00	0.00	1.00	A	0.00	1	0.00	0.00	1.00
A^2	0.00	1	0.00	0.00	1.00	A^2	0.00	1	0.00	0.00	1.00
B	2.20	1	2.20	1.62	0.22	B	0.04	1	0.04	0.16	0.68
B^2	5.41	1	5.41	3.97	0.06	B^2	0.04	1	0.04	0.15	0.70
C	56.18	1	56.18	41.28	0.00	C	6.12	1	6.12	22.41	0.00
C^2	17.34	1	17.34	12.74	0.00	C^2	7.04	1	7.04	25.76	0.00
A*B	0.00	1	0.00	0.00	1.00	A*B	0.00	1	0.00	0.00	1.00
A*C	0.00	1	0.00	0.00	1.00	A*C	0.00	1	0.00	0.00	1.00
B*C	24.36	1	24.36	17.90	0.00	B*C	16.56	1	16.56	60.62	0.00
Error	23.13	17	1.36			Error	4.64	17	0.27		
Total SS	128.64	26				Total SS	34.46	26			

ARTIGO 4 PROBING KINETIC AND THERMODYNAMIC PARAMETERS AS WELL AS SOLVENT AND SUBSTITUENT EFFECTS ON SPECTROSCOPIC PROBES OF 2-AMINO-1,4-NAPHTHOQUINONE DERIVATIVES.

Probing kinetic and thermodynamic parameters as well as solvent and substituent effects on spectroscopic probes of 2-amino-1,4-naphthoquinone derivatives

Abstract

In the world, many diseases, such as cancer, require rapid diagnosis. Currently, it is well known that fluorescent spectroscopy is one of the most promising methodologies to this end, because it is less invasive, rapid and quite sensitive. In this perspective, naphthoquinone derivatives have demonstrated applications as fluorescent probes. Despite great importance of substituents effects on the fluorescence mechanism, such as the ESIPT process, few detailed computational works on this subject have appeared. Our current findings showed that the ESIPT process is a preferential fluorescence mechanism in a great number of molecules. The compounds showed color emission ranging from red to green and blue to violet. Furthermore, PCA techniques have been employed for rationalizing the energy gaps of the fluorescence process of 36 naphthoquinone (ANQ) derivatives. The PCA referent emission energy showed bathochromic effects when electron donor groups were at position R_3 or R_5 and hypsochromic effects when withdrawing groups were in the same position. Our findings point out that substituents with higher electron density promote wavelength red-shifting. In fact, the substituent effects provide an understanding about behavior of the ESIPT process in ANQ derivatives, and how kinetic and thermodynamic parameters can be influenced. These conclusions can help in understanding emission and absorption energies as well as the solvent and substituent influence on the spectroscopic parameters.
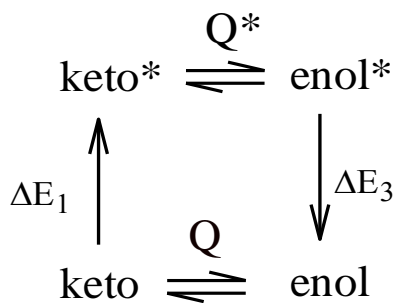
1. Introduction

Currently, fluorescent spectroscopy plays an important role for rapid and sensitive diagnosis of many diseases including cancer [1,2]. In fact, various compounds have been used as probes for pathology and biomolecule detection [3]. Cancer detection employing fluorescent probes *in vivo* and *in vitro* was reported in 1990 [4] and the probe applications have demonstrated to be crucial for an efficient treatment, faster diagnosis and cure [5,6]. In this sense, the literature has reported applications of naphthoquinones as fluorescent probes in breast cancer detection in humans [6,7].

In fact, different mechanisms can be cited for explaining the fluorescent emission in naphthoquinones [8]. The excited-state intramolecular proton transfer (ESIPT), which is a photo induced proton transfer across an intramolecular hydrogen bond, was reported as one possible mechanism [9–11]. The fluorescent emission in this mechanism, which is dependent on the chemical environment [9], involves the hydrogen transfer in excited-state and subsequent decay from ground state [12].

Recently, in a previous contribution, we illustrated the solvent influence on the ESPIT process, in which we demonstrated that this process occurs more favorably in non-polar solvent (like chloroform), however in polar solvent (like water) the ESIPT process can also occur [10]. Despite the great importance of developing spectroscopic probes for disease diagnosis, surprisingly little detailed computational work investigating thermodynamic and kinetic parameters of these compounds in solution has appeared [13–16]. In fact, the thermodynamic and kinetic parameters can help in streamlining the action mechanism of drug and spectroscopic probes, as they provide important information about chemical bonds, chemical interactions and energies involved as well as the reaction speed of these compounds in organisms [17,18]. Therefore, kinetic study provides

relevant information about the process and how structural modifications can affect the proton transfer rate in ANQ derivatives [19].

$$\text{keto*} \underset{}{\overset{Q^*}{\rightleftharpoons}} \text{enol*}$$

$$\Delta E_1 \uparrow \qquad \qquad \downarrow \Delta E_3$$

$$\text{keto} \underset{}{\overset{Q}{\rightleftharpoons}} \text{enol}$$

Fig. 1 Thermodynamics cycle of keto and enol form excitation during proton transfer. From the thermodynamic cycle in this figure, the equilibrium constant was calculated through Eqs. 1 and 2 in the ground and excited state [20]. When Q and Q* was equilibrium constant in ground and excited-state, respectively.

The estimated Gibbs free energy in the ground and excited-states (Equation 2) provides significant information for the transition state formation of the ESIPT process [21]. The Thermodynamic cycle described in Figure 1 was employed for calculating the Gibbs free energy in excited-state [20]. It is well-known that the Gibbs free energy calculation in the excited-state employs the formalism described by Equations 1, 2 and 3 [20,22,23]. The Gibbs free energy in the ground state as well as the difference between the absorption energy for the keto form and the emission energy from Enol form were used for calculating pK* values by Equation 1 and Figure 1. The molecular geometries in the excited state followed the Franck-Condon principle [20,22–26].

Equation 1:

$$pK = pK^* + \frac{(\Delta E_3 - \Delta E_1)}{RTln10}$$

Equation 2:

$$pK^* = -logQ^*$$

Equation 3:

$$\Delta G^* = -RTlnQ^*$$

The constant rate is dependent on many factors, such as electronic, steric and structural interactions [27]. The constant rate (k) can be calculated by the Eyring-Polanyi equation (Equation 4), where h is the Plank's constant, k_B is the Boltzmann's constant, R is the universal gas constant, $\Delta G^{\#}$ is transition state Gibbs free energy and T is the temperature [28]. These parameters can successfully be obtained by structure electronic calculations, for instance DFT or *ab initio* methods.

Equation 4:

$$k = \frac{k_B T}{h} exp\left(-\frac{\Delta G^{\#}}{RT}\right)$$

In recent years, the application of Density Functional Theory (DFT) for studying spectroscopic properties of biological molecules has grown, because DFT calculations can be successfully employed for macro or microsystems [29]. For instance, Mariam et. al. [30,31] investigated the intramolecular hydrogen bond interactions of naphthoquinones with enzymes by DFT calculations, whereas Lamourex et. al. [32] reported the structure and reactivity studies of naphthoquinone derivatives employing the DFT method. Besides the DFT method, the excited state naphthoquinones were characterized employing Time Dependent Density Functional Theory (TD-DFT) [33] and their absorption and emission energies were calculated [8,10,11,34]. DFT and TD-DFT methodologies were employed for kinetic studies, because these methodologies have been used successfully for exploring the elementary steps and mechanisms, besides spectroscopic and thermodynamics properties [35]. Azarias et. al. [12] investigated the substituent effects in hydroxyphenyl-benzoxazole (HBO), -

benzimidazole (HBI) and [3H]-indole (HI) whereupon changing the positions R_1, R_2, R_3 and R_4 in the structure of these compounds and making the relation with emission values in the ESIPT process available. In addition, we have observed the relation between thermodynamics parameters and a keto, enol and dual emission of fluorescence [12].

The structural changes in naphthoquinones affect their fluorescent properties [36]. Thus, the evaluation of this influence is very important for applications in biological systems [37]. The structural modification of the benzenoid or quinoid ring in naphthoquinones change the spectroscopic properties in different ways [38–40]. For example, the absorption affects much more when the substitution occurs in the quinoid ring, as well as the benzenoid ring, according to Jacquemin et. al. [41]. Despite their great importance, studies involving the influence of the substituent effect on the ESIPT process in naphthoquinones have been little investigate in the literature [32,42,43]. Lan X. et. al. demonstrated, for 2-hydroxybenzoil, that the ESIPT process does not occur when electron withdrawn substituents are added in the benzoyl structure [42]. On the other hand, Barman et. al. described the ESIPT process across the *o*-hydroxybenzothiazole group [44]. They related the emission change during 15 min of experiment with the structural alteration of the fluorescent probe [44]. In this sense, understanding this influence is crucial for developing new fluorescent probes with different emission wavelengths, more sensitive, faster and more precise for applications in disease diagnosis [45,46].

In this line, this paper related kinetic and thermodynamics studies in the proton transfer in the excited-state for 2-amino-1,4-naphthoquinone and its derivatives, as well as evaluated the substitution and solvent effects on the ESIPT process. These studies were carried out at the TD-DFT level for characterization of the excited states, the absorption calculation, proton transfer and emission energy of all compounds. PCA analysis was employed for discrimination among

participants involved in the proton transfer process across the relation between the ESIPT energies and the compounds structures.

2. Calculation Strategy

2.1 Ground State Calculations

All ANQ derivatives (keto and enol form) have been optimized (10^{-5} a.u. for self-consistent field) at the DFT level with DGTZVP basis set and B3LYP functional, which was the best functional for investigating structural and electronic aspects for this class of compounds according to previous studies [10,47]. The vibrational frequencies were obtained with DFT in gas phase and solvent effects were evaluated by the COSMO model [48–50]. From the vibrational frequencies, the thermochemistry parameters for all compounds were determined and used for calculating the transition state Gibbs free energy ($\Delta G^{\#}$) as well as the Gibbs free energy (ΔG) values for the ground state. From the $\Delta G^{\#}$ and ΔG values, pK and pK$^{\#}$ parameters were also obtained from Equation 1.

2.2 Excited State Calculations

The TD-DFT calculations were carried out at the CAM-B3lYP/DGTZVP level. From previous works, the CAM-B3LYP functional was identified as an important the best functional for the electronic properties of this class of compounds [10,47,51]. The CAM-B3LYP functional exhibit a long-range behavior and description for excited-state with significant through-space charge transfer [51]. Here, we have applied TD-DFT calculations to determine the vertical and adiabatic transition energies of 20 excited states for Keto and Enol forms of ANQ derivatives. In all compounds, the absorption energy (ΔE_1) was calculated for the Keto form and the emission energy (ΔE_3) was calculated for the Enol form according Figure 3. The ΔE_1 and ΔE_3 values were employed for calculating pK* in Equation 1. Afterwards, the pK* value was used for obtaining

Q* using Equation 2 and the excited-state Gibbs free energy (ΔG*) according to Equation 3. The proton transfer energy (ΔE_2) was determined by difference between ΔE_3 and ΔE_1, as displayed in Figure 3.

2.3 Solvent Effect, Potential Energy Surface and PCA analysis

To account for solvent effects from water, optimized structures, vibration frequencies, thermochemistry and transition energies were obtained using the conductor-like screening model (COSMO) implemented in the ORCA program [52]. In fact, all calculations were performed in the program. The ESIPT process was investigated determining the absorption energy (ΔE_1), the proton transfer energy (ΔE_2) and the emission-energy (ΔE_3), in gas phase and water solvent, according to the scheme in Figure 3. The Chemcraft program was employed for visualization of compounds [53].

The potential energy surface was carried out transferring the proton from the nitrogen of amine to oxygen atom of the keto group forming the tautomeric species, enol. The approximation was automatic and the displacement step was 0.25 Å in direction of the keto group. In each step, the ground and excited-state energies were calculated employing the DFT/DGTZVP/B3LYP and TDDFT/DGTZVP/CAM-B3LYP, respectively. The transition state was characterized using the imaginary vibrational frequencies [31,54].

For testing the similarity among 31 compounds investigated, the energy gaps (ΔE_1, ΔE_2 and ΔE_3) involved in the ESIPT process were applied to PCA analysis [55,56]. The values obtained in gas phase and water solvent were used for the PCA analysis in Figure 5. Herein, we divided the energies into three PCA graphs with absorption energy (ΔE_1), proton transfer energy (ΔE_2) and emission energy information (ΔE_3). Principal Component Analysis (PCA) was performed using the Statistica® program [57,58].

3. Results and Discussion

3.1. *Kinetic and thermodynamic parameters for the reaction mechanism of the proton transfer in 2-amino-1,4-naphthoquinone derivatives .*

In Figure 2, the Potential Energy Surface (PES) for ANQ compounds showed that the keto form was more stable than the enol form in ground state, it should be kept in mind, however, that the enol form can be more stable than the keto form in excited-states.
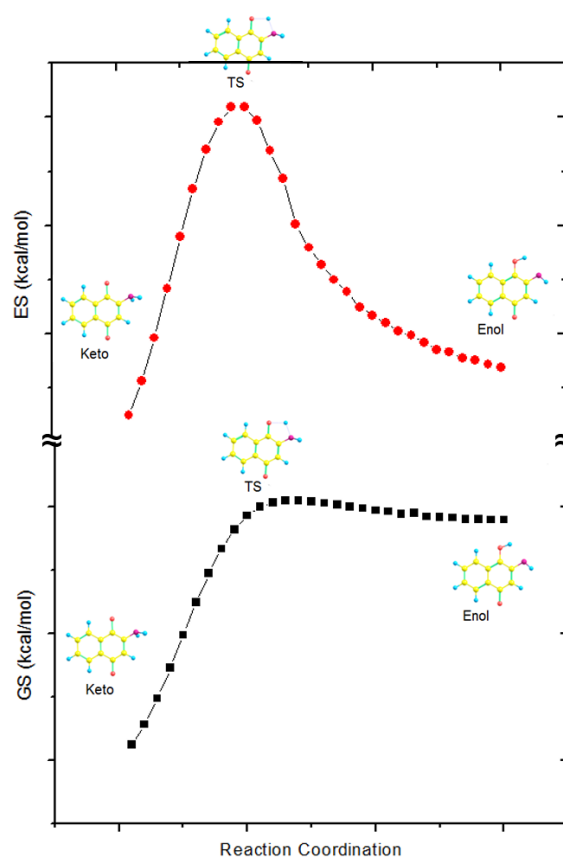
Fig 2. Intrinsic Coordinate Reaction (IRC) for 2-amino-1,4-naphthoquinone in ground (black) and excited-state (red). Results obtained for variance a bond lengths N – H – O during proton transfer in ESIPT process.

The transition state structures were characterized in ground and excited-state and the keto, TS and enol structures from ANQ compounds were obtained from the PES (figure 2). The keto form revealed bond lengths of 1.04 Å and 1.04 Å related to of N – H and O – H, respectively. For the TS form, the bond lengths of 1.36 Å and 1.38 Å are related to N – H and O – H, while and the enol form 2.24 Å and 1.00 Å are associated to the N – H and O – H bond lengths, respectively. The distances between N – H and O – H chemical bonds during the proton transfer are reported in Table 1. All points in the PES for the N – H and O – H chemical bonds in the ground and excited state are reported in the Supplementary material Table S2 and S4.

Table 1 - Distance values in angstroms (Å) and angle value between N – H and O – H, during the proton transfer for construction of the Potential Energy Surface of Figure 2.

Compounds	d(N – H)	d(O – H)	α(N – H – O)
K	1.04	1.82	122.79
K*	1.04	1.82	122.79
TS	1.36	1.38	136.51
TS*	1.36	1.38	136.51
E	2.24	1.00	115.59
E*	2.25	1.00	115.59

Eight 2-amino-1,4-naphthoquinone derivatives (Figure 3) were used for exploring kinetic and thermodynamics properties. The transition state formed a five-member ring with hydrogen between oxygen and nitrogen. The initial step is the keto form of the 2-amino-1,4-naphthoquinone and the final step is the enol form, after the ESIPT process. The calculated frequencies for three steps in the ground and excited state were carried out to characterize the transition state structures. For three compounds, thermodynamics as well as kinect parameters were calculated. The thermodynamics parameters ΔG and $\Delta G*$ are defined as the difference between final and initial step in the ground and excited state,

respectively. Turning now to the kinetic parameters, $\Delta G^{\#}$ and $\Delta G^{*\#}$ are defined as the difference between transition state and initial step for the ground and excited state, respectively. In addition, the rate constants k and k^{*}, from Equation 4, were calculated from the ΔG and $\Delta G^{\#}$ values, respectively. In Equation 1, the difference between the emission energy (ΔE_3) and absorption energy (ΔE_1) was calculated from the final and initial step, respectively. These values are used in Equation 1 to calculate the pK* and $pK^{\#}$* parameters. From Equation 2, the Q* and $Q^{\#}$* values are obtained and from Equation 3, ΔG^* and $\Delta G^{*\#}$ values. Turning now to the rate constant in excited state (k*), which was calculated using the $\Delta G^{*\#}$ values in Equation 4. All Gibbs free energy values and rate constants are in Table 2. It is worth mentioning that other thermodynamics parameters, such as ΔH, ΔS and ΔE $\Delta H^{\#}$, $\Delta S^{\#}$ and $\Delta E^{\#}$, are shown in supplementary material.
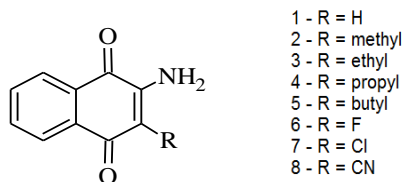
Fig. 3. Structure of 2-amino-1,4-naphthoquinone derivatives exhibiting all compounds in the mechanistic pathway.

Regarding the activation Gibbs free energy ($\Delta G^{\#}$) for Compound *1*, the value was 37.54 kcal/mol in the ground state and 24.35 kcal/mol in the excited-state. On the hand, Compound *2* was 76.30 and 58.99 kcal/mol, while Compound *3* was 76.30 and 58.99 kcal/mol, Compound *4* was 68.83 and 42.02 kcal/mol, Compound *5* was 78.85 and 64.73 kcal/mol, Compound *6* exhibits 39.85 and 21.04 kcal/mol, Compound *7* was 36.00 and 19.00 kcal/mol and Compound *8* was 54.24 and 17.98 kcal/mol, respectively. The $\Delta G^{\#}$ and $\Delta G^{*\#}$ parameters are according to transition-state theory, because the values were positive for all

compounds. Although the $\Delta G^{*\#}$ values are positive, they are lower than in the ground state ($\Delta G^{\#}$ values), so that this process in the excited-state is more favorable. Compound *8* exhibits the lowest $\Delta G^{\#*}$ value among the studied compounds.

Table 2 - Kinetic and thermodynamic parameters (kcal/mol) for transition state and final stage of proton transfer of naphthoquinones derivative.

	Kinetic				Thermodynamic	
	$\Delta G^{\#}$	k	$\Delta G^{\#*}$	k*	ΔG	ΔG^*
1	37.54	6.07E+12	24.35	5.97E+12	11.82	-14.38
2	76.30	5.69E+12	58.99	5.63E+12	12.77	-18.92
3	66.99	5.78E+12	45.85	5.76E+12	11.75	6.31
4	68.83	5.76E+12	42.02	5.79E+12	10.72	0.31
5	79.85	5.67E+12	64.73	5.58E+12	11.87	11.83
6	39.85	6.05E+12	21.04	6.00E+12	13.96	-18.24
7	36.00	6.47E+12	19.00	6.49E+12	11.91	3.58
8	54.24	5.91E+12	17.98	6.03E+12	23.15	34.00

[#]Values in the transition state; *Values in the excited-state; k is the rate constant.

Furthermore, the ΔG and ΔG^* values suggest that the process does not spontaneously occur in the ground state, whose ΔG values range from 10.72 kcal/mol to 13.96 kcal/mol. In the excited-state, however, Compound *1* showed -14.38 kcal/mol, Compound *2* -18.92 kcal/mol and Compound *6* showed -18.24 kcal/mol, which are spontaneous. Thus, Compounds *1*, *2*, *6* were thermodynamically favorable. Compound *3* showed 6.31 kcal/mol, Compound *4* 0.31 kcal/mol, while Compound *5* was of 11.83 kcal/mol. Compound *7* showed 3.58 kcal/mol, while Compound *8* 34.00 kcal/mol, obtained the highest ΔG^* value among all studied compounds. Thus, Compounds *3*, *4*, *5*, *7* and *8* were thermodynamically unfavorable.

The rate constant in the ground state reveals that Compound *7* was the most reactive among all compounds, followed by *1*, *6*, *8*, *3*, *4*, *2* and *5*. In the

excited-state, the most reactive compound was *7* as well, followed by Compounds *8*, *6*, *1*, *4*, *3*, *2* and *5*. The values indicate an order of reactivity in the excited and ground state, suggesting that Compound *7* is kinetic and thermodynamically favorable. Although Compounds *3*, *4*, *5* and *7* are not thermodynamically favorable, they showed to be kinetically favorable in excited-states.

3.2. *Spectroscopic properties of the 2-amino-1.4-naphthoquinone derivatives.*

The interest in amino-naphthoquinone derivatives (ANQ) is associated to their application as fluorescent probes in biological systems [5,58]. Therefore assessing the solvent effect on the ESIPT process for ANQ derivatives is a very important task for simulating the application of spectroscopic probes in biological environments. In this line, the solvent effect was taken into account with the COSMO continuum solvation model [48,59] for all compounds. The ESIPT process described in Figure 4 shows the absorption energy (ΔE_1), in which the keto form was excited. In the excited-state, the proton transfer forms the enol form. The proton transfer energy (ΔE_2) is the energy involved in the tautomeric mechanism. The emission energy (ΔE_3) is the enol form decay from excited state to ground state. The energy values shown in Table 2 were calculated in gas phase and water solvent.

The kinetic and thermodynamic studies showed that the ESIPT process is favorable for the proton transfer in 2-amino-1.4-naphthoquinone (*1*) derivatives. Compound *1* exhibits an absorption energy of 4.65 eV (Table 3), whereas the hydrocarbon derivatives were 4.44, 4.17, 3.96 and 4.42 eV for the *2*, *3*, *4* and *5* derivatives, respectively. The values were lower than those for Compound *1*. The same effects were observed in Compounds *6* and *7*, which exhibited 4.42 and 4.01, respectively.
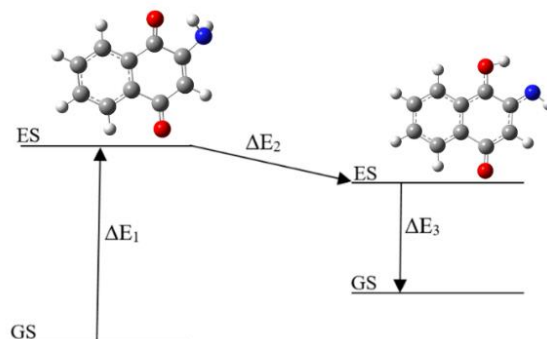
Fig. 4 – Diagram of ESIPT process of the 2-amino-3-butyl-1.4-naphthoquinone with absorption energy ΔE_1 between ground state (GS) and excited state (ES) from Keto form. Proton transfer energy ΔE_2 between Keto-Enol forms in ES and emission energy ΔE_3 between ES and GS from Enol form.

Compound **8** exhibit 4.04 eV for absorption energy in gas phase. The proton transfer ΔE_2 for Compound **1** was -1.33 eV (Table 2), this value was negative because the Enol form showed lower energy value than the Keto form and the difference in the Enol-Keto energy was negative, which was required for the ESIPT process to occur. Compound **2** was -1.08 eV, for **3** it was -0.83 eV, for **4** -0.65 and for **5** the energy was -1.11 eV. The hydrocarbon derivatives showed the ESIPT transfer for all compounds. Compound **6** (fluorine derivative) was -1.06 eV and Compound **7** (Chlorine present) was -0.80 eV. The halogenated compounds also exhibit an ESIPT process, but the proton transfer values are lower when compared to Compound **1**. Compound **8** showed a proton transfer value of -0.08 eV, which suggests that the ESIPT process cannot be occurring in gas phase.

The emission energy (ΔE_3, Table 3) for Compound **1** was 2.74 eV, emission at 452 nm (blue region). The Hydrocarbon derivatives **2**, **3**, **4** and **5** showed 2.78, 2.80, 2.77 and 2.77 eV, respectively, which emitted at 445, 442 and 447 nm, respectively. The values suggest that the hydrocarbon derivatives influenced the emission energy, displaying a lower hypsochromic effect compared to **1**. Compounds **6** and **7** also showed 2.74 and 2.78 eV, respectively, which

emitted at 452 nm and 445 nm. Compound *8* showed 2.95 eV for the emission energy, emitting a violet color at 420 nm.

Turning now to the solvent effects, Compound *1* showed an absorption energy, ΔE_1, in water, of 4.55 eV (Table 3) while the hydrocarbon substituents showed lower absorption energy values. Compound *2* showed a ΔE_1 of 4.47 eV, Compound *3* was 4.25 eV, and Compounds *4* and *5* were 4.17 eV each. Finally, Compounds *6* and *7* were 4.48 and 4.25 eV, respectively. The proton transfer energy (ΔE_2) was -1.81 eV for ANQ, which demonstrates that the ESIPT process occurs in water solvent. The same way, the hydrocarbon substituents pointed to negative values for the ΔE_2. The Compound *2* derivative was - 0.94 eV in water solvent, a lower value compared to gas phase. Compound *3* was - 1.33 eV in water solvent, a higher energy value in gas phase, Compound *4* was - 0.67 eV, which was the same value in gas phase. On the other hand, Compound *5* was - 0.78 eV, a lower value when compared to gas phase. The halogen substituents showed proton transfer energy values that were more negative in water than in gas phase. Compound *6* was -1.61 eV and Compound *7* was -1.07 eV for the proton transfer energy (ΔE_2). Compound *8* showed ΔE_2 -0.30 eV, this value suggests that ESIPT process can occur in water solvent.

In water, the emission energy for Compound *1* was -2.17 eV, emitting a green color, which is a lower energy value than in gas phase. The hydrocarbon substituents showed higher emission energies compared to gas phase. Compounds *2* and *3* in water solvent were 2.89 eV for each, Compound *4* was 2.87 eV and Compound *5* showed the same value in the gas phase and water 2.77 eV. Compound *6* emission energy ΔE_3 was 2.83 eV, emitting a violet color, while Compound *7* was 2.66 eV, emitting a blue color.

Table 3 - Reference energy values (eV) for the ESIPT process presenting the absorption energy (ΔE_1), proton transfer energy (ΔE_2) and emission energy (ΔE_3).
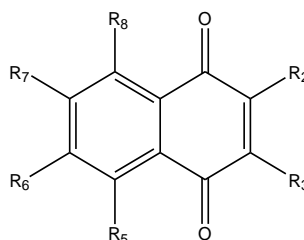
	Position						Gas Phase			Water		
	R_2	R_3	R_5	R_6	R_7	R_8	ΔE_1	ΔE_2	ΔE_3	ΔE_1	ΔE_2	ΔE_3
1	NH_2	H	H	H	H	H	4.65	-1.33	2.74	4.55	-1.81	2.17
2	NH_2	CH_3	H	H	H	H	4.44	-1.08	2.78	4.47	-0.94	2.89
3	NH_2	CH_2CH_3	H	H	H	H	4.17	-0.83	2.80	4.25	-1.33	2.89
4	NH_2	$(CH_2)_2CH_3$	H	H	H	H	3.96	-0.65	2.77	4.17	-0.67	2.87
5	NH_2	$(CH_2)_3CH_3$	H	H	H	H	4.42	-1.11	2.77	4.17	-0.78	2.77
6	NH_2	F	H	H	H	H	4.42	-1.06	2.74	4.48	-1.61	2.83
7	NH_2	Cl	H	H	H	H	4.01	-0.80	2.66	4.25	-1.07	2.66
8	NH_2	CN	H	H	H	H	4.04	-0.08	2.95	3.88	-0.30	2.71
9	NH_2	NH_2	H	H	H	H	4.60	-1.24	2.97	4.51	-1.31	2.77
10	NH_2	OCH_3	OCH_3	H	H	OCH_3	5.93	2.96	1.93	5.84	3.47	2.43
11	NH_2	H	H	H	H	NH_2	4.67	-1.65	2.44	4.58	-1.57	2.77
12	$NHCH_3$	CN	NH_2	H	H	H	4.45	-1.52	1.85	4.29	-1.63	1.95
13	$NHCH_3$	H	NH_2	H	H	H	4.63	-2.34	1.73	4.55	-1.80	1.62
14	$NHCH_3$	H	NO_2	H	H	H	1.49	-1.75	1.60	4.74	-3.25	3.25
15	$NHCH_3$	H	H	H	H	H	4.67	-0.40	3.04	4.57	-0.90	2.86
16	$NHCH_3$	Cl	H	H	H	H	4.41	-3.09	1.79	4.26	-0.64	2.91
17	$NHCH_3$	Cl	OCH_3	H	H	OCH_3	4.41	-3.21	2.72	4.09	-0.93	2.44
18	$NHCH_3$	Cl	NH_2	H	H	H	4.46	-3.60	1.87	4.31	-2.24	1.76
19	$NHCH_3$	Cl	NO_2	H	H	H	3.74	-1.25	3.00	3.59	-0.42	2.55
20	$NHCH_3$	CN	H	H	H	H	4.39	-0.25	2.99	4.38	-1.02	2.73
21	$NHCH_3$	CN	NH_2	H	H	H	4.43	-1.04	2.59	4.40	-0.97	2.75
22	$NHCH_3$	$NHCH_3$	H	H	H	H	4.56	-0.32	2.91	4.48	0.04	2.94
23	$NHCH_3$	NHPh	H	H	H	H	4.50	-3.50	2.60	4.38	-2.84	2.56
24	$NHCH_3$	OCH_3	H	H	H	H	4.56	-0.53	1.68	4.46	1.42	2.97
25	$NHCH_3$	OCH_3	NH_2	H	H	H	4.60	-0.97	1.68	4.49	0.97	2.84
26	$NHCH_3$	H	OCH_3	Cl	Cl	OCH_3	4.67	-5.45	2.47	4.59	-1.51	2.26
27	NHPh	H	H	H	H	H	4.65	-1.38	2.29	4.57	-1.63	2.06
28	NHPh	Cl	H	H	H	H	4.43	-1.88	2.21	4.31	0.36	2.18
29	NHPh	CN	H	H	H	H	4.48	-0.82	1.82	4.42	-0.19	2.19
30	NHPh	OCH_3	H	H	H	H	4.06	-2.42	2.18	3.91	-0.54	2.98
31	$NHCH_3$	OCH_3	NH_2	H	H	H	3.95	-1.74	1.72	3.88	-0.31	2.91
32	$NHSO_2Ph$	$NHPh-3.5-(CH_3)_2$	H	H	H	H	3.69	-3.57	2.06	3.43	-2.90	2.10
33	$NHCH_2(CH_3)_2$	H	H	H	H	H	4.62	-0.25	2.95	4.47	-0.40	2.76
34	$NHCH_3$	NO_2	H	H	H	H	4.72	-0.51	3.09	4.66	-1.25	2.46
35	$NHCH_2C_5H_4N$	H	H	H	H	H	4.86	-0.58	2.85	4.72	-0.76	2.59
36	NH_2	NO_2	H	H	H	H	4.78	-0.43	3.05	4.63	-0.62	2.87

Compound *8* emitted at 2.71 eV (blue color region). The emission ranges of green, blue or violet color when the substituents in Compound *1* were added exhibit the hypsochromic shift. The other compounds were used to understand

how substituents and their positions in the naphthoquinone structure alter the ΔE_1, ΔE_2 and ΔE_3 values in water and gas phase.

3.3. PCA analysis: Influence of position and substituent on the ESIPT process in 2-amino-1.4-naphthoquinones derivatives.

To rationalize the substituent effect on the ESIPT process of spectroscopic probes, other compounds structurally modified at Position 2 were taken into account. Thus, we have introduced different substituents into the chemical structure of 1.4-naphthoquinone (Fig. 5) in order to evaluate the barrier energies in the ESIPT process (Table 3). In addition, the chemiometric methodology (PCA analysis) was applied to investigate how position and substituent influenced the ESIPT process and what their influence is on the energy absorption, emission and proton transfer.


Fig. 5 - Chemical Structure for derivatives for 1.4-naphthoquinone and the positions that were altered (R_2. R_3. R_5. R_6. R_7 and R_8).

The PCA analysis (Fig 6) was carried out for each energy gap in gas phase and in solution. Graph A exhibits the Factor 1 and 2 generated for ΔE_1, Graph B for ΔE_2 and Graph C for ΔE_3. Graph A (Fig. 6A) showed only two nonstandard compounds, but the other compounds were grouped in the PCA center, which exhibits values around 4.50 eV in both water and gas. Compound *10* was an outlier in relation to ΔE_1 energy, being the highest value for this energy (5.93 eV in gas

phase and 5.84 eV in water). Compound *14* exhibits 1.49 eV in gas phase, also being an outlier. Graph B (Fig 6B) showed four groups and two outlier compounds in relation to ΔE_2. Compound *10* showed positive values for the ΔE_2 energy and no ESIPT process in gas phase and water. Compound *26* exhibits a ΔE_2 value of - 5.45 eV in gas phase and in water of - 1.51 eV. The group formed by Compounds *24*, *25* and *28* do not exhibit an ESIPT process, because they present positive ΔE_2 values in both solution and gas phase. Compounds *24* and *25* showed the group methylamine as well as the methoxide group at the R_3 position, resulting in much more hydrophobic characteristics for the molecules, which is a disadvantage for the ESIPT process in water. The group formed with Compounds *4*, *5*, *16*, *17*, *19*, *22*, *29*, *30* and *31* exhibit ΔE_2 values between 0.00 and - 1.00 eV. These compounds showed electrons withdrawing substituents, such as methoxide (OCH_3) and cyanide (CN) groups. Compounds *8*, *14*, *18* and *23* formed a group with higher ΔE_2 values, - 2.00 eV. These compounds showed electron donor substituents, such as chlorine (Cl) and amino derivatives or $NHCH_3$. The other compounds formed a new group with ΔE_2 values ranging from -1.00 to 2.00 eV. Substituents at the R_8 position help stabilize the positive charge in the resonance and the stabilization promotes the ESIPT process with values between - 1.00 and - 2.00 eV.

Graph C (Fig. 6C) showed four groups formed for compounds that have the same wavelength or emission energy. The ΔE_3 values for the group formed from Compounds *12*, *13* and *18* were 1.95, 1.62 and 1.76 eV, emitting a red color in water, respectively. These compounds showed electron donor groups at Positions R_3 or R_5. The group formed by Compounds *1*, *10*, *26*, *27*, *28* and *29* emitted a green color and the ΔE_3 values were 2.17, 2.43, 2.26, 2.06, 2.18 and 2.19 eV, respectively. Although Compounds *10* and *28* do not exhibit an ESIPT process, their ΔE_3 values were similar to those of the other compounds and the PCA captured this information.
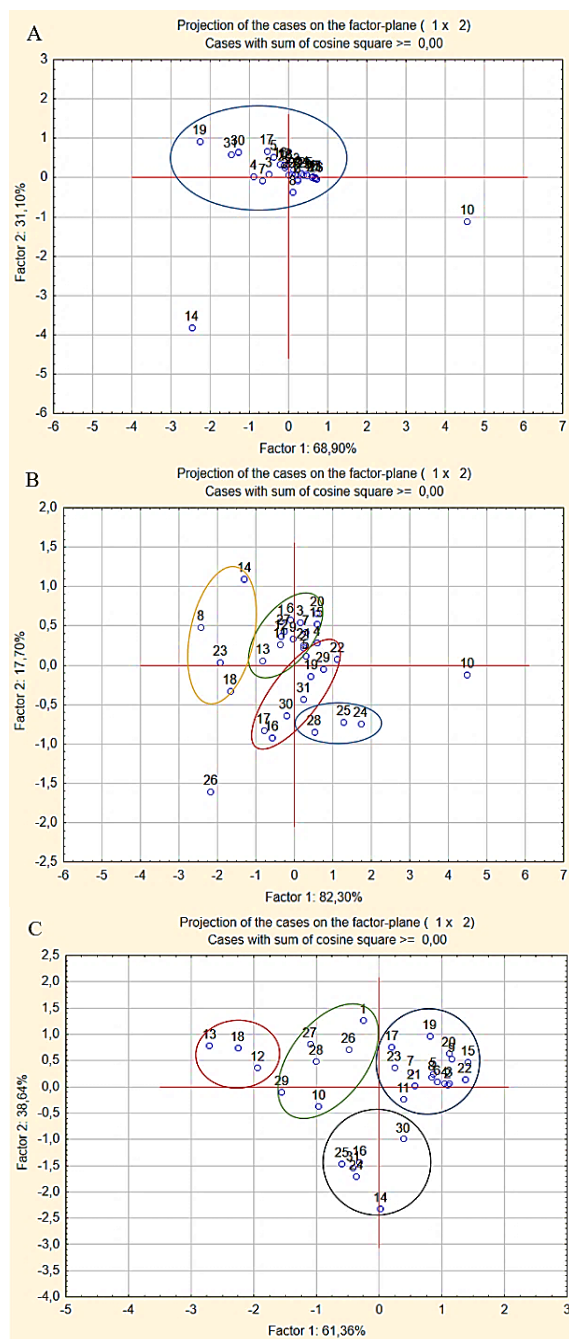
Fig. 6 – PCA graph showing the Factor 1 and 2 for the energy values: A) ΔE_1 energy; B) ΔE_2 energy and C) ΔE_3 energy.

The group formed by Compounds *14*, *16*, *24*, *25*, *30* and *31* exhibit large differences in ΔE_3 values when compared to values in gas phase and water. For example, Compounds *14* and *16* in gas phase showed values 1.60 and 1.79 and in water higher values of 3.25 and 2.91 eV, respectively. The other compounds, including this group, emitted a blue color and their values were higher, 2.50 eV. Comparatively, the compounds of these groups showed electron withdrawing groups at position R_3 or R_5. Graph C indicated that when the rich electron density groups were at Position R_3 or R_5, the ΔE_3 values exhibit bathochromic effects and when the withdrawing groups were at Position R_3 or R_5, the ΔE_3 values exhibit hypsochromic effects. In line with our theoretical findings, substituent groups are not able to simultaneously optimize all energy gaps involved in the ESIPT for ANQ derivatives, but the substituent effect significantly affects ΔE_3 values.
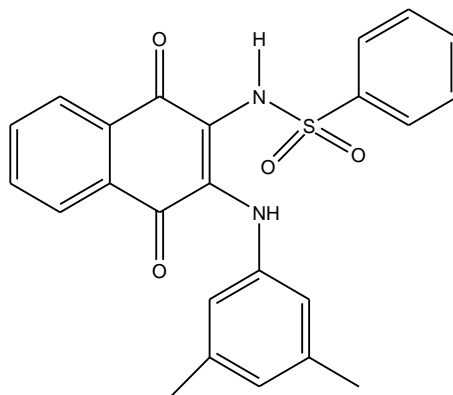
Fig 7 – Naphthoquinone derivative structure of Compound *32* used with fluorescent probe in the enzyme N-acetyltransferase.

In order to validate the theoretical techniques and the efficiency of the PCA methodology for describing the behavior of all tested compounds, we have used Compounds *32, 33, 34* and *35*. It is important to mention that Compound *32* (fig. 7) is a fluorescence probe even for N-acetyl Transferase enzymes [3,6],

which has previously reported experimental emission values. In fact, Compound *32,* contains two substituents with higher electron density in the amino group (R_2) and R_3 position and exhibits an emission experimental wavelength of 585 nm (2.11 eV) [3–6.57], which corresponds to a red color. The emission wavelength values calculated for this compound, according to the experimental value, showed an error of -0.05 eV in gas phase and -0.01 eV in water (Table 3). The other four compounds (Fig. 8) had their energy values (ΔE_1. ΔE_2 and ΔE_3) calculated in gas phase and water solution as well. These values were compared to the experimental values [46,61] for estimating the error and efficiency of the theoretical methodology employed in the study. Compound *33* showed an experimental value of 4.54 eV for the absorption energy, while the theoretical value was 4.48 eV, revealing a difference between theory and experiment of about 0.06 eV. On the other hand, Compound *34* shows an experimental value of 4.95 eV and an error, compared to the theoretical value (4.66 eV), of 0.29 eV.
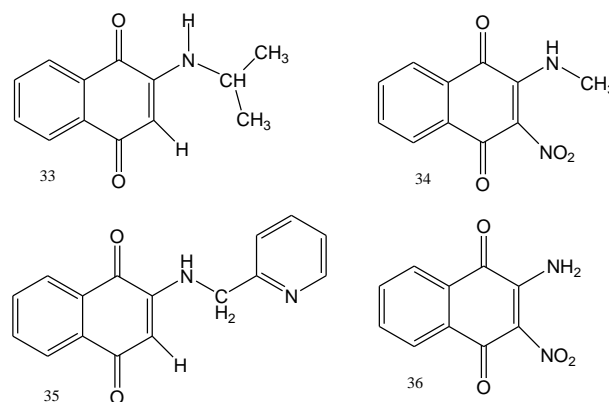
Fig. 8 – Chemical Structure of compounds 33. 34. 35 and 36.

Compound *35* showed the experimental absorption value of 2.83 eV and compared to the theoretical value of 2.81 eV the error was 0.02 eV. Finally, Compound *36* showed an experimental value of 4.95 eV and the theoretical

methodology used led to an error of 0.34 eV, which was the highest deviation between theory and experiment among all compounds used for validating the methodology.

Another interesting observation was made between Compounds *34* and *36,* which is that the addition of the methyl group in the amino group increases the proton transfer energy (ΔE_2) value about 0.60 eV, which promoted much more favorable energy gaps for the ESIPT process in *34* than *36.* This feature can be explained when the methyl group donates electronic density to the amino group, resulting in more susceptibility for proton transfer.

These values demonstrate that the PCA methodology was efficient for describing the emission energy behavior and its application for separating compound sets by similarity. Compounds *33-36*, also described the lowest errors when compared to experimental results, which demonstrate that the theoretical strategy employed for this study is good and accurate.

4. Conclusion

The reaction mechanism involving 2-amino-1.4-naphthoquinone derivatives showed that the ESIPT process is most likely to be the most effective for the proton transfer process. The methodology employed for ground and excited state calculations was adequate for this study. The kinetic parameters reveled that all compounds were kinetically favorable and Compound **1**, **2**, **6** and **8** were also thermodynamically favorable. The emission energy ΔE_3 showed hipsochromic effect for all cases ranging from red to green color (ANQ) as well as from blue and violet color (halogen, methoxide derivatives and hydrocarbon derivative). The PCA analysis generated three graphs for the behavior of the compounds. Graph A demonstrates that the absorption energy for all compounds exhibits little variation, but Graph B showed same groups in relation to ΔE_2 values. The compounds that do not exhibit the ESIPT process formed a group with

positive values. The analysis for Graph C showed that when the electron donor groups were at the Position R_3 or R_5, the ΔE_3 values exhibit hypsochromic effects and when the withdrawing groups were at Position R_3 or R_5, the ΔE_3 values exhibit bathochromic effects. The compounds used to test the methodology described lower error values and demonstrated the accuracy of our theoretical strategy, for instance Compounds *32*-*36* showed an error value ranging from 0.01 to 0.60 eV. The substituent effects provide an understanding about behavior of the ANQ derivatives as well as how solvent and substituent effects influenced the kinetic and thermodynamic parameters of the ESIPT process. These conclusions can help in the understanding of emission and absorption energies and the solvent and substituent influence on the spectroscopic parameters of fluorescent probes.

5. Acknowledgements

6. References

[1]   T. a. Prime, M. Forkink, A. Logan, P.G. Finichiu, J. McLachlan, P.B. Li Pun, et al., A ratiometric fluorescent probe for assessing mitochondrial phospholipid peroxidation within living cells, Free Radic. Biol. Med. 53 (2012) 544–553. doi:10.1016/j.freeradbiomed.2012.05.033.

[2]   A. Krishna Mitra, S. Ghosh, S. Chakraborty, S. Basu, C. Saha, Synthesis and spectroscopic exploration of carboxylic acid derivatives of 6-hydroxy-1-keto-1,2,3,4-tetrahydrocarbazole: Hydrogen bond sensitive fluorescent probes, J. Lumin. 143 (2013) 693–703. doi:10.1016/j.jlumin.2013.06.021.

[3]   N. Laurieri, M.H.J. Crawford, A. Kawamura, I.M. Westwood, J.

Robinson, A.M. Fletcher, et al., Small molecule colorimetric probes for specific detection of human arylamine N-acetyltransferase 1, a potential breast cancer biomarker, J. Am. Chem. Soc. 132 (2010) 3238–3239. doi:10.1021/ja909165u.

[4]   A.J. Russell, I.M. Westwood, M.H.J. Crawford, J. Robinson, A. Kawamura, C. Redfield, et al., Selective small molecule inhibitors of the potential breast cancer marker, human arylamine N-acetyltransferase 1, and its murine homologue, mouse arylamine N-acetyltransferase 2, Bioorganic   Med.   Chem.   17   (2009)   905–918. doi:10.1016/j.bmc.2008.11.032.

[5]   N. Laurieri, J.E. Egleton, A. Varney, C.C. Thinnes, C.E. Quevedo, P.T. Seden, et al., A Novel Color Change Mechanism for Breast Cancer Biomarker Detection: Naphthoquinones as Specific Ligands of Human Arylamine N-Acetyltransferase 1, PLoS One. 8 (2013) e70600. doi:10.1371/journal.pone.0070600.

[6]   J.E. Egleton, C.C. Thinnes, P.T. Seden, N. Laurieri, S.P. Lee, K.S. Hadavizadeh, et al., Structure-activity relationships and colorimetric properties of specific probes for the putative cancer biomarker human arylamine N-acetyltransferase 1, Bioorganic Med. Chem. 22 (2014) 3030–3054. doi:10.1016/j.bmc.2014.03.015.

[7]   A. Emadi, A. Le, C.J. Harwood, K.W. Stagliano, F. Kamangar, A.E. Ross, et al., Metabolic and electrochemical mechanisms of dimeric naphthoquinones cytotoxicity in breast cancer cells, Bioorganic Med. Chem. 19 (2011) 7057–7062. doi:10.1016/j.bmc.2011.10.005.

[8]   D.T. Mancini, K. Sen, M. Barbatti, W. Thiel, T.C. Ramalho, Excited-State Proton Transfer Can Tune the Color of Protein Fluorescent Markers, ChemPhysChem. 16 (2015) 3444–3449. doi:10.1002/cphc.201500744.

[9]   A.D. Laurent, Y. Houari, P.H.P.R. Carvalho, B. a. D. Neto, D. Jacquemin,

ESIPT or not ESIPT? Revisiting recent results on 2,1,3-benzothiadiazole under the TD-DFT light, RSC Adv. 4 (2014) 14189. doi:10.1039/c4ra00991f.

[10]   E.P. Rocha, T.C. Ramalho, Probing the ESIPT process in 2-amino-1,4-naphthoquinone: thermodynamics properties, solvent effect and chemometric analysis, Theor. Chem. Acc. 135 (2016) 39. doi:10.1007/s00214-015-1786-4.

[11]   B.K. Paul, N. Guchhait, Density functional theory (DFT) and natural bond orbital (NBO) investigation of intramolecular hydrogen bond interaction and excited-state intramolecular proton transfer (ESIPT) reaction in a five-membered hydrogen-bonding system 2-(1H-pyrazol-5-yl)pyridi, Comput. Theor. Chem. 972 (2011) 1–13. doi:10.1016/j.comptc.2011.06.004.

[12]   C. Azarias, Š. Budzák, A.D. Laurent, G. Ulrich, D. Jacquemin, Tuning ESIPT fluorophores into dual emitters, Chem. Sci. (2016). doi:10.1039/C5SC04826E.

[13]   D. Bose, B. Jana, S. Datta, N. Chattopadhyay, Journal of Photochemistry and Photobiology A : Chemistry Excited state intramolecular proton transfer of 2-hydroxy-1-naphthaldehyde semicarbazone : A combined fluorometric and quantum chemical study, "Journal Photochem. Photobiol. A Chem. 222 (2011) 220–227. doi:10.1016/j.jphotochem.2011.06.001.

[14]   S. Chaudhuri, B. Pahari, P.K. Sengupta, Ground and excited state proton transfer and antioxidant activity of 7-hydroxyflavone in model membranes: Absorption and fluorescence spectroscopic studies, Biophys. Chem. 139 (2009) 29–36. doi:10.1016/j.bpc.2008.09.018.

[15]   M. a. Gonçalves, F.C. Peixoto, E.F.F. da Cunha, T.C. Ramalho, Dynamics, NMR parameters and hyperfine coupling constants of the Fe3O4(100)–water interface: Implications for MRI probes, Chem. Phys. Lett. 609 (2014) 88–92. doi:10.1016/j.cplett.2014.06.030.

[16]   M.A. Gonçalves, E.F.F. da Cunha, F.C. Peixoto, T.C. Ramalho, Probing thermal and solvent effects on hyperfine interactions and spin relaxation rate of δ-FeOOH(100) and [MnH3buea(OH)]2−: Toward new MRI probes, Comput. Theor. Chem. 1069 (2015) 96–104. doi:10.1016/j.comptc.2015.07.006.

[17]   T.C. Silva, M. dos Santos Pires, A.A. de Castro, E.F.F. da Cunha, M.S. Caetano, T.C. Ramalho, Molecular insight into the inhibition mechanism of plant and rat 4-hydroxyphenylpyruvate dioxygenase by molecular docking and DFT calculations, Med. Chem. Res. 24 (2015) 3958–3971. doi:10.1007/s00044-015-1436-3.

[18]   R.P. Kumar, L. Roopa, U. Nongthomba, M.M. Sudheer Mohammed, N. Kulkarni, Docking, molecular dynamics and QM/MM studies to delineate the mode of binding of CucurbitacinE to F-actin, J. Mol. Graph. Model. 63 (2016) 29–37. doi:10.1016/j.jmgm.2015.11.007.

[19]   T.R. Papo, D. Jaganyi, Kinetic and mechanistic investigation into the influence of substituents on the substitution reactions of Pt(II) NCN-donor complexes, Transit. Met. Chem. 40 (2015) 53–60. doi:10.1007/s11243-014-9889-7.

[20]   D. Jacquemin, E. a Perpète, I. Ciofini, C. Adamo, Fast and reliable theoretical determination of pKa* for photoacids., J. Phys. Chem. A. 112 (2008) 794–796. doi:10.1021/jp7105814.

[21]   W.J. Knaeble, E. Iglesia, Kinetic and Theoretical Insights into the Mechanism of Alkanol Dehydration on Solid Brønsted Acid Catalysts, J. Phys. Chem. C. (2016) acs.jpcc.5b11127. doi:10.1021/acs.jpcc.5b11127.

[22]   D. Hessz, B. Hégely, M. Kállay, T. Vidóczy, M. Kubinyi, Solvation and protonation of coumarin 102 in aqueous media: A fluorescence spectroscopic and theoretical study, J. Phys. Chem. A. 118 (2014) 5238–5247. doi:10.1021/jp504496k.

[23]   B. Marciniak, H. Kozubek, S. Paszyc, Estimation of pKa* in the first excited singlet state. A physical chemistry experiment that explores acid-base properties in the excited state, J. Chem. Educ. 69 (1992) 247. doi:10.1021/ed069p247.

[24]   O.A. Borg, B. Durbeej, Relative ground and excited-state pKa values of phytochromobilin in the photoactivation of photochrome: A computational study, J. Phys. Chem. B. 111 (2007) 11554–11565. doi:10.1021/jp0727953.

[25]   F.A.D.C. Silva, E.T. Rezende, D.B. Filho, D. De Brito Rezende, I.M. Cuccovia, L.F. Gome, et al., Prototropic studies in vitreous and in solid phases: Pyranine and 2-naphthol excited state proton transfer, J. Lumin. 146 (2014) 57–63. doi:10.1016/j.jlumin.2013.09.038.

[26]   P. Idoux, K. Hancock, The Correlation of the Electronic Spectra , Ground-State p, 4858 (1967).

[27]   M. Dixit, M. Kosa, O.S. Lavi, B. Markovsky, D. Aurbach, D.T. Major, Thermodynamic and kinetic studies of LiNi $_{0.5}$ Co $_{0.2}$ Mn $_{0.3}$ O $_2$ as a positive electrode material for Li-ion batteries using first principles, Phys. Chem. Chem. Phys. 18 (2016) 6799–6812. doi:10.1039/C5CP07128C.

[28]   W. Qi, J. Ran, R. Wang, X. Du, J. Shi, M. Ran, Kinetic mechanism of effects of hydrogen addition on methane catalytic combustion over Pt(111) surface: A DFT study with cluster modeling, Comput. Mater. Sci. 111 (2016) 430–442. doi:10.1016/j.commatsci.2015.09.002.

[29]   Y. Wang, J. Ren, S. Qi, D. Wei, M. Tang, Mechanistic insights into the stereoselective C2-functionalization of 1-substituted imidazoles with cyanophenylacetylene and aldehydes, Comput. Theor. Chem. 1049 (2014) 35–41. doi:10.1016/j.comptc.2014.09.015.

[30]   Y.H. Mariam, L. Chantranupong, DFT computational studies of intramolecular hydrogen-bonding interactions in a model system for 5-

iminodaunomycin, J. Mol. Struct. THEOCHEM. 529 (2000) 83–97. doi:10.1016/S0166-1280(00)00535-2.

[31] Y.H. Mariam, R.N. Musin, A B3LYP study of intramolecular hydrogen bonding and proton transfer in naphthazarin: A model system for daunomycin/adriamycin, J. Mol. Struct. THEOCHEM. 549 (2001) 123–136. doi:10.1016/S0166-1280(01)00487-0.

[32] G. Lamoureux, A.L. Perez, M. Araya, C. Agüero, Reactivity and structure of derivatives of 2-hydroxy-1, 4-naphthoquinone (lawsone), J. Phys. Org. Chem. 21 (2008) 1022–1028. doi:10.1002/poc.1435.

[33] Š. Budzák, A. Charaf-eddin, M. Medved, D.T. Gryko, D. Jacquemin, Optical properties of V-shaped bis-coumarins : Ab initio insights, 1076 (2016) 57–64. doi:10.1016/j.comptc.2015.12.001.

[34] J. Jayabharathi, V. Thanikachalam, M. Vennila, K. Jayamoorthy, Potential fluorescent chemosensor based on L-tryptophan derivative: DFT based ESIPT process., Spectrochim. Acta. A. Mol. Biomol. Spectrosc. 95 (2012) 446–51. doi:10.1016/j.saa.2012.04.017.

[35] J. Niu, X. Du, J. Ran, R. Wang, Dry (CO2) reforming of methane over Pt catalysts studied by DFT and kinetic modeling, Appl. Surf. Sci. (2016). doi:10.1016/j.apsusc.2016.01.212.

[36] G.B. Guseva, A.A. Ksenofontov, E.V. Antina, Theoretical studies on the electronic structure and spectroscopic properties of zinc(II) bis(dipyrrinate)s, Comput. Theor. Chem. 1054 (2015) 88–92. doi:10.1016/j.comptc.2014.12.018.

[37] C. Li, C. Ma, D. Li, Y. Liu, Excited state intramolecular proton transfer (ESIPT) of 6-amino-2-(2′-hydroxyphenyl)benzoxazole in dichloromethane and methanol: A TD-DFT quantum chemical study, J. Lumin. 172 (2016) 29–33. doi:10.1016/j.jlumin.2015.11.026.

[38] P. Bermejo-Bescós, S. Martín-Aragón, K.L. Jiménez-Aliaga, A. Ortega,

M.T. Molina, E. Buxaderas, et al., In vitro antiamyloidogenic properties of 1,4-naphthoquinones, Biochem. Biophys. Res. Commun. 400 (2010) 169–174. doi:10.1016/j.bbrc.2010.08.038.

[39] S.L. De Castro, F.S. Emery, E.N. Da Silva Júnior, Synthesis of quinoidal molecules: Strategies towards bioactive compounds with an emphasis on lapachones, Eur. J. Med. Chem. 69 (2013) 678–700. doi:10.1016/j.ejmech.2013.07.057.

[40] S.M. Basheer, A.C. Willis, R.J. Pace, A. Sreekanth, Spectroscopic and TD-DFT Studies on the Turn-off Fluorescent Chemosensor based on Anthraldehyde N(4) Cyclohexyl Thiosemicarbazone for the Selective Recognition of Fluoride and Copper Ions, Polyhedron. (2016). doi:10.1016/j.poly.2016.01.021.

[41] D. Jacquemin, C. Peltier, I. Ciofini, Visible spectrum of naphthazarin investigated through time-dependent density functional theory, Chem. Phys. Lett. 493 (2010) 67–71. doi:10.1016/j.cplett.2010.04.071.

[42] X. Lan, D. Yang, X. Sui, D. Wang, Time-dependent density functional theory (TD-DFT) study on the excited-state intramolecular proton transfer (ESIPT) in 2-hydroxybenzoyl compounds: Significance of the intramolecular hydrogen bonding, Spectrochim. Acta - Part A Mol. Biomol. Spectrosc. 102 (2013) 281–285. doi:10.1016/j.saa.2012.10.017.

[43] D. Yang, R. Zheng, Y. Wang, J. Lv, Theoretical investigation on ESIPT mechanism of a new fluorescent sensor in different solvents., Spectrochim. Acta. A. Mol. Biomol. Spectrosc. 159 (2016) 30–34. doi:10.1016/j.saa.2016.01.025.

[44] S. Barman, S.K. Mukhopadhyay, S. Biswas, S. Nandi, M. Gangopadhyay, S. Dey, et al., A p -Hydroxyphenacyl-Benzothiazole-Chlorambucil Conjugate as a Real-Time-Monitoring Drug-Delivery System Assisted by Excited-State Intramolecular Proton Transfer, Angew. Chemie Int. Ed. 55

(2016) 4194–4198. doi:10.1002/anie.201508901.

[45] M.R.S. Kumar, K. Aithal, B.S.S.B.N. Rao, N. Udupa, B.S.S.B.N. Rao, Cytotoxic, genotoxic and oxidative stress induced by 1,4-naphthoquinone in B16F1 melanoma tumor cells, Toxicol. Vitr. 23 (2009) 242–250. doi:10.1016/j.tiv.2008.12.004.

[46] L.M. Gornostaev, I.S. Kryukovskaya, T.I. Lavrikova, M. V. Vigant, Y. V. Gatilov, Synthesis of 2-amino(alkylamino)-3-nitro-1,4-naphthoquinones, Russ. J. Org. Chem. 50 (2014) 205–210. doi:10.1134/S1070428014020110.

[47] E.P. da Rocha, A.A. Castro, T.C. Ramalho, E.F.F. da Cunha, Insights into the value of statistical models and relativistic effects for the investigation of halogenated derivatives of fluorescent probes, Theor. Chem. Acc. 135 (2016) 135. doi:10.1007/s00214-016-1862-4.

[48] A. Elkechai, F. Kias, F. Talbi, A. Boucekkine, Redox properties of biscyclopentadienyl uranium(V) imido-halide complexes: a relativistic DFT study., J. Mol. Model. 20 (2014) 2294. doi:10.1007/s00894-014-2294-5.

[49] D. Reinen, M. Atanasov, P. Köhler, D. Babel, Jahn–Teller coupling and the influence of strain in Tg and Eg ground and excited states – A ligand field and DFT study on halide MIIIX6 model complexes [M=TiIII–CuIII; X=F−, Cl−], Coord. Chem. Rev. 254 (2010) 2703–2754. doi:10.1016/j.ccr.2010.04.015.

[50] C. Daniel, Photochemistry and photophysics of transition metal complexes: Quantum chemistry, Coord. Chem. Rev. 282-283 (2014) 19–32. doi:10.1016/j.ccr.2014.05.023.

[51] L. Wilbraham, M. Savarese, N. Rega, C. Adamo, I. Ciofini, Describing Excited State Intramolecular Proton Transfer in Dual Emissive Systems: A Density Functional Theory Based Analysis, J. Phys. Chem. B. 119

(2015) 2459–2466. doi:10.1021/jp507425x.

[52]   F. Neese, The ORCA program system, Wiley Interdiscip. Rev. Comput. Mol. Sci. 2 (2012) 73–78. doi:10.1002/wcms.81.

[53]   G.A. Zhurko, D.A. Zhurko, Chemcraft program, Academic version, (2015).

[54]   M.M.C. Ferreira, Multivariate QSAR, J. Braz. Chem. Soc. 13 (2002) 742–753. doi:10.1590/S0103-50532002000600004.

[55]   C.A. Barboza, P.A.M. Vazquez, D. Mac-Leod Carey, R. Arratia-Perez, A TD-DFT basis set and density functional assessment for the calculation of electronic excitation energies of fluorene, Int. J. Quantum Chem. 112 (2012) 3434–3438. doi:10.1002/qua.24300.

[56]   F.L. do N. Silva, E.M. Schmidt, C.L. Messias, M.N. Eberlin, A.C. Helena Frankland Sawaya, Quantitation of organic acids in wine and grapes by direct infusion electrospray ionization mass spectrometry, Anal. Methods. 7 (2015) 53–62. doi:10.1039/C4AY00114A.

[57]   J.A. Nascimento, A.G.G. Dionísio, E.C.L. Do Nascimento, S.K.B. Freitas, M.C.U. De Araújo, Análise screening de vinhos empregando um analisador fluxo-batelada, espectroscopia UV-VIS e quimiometria, Quim. Nova. 33 (2010) 351–357. doi:10.1590/S0100-40422010000200022.

[58]   J. Li, X.J. Qi, Y.Y. Du, H.E. Fu, G.N. Chen, H.H. Yang, Efficient detection of secondary structure folded nucleic acids related to Alzheimer's disease based on junction probes, Biosens. Bioelectron. 36 (2012) 142–146. doi:10.1016/j.bios.2012.04.003.

[59]   C. Scharnagl, R. a Raupp-Kossmann, Solution pKa Values of the Green Fluorescent Protein Chromophore from Hybrid Quantum-Classical Calculations, J. Phys. Chem. B. 108 (2004) 477–489. doi:10.1021/jp036411u.

[60]   P.J. Ballester, I. Westwood, N. Laurieri, E. Sim, W.G. Richards,

Prospective virtual screening with Ultrafast Shape Recognition: the identification of novel inhibitors of arylamine N-acetyltransferases, J. R. Soc. Interface. 7 (2010) 335–342. doi:10.1098/rsif.2009.0170.

[61] B.R. Jali, K. Masud, J.B. Baruah, Selectivity in changes of fluorescence emission of 1,4-naphthoquinone derivatives by manganese and cadmium ions, Polyhedron. 51 (2013) 75–81. doi:10.1016/j.poly.2012.12.018.
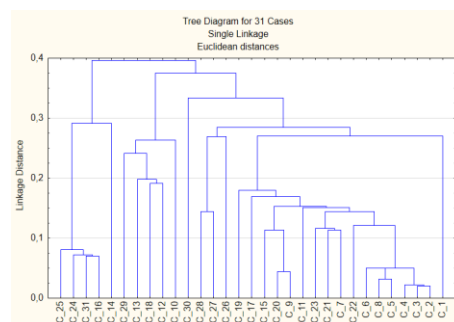
Supplementary Material

S1. HCA statistical model
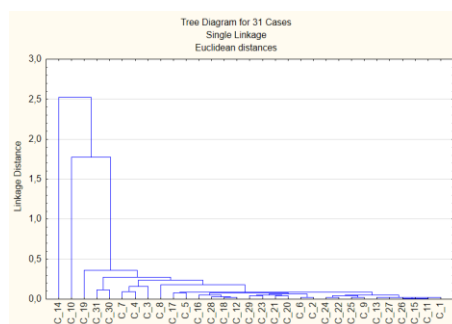
Figure S1 – HCA employed single linkage and Euclidean distances for analyses of compounds 1 at 31 according values of absorption energy.
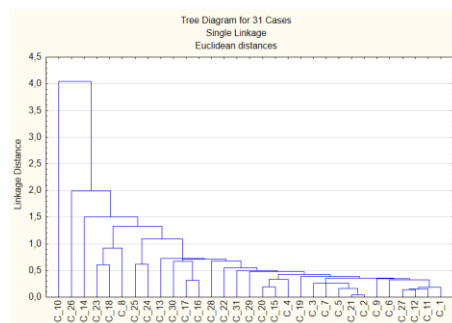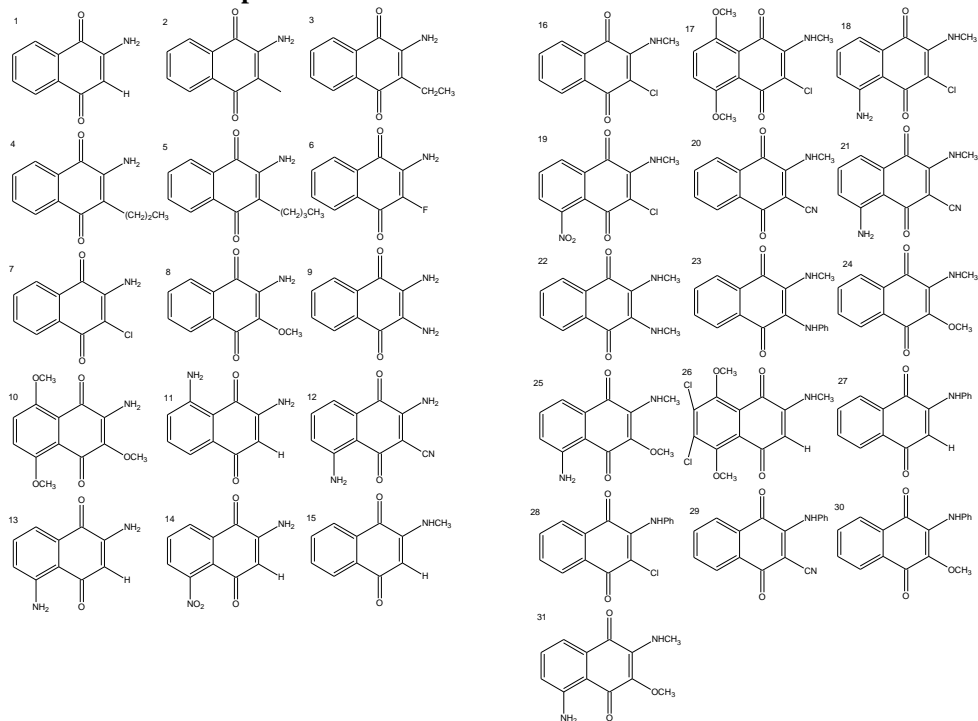

Figure S2 – HCA employed single linkage and Euclidean distances for analyses of compounds 1 at 31 according values of proton transfer energy.

Figure S3 – HCA employed single linkage and Euclidean distances for analyses of compounds 1 at 31 according values of emission energy.

S2. Structure of compounds

Figure S4 - Structure of the compounds 1 at 31 employed in substituents effect study and PCA analysis.

S3. Thermodynamic parameters

Table S1 – Thermodynamic parameters (kcal/mol) for transition state and final stage of proton transfer of naphthoquinones derivative.

	ΔE_a	ΔE_a*	$\Delta H^{\ddagger}$	$T\Delta S^{\ddagger}$	ΔE	$\Delta E*$	ΔH	$T\Delta S$
1	43.17	25.24	38.38	0.85	13.34	-56.19	12.38	-0.56
2	83.76	71.54	76.68	0.38	13.66	-96.60	12.10	0.67
3	74.47	64.93	67.07	0.08	12.65	-84.25	11.03	0.72
4	76.00	70.32	69.36	0.52	12.55	-85.37	11.50	-0.78
5	85.28	68.76	78.56	-1.29	12.56	-94.47	10.92	0.95
6	45.12	43.93	39.58	-0.27	14.54	-68.56	12.23	1.73
7	43.48	35.62	33.5	-0.20	12.68	-54.31	11.19	0.72
8	44.00	34.56	38.57	-0.76	-48.49	-117.69	-47.17	2.59

Table S2 – Energy values for ground and excited-state determined in each point from potential energy surface.

Points	GS (a.u.)	ΔGS (kcal/mol)	ES (a.u.)	ΔES (kcal/mol)	d (N – H) (Å)	d (O – H) (Å)
1	-590.52	2.413	-590.31	2.46	1.04	1.82
2	-590.52	5.615	-590.31	5.62	1.04	1.78
3	-590.51	9.739	-590.30	9.63	1.05	1.75
4	-590.50	14.592	-590.30	14.23	1.06	1.69
5	-590.50	19.769	-590.29	18.97	1.09	1.64
6	-590.49	24.841	-590.28	23.36	1.13	1.59
7	-590.48	29.458	-590.28	27.00	1.18	1.54
8	-590.47	33.370	-590.27	29.56	1.24	1.48
9	-590.47	36.433	-590.27	30.91	1.30	1.42
10	-590.46	38.613	-590.26	30.98	1.35	1.37
11	-590.46	39.979	-590.26	29.68	1.41	1.32
12	-590.46	40.697	-590.27	26.96	1.47	1.27
13	-590.46	40.978	-590.27	24.36	1.53	1.22
14	-590.45	40.994	-590.27	20.14	1.58	1.17
15	-590.45	40.823	-590.28	17.96	1.64	1.13
16	-590.46	40.604	-590.28	16.38	1.69	1.10
17	-590.46	40.350	-590.29	15.00	1.73	1.08
18	-590.46	40.053	-590.29	13.90	1.78	1.06
19	-590.46	39.785	-590.29	12.45	1.82	1.05
20	-590.46	39.459	-590.29	11.65	1.86	1.04
21	-590.46	39.292	-590.29	10.99	1.90	1.03
22	-590.46	38.849	-590.30	10.24	1.93	1.03
23	-590.46	39.004	-590.30	9.82	1.96	1.02
24	-590.46	38.466	-590.30	9.21	1.99	1.02
25	-590.46	38.421	-590.30	8.56	2.03	1.01
26	-590.46	38.294	-590.30	8.37	2.05	1.02
27	-590.46	38.086	-590.30	7.75	2.11	1.01
28	-590.46	38.071	-590.30	7.59	2.14	1.00
29	-590.46	37.928	-590.30	7.18	2.22	1.00
30	-590.46	37.980	-590.30	6.88	2.24	1.00

*Δ is a difference between the next point and the initial point ($\Delta = p_n - p_1$);
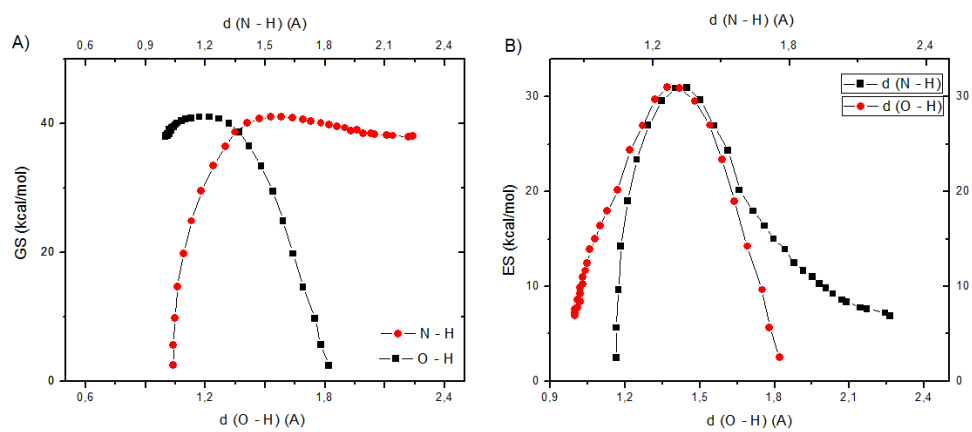
Figure S5 – Relation between energy in ground and excited-state at distances N – H and O – H in PES.

CONCLUSÃO GERAL

O estudo de sondas fluorescentes requer investigações teóricas e experimentais para o entendimento dos mecanismos envolvidos e de sua aplicabilidade. De fato, investigações cada vez mais abrangentes para aplicação de sondas espectroscópicas em organismos vivos ainda são necessárias. A utilização de sondas fluorescentes em diferentes ambientes surge como uma promissora área para a detecção de compostos de interesse ambiental, medicinal e bioquímico. No presente trabalho, calculamos os parâmetros termodinâmicos do processo ESIPT sob a ótica da DFT, avaliando o melhor funcional para os estudos geométricos no estado fundamental, o qual foi o B3LYP, e o melhor funcional para os estudos do estado excitado foi o funcional CAM-B3LYP. A escolha dos funcionais foi auxiliada por técnicas quimiométricas, como a PCA e HCA. O processo ESIPT se apresenta como o mecanismo possível para os derivados da 2-amino-1.4-naphthoquinona e o clorofórmio foi o solvente mais favorável termodinamicamente para o processo ESIPT. Dentre nossos resultados, a ANQ se mostrou versátil nos diferentes solventes e potencial aplicação como sonda fluorescente. O modelo fatorial foi satisfatório para avaliar os efeitos relativísticos e os parâmetros espectroscópicos para derivados halogenados da ANQ. A metodologia descreveu o Hamiltoniano DKH2 como o melhor entre os abordados. Mostrou, também, que a interação entre o Hamiltoniano e a função de base é significativa para este estudo. Finalmente, o presente trabalho demonstrou que os substituintes halogenados Cl, Br e I desativaram o processo ESIPT, sendo que apenas os compostos contendo flúor, que devido a alta eletronegatividade promove o aumento da acidez do grupo amino facilitando o processo, ou sem halogênios demonstraram emissão de fluorescência via ESIPT, emitindo na região do vermelho e do azul, respectivamente. Acreditamos que o estudo dos efeitos relativísticos no processo ESIPT de ANQ e derivados pode auxiliar no entendimento desse processo, bem como auxiliar em estratégias teóricas para o

estudo apropriado desse fenômeno. De acordo com os nossos resultados, todos os compostos testados foram cineticamente favoráveis ao processo ESIPT. O efeito dos substituintes demonstrou que grupos retiradores de elétrons proporcionam o deslocamento da emissão para a região do azul, enquanto grupos doadores de elétrons deslocam a emissão para a região do vermelho. O estudo com derivados de naftoquinonas empregados como sondas teve desvio médio calculado para o valor de emissão de 0,01 eV, demonstrando que a metodologia empregada está coerente com os valores experimentais. O entendimento do mecanismo de emissão de fluorescência bem como a natureza cinética e termodinâmica do processo investigado pode auxiliar no desenvolvimento de novos sensores mais eficientes e precisos bem como inferir na cor das emissões apresentadas por esses compostos em solução e vácuo.

ANEXO I

- TRABALHOS DESENVOLVIDOS -

Insights into the value of statistical models and relativistic effects for the investigation of halogenated derivatives of fluorescent probes

Eduardo P. da Rocha[1,3] · Alexandre A. Castro[1] · Teodorico C. Ramalho[1,2] ·
Elaine F. F. da Cunha[1]

CrossMark

REGULAR ARTICLE

Probing the ESIPT process in 2-amino-1,4-naphthoquinone: thermodynamics properties, solvent effect and chemometric analysis

Eduardo Pereira Rocha[1,3] · Teodorico Castro Ramalho[1,2]

1

Molecular Docking, Metal Substitution and Hydrolysis Reaction of Chiral Substrates of Phosphotriesterase

Alexandre A. de Castro[1], Melissa S. Caetano[2] and Telles C. Silva[1], Daiana T. Mancini[1], Eduardo Pereira Rocha[1], Elaine F.F. da Cunha[1] and Teodorico C. Ramalho[*,1,3]

[1]*Department of Chemistry. Federal University of Lavras, University Campus, 37200-000, Lavras-MG, Brazil*

[2]*Institute of Exact and Biological Sciences. Federal University of Ouro Preto, University Campus, 35400000, Ouro Preto, Brazil*

[3]*Center for Basic and Applied Research, Faculty of Informatics and Management, University of Hradec Kralove, Czech Republic*
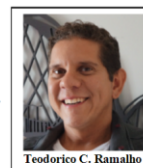
Teodorico C. Ramalho

Abstract: During World War II, organophosphorus compounds with neurotoxic action were developed and used as the basis for the development of structures currently used as pesticides in the agricultural industry. Among the nerve agents, Tabun, Sarin, Soman and VX are the most important. The factor responsible for the high toxicity of organophosphorus (OP) is the acetylcholinesterase inhibition. However, one of the characterized enzymes capable of degrading OP is Phosphotriesterase (PTE). This enzyme has generated considerable

Artigo Geral 16

Planejamento Fatorial para a Investigação das Propriedades Espectroscópicas, Efeitos Relativísticos e de Solvatação de Derivados Halogenados da 2-Amino-1,4-Naftoquinona

Eduardo P. Rocha, Lívia C. T. Lacerda, Mateus A. Gonçalves, Maíra S. Pires,
Telles C. Silva, Henrique A. Rodrigues & Teodorico C. Ramalho